

# Signal Processing Methods for Neutron Detection with a Diamond Detector at Cryogenic Temperatures

---

Cosic, Donny Domagoj

Doctoral thesis / Disertacija

2024

*Degree Grantor / Ustanova koja je dodijelila akademski / stručni stupanj:* **University of Split, Faculty of Electrical Engineering, Mechanical Engineering and Naval Architecture / Sveučilište u Splitu, Fakultet elektrotehnike, strojarstva i brodogradnje**

*Permanent link / Trajna poveznica:* <https://um.nsk.hr/um:nbn:hr:179:509286>

*Rights / Prava:* [In copyright](#) / [Zaštićeno autorskim pravom.](#)

*Download date / Datum preuzimanja:* **2024-11-24**



*Repository / Repozitorij:*

[Repository of the Faculty of Electrical Engineering, Mechanical Engineering and Naval Architecture - University of Split](#)



UNIVERSITY OF SPLIT  
FACULTY OF ELECTRICAL ENGINEERING, MECHANICAL ENGINEERING AND  
NAVEL ARCHITECTURE

**Donny Domagoj Cosic**

**SIGNAL PROCESSING METHODS FOR NEUTRON  
DETECTION WITH A DIAMOND DETECTOR AT  
CRYOGENIC TEMPERATURES**

DOCTORAL THESIS

Split, 2024



UNIVERSITY OF SPLIT  
FACULTY OF ELECTRICAL ENGINEERING, MECHANICAL ENGINEERING AND  
NAVEL ARCHITECTURE

**Donny Domagoj Cosic**

***Signal Processing Methods for Neutron Detection with a  
Diamond Detector at Cryogenic Temperatures***

DOCTORAL THESIS

Split, 2024

The research reported in this thesis was carried out at the department of Electronics and Computing, University of Split, Faculty of Electrical Engineering, Mechanical Engineering and Naval Architecture.

Supervisors: Prof. dr. sc. Dinko Begušić, FESB, University of Split, Croatia

Dr. sc. Tonči Tadić, Ruđer Bošković Institute, Zagreb

Dissertation number: 206

---

## BIBLIOGRAPHIC INFORMATION

Keywords: scCVD diamond, cryogenic temperatures, ionizing radiation, IBIC, TCT, signal processing, neutron detection, pulse shape discrimination

Scientific area: Technical Sciences

Scientific field: Electrical Engineering

Scientific branch: Electronics

Institution of PhD completion: University of Split, Faculty of Electrical Engineering, Mechanical Engineering and Naval Architecture

Supervisor of the thesis: Prof. dr. sc. Dinko Begušić, Dr. sc. Tonči Tadić

Number of pages: 156

Number of figures: 74

Number of tables: 13

Number of references: 108

---

Committee for assessment of doctoral dissertation:

1. Professor dr. sc. Joško Radić University of Split, Faculty of Electrical Engineering, Mechanical Engineering and Naval Architecture, Split
2. Professor dr. sc. Mladen Russo University of Split, Faculty of Electrical Engineering, Mechanical Engineering and Naval Architecture, Split
3. Associate professor dr. sc. Matko Šarić University of Split, Faculty of Electrical Engineering, Mechanical Engineering and Naval Architecture, Split
4. Associate professor dr. sc. Maja Stella University of Split, Faculty of Electrical Engineering, Mechanical Engineering and Naval Architecture, Split
5. Dr. sc. Milko Jakšić, senior scientist, Ruđer Bošković Institute, Zagreb

Committee for defense of doctoral dissertation:

1. Professor dr. sc. Joško Radić University of Split, Faculty of Electrical Engineering, Mechanical Engineering and Naval Architecture, Split
2. Professor dr. sc. Mladen Russo University of Split, Faculty of Electrical Engineering, Mechanical Engineering and Naval Architecture, Split
3. Associate professor dr. sc. Matko Šarić University of Split, Faculty of Electrical Engineering, Mechanical Engineering and Naval Architecture, Split
4. Associate professor dr. sc. Maja Stella University of Split, Faculty of Electrical Engineering, Mechanical Engineering and Naval Architecture, Split
5. Dr. sc. Milko Jakšić, senior scientist, Ruđer Bošković Institute, Zagreb

Dissertation defended on: 24<sup>th</sup> October 2024

# Signal processing methods for neutron detection with a diamond detector at cryogenic temperatures

## Abstract

Next generation of accelerator and fusion research facilities, such as DONES, will require detectors that can operate reliably under extreme conditions, in particular, at cryogenic temperatures and at very high radiation fluences. Diamond based detectors have the potential to satisfy these requirements plus have the added benefit of being intrinsically sensitive to neutron radiation. This work presents a methodology for testing the performance of diamond detectors in such an environment. All components of the signal processing chain were analytically and experimentally examined to produce an optimized apparatus which then was used to systematically evaluate the charge collection efficiency from room temperature down to 46 K. A drastic drop in the charge collection efficiency has been observed at low temperature for H, He, Li, C ions, and neutrons, while less severe for  $\gamma$ -rays. The mechanism behind this observation were investigated and attributed to the density of the generated charge carriers and the generation/evaporation of excitons. Furthermore, a database of current profiles resulting from the interaction of various types of radiation with the diamond detector was built up and benchmarked. From this information pulse shape discrimination algorithms were developed and evaluated. This work contributes to the development of micro loss monitors based on diamond detectors.

**Keywords:** scCVD diamond, cryogenic temperatures, ionizing radiation, IBIC, TCT, neutron detection, pulse shape discrimination

# Metode obrade signala za detekciju neutrona pomoću dijamantnog detektora na kriogenim temperaturama

## Sažetak

Sljedeća generacija akceleratora i istraživačkih postrojenja za fuziju, poput DONES-a, zahtijevat će detektore koji mogu pouzdano raditi u ekstremnim uvjetima, posebno pri kriogenim temperaturama i vrlo visokim intenzitetima zračenja. Detektori na bazi dijamanta imaju potencijal zadovoljiti te zahtjeve i imaju dodatnu prednost što su intrinzično osjetljivi na neutronske zračenje. Ovaj rad predstavlja metodologiju testiranja performanse dijamantnih detektora u takvom okruženju. Svi dijelovi lanca obrade signala analitički i eksperimentalno su ispitani kako bi se proizvela optimizirana aparatura koja je zatim korištena za sistematsku evaluaciju učinkovitosti prikupljanja naboja od sobne temperature do 47 K. Drastičan pad u učinkovitosti prikupljanja naboja uočen je pri niskim temperaturama za H, He, Li, C ione i neutrone, dok je manje izražen za  $\gamma$ -zrake. Mehanizmi iza ove pojave su istražena i povezana s gustoćom generiranih nositelja naboja i generacijom/isparavanjem ekcitona. Nadalje, prikupljena je baza podataka o profilima struje nastale uslijed interakcije različitih vrsta zračenja s dijamantnim detektorom na bazi dijamanta te je napravljena usporedba s osnovnim pokazateljem. Na temelju te informacije, razvijeni su i evaluirani algoritmi za diskriminaciju na bazi oblika impulsa. Ovaj rad doprinosi razvoju monitora mikro-gubitaka temeljenih na dijamantnim detektorima.

**Ključne riječi:** scCVD dijamant, kriogenske temperature, ionizirajuće zračenje, IBIC, TCT, detekcija neutrona, diskriminacija oblika pulsa





## **Acknowledgments**

I would like to express my sincere gratitude to my family, mentors and the entire staff of the Laboratory for Ion Beam Interactions at the Ruđer Bošković Institute. Their unwavering patience, enthusiasm, and constant encouragement have been invaluable throughout this work. I am also grateful to the teams at the Ruđer Bošković Neutron Facility and the NCSR “Demokritos” Tandem Accelerator for generously providing the necessary beam time for this work. In particular, I would like to extend my heartfelt thanks to Dr. Georgios Provas and Dr. Milko Jakšić for their dedicated time and effort; their support was instrumental in making this research possible.

# Contents

Abstract.....	iv
Sažetak.....	v
Acknowledgments .....	vii
List of Tables .....	x
List of Figures.....	xi
List of Acronyms .....	xvi
<b>1 INTRODUCTION .....</b>	<b>1</b>
<b>2 INTERACTION OF RADIATION WITH MATTER.....</b>	<b>5</b>
2.1 Charged Particles.....	5
2.2 Photons .....	7
2.3 Neutrons .....	7
2.3.1 Fast Neutrons.....	8
2.3.2 Slow Neutrons.....	10
2.4 Neutron generation.....	11
2.5 Distinguishing radiation by interaction volume .....	12
<b>3 RADIATION DETECTION WITH DIAMONDS .....</b>	<b>15</b>
3.1 Signal generation.....	17
3.2 Effects of defects in diamond on charge transport .....	22
3.3 Polarization phenomenon in scCVD diamond.....	24
3.4 Low temperature dependences .....	26
3.5 CCE measuring techniques at low temperatures.....	28
<b>4 DETECTOR SIGNAL PROCESSING.....</b>	<b>29</b>
4.1 Preamplifiers for radiation detectors .....	30
4.2 Characteristics of noise .....	33
4.3 Digital signal processing of preamplifier signals .....	36
4.4 Ion beam analysis .....	46
<b>5 NEUTRON DISCRIMINATION.....</b>	<b>49</b>
5.1 Neutron induced spectra in diamond detectors .....	49

5.2	Discrimination through detector configurations .....	52
5.3	Discrimination based on Pulse Shape Analysis.....	53
5.4	Discrimination based on event coincidences .....	57
5.5	Summary of discrimination techniques.....	58
<b>6</b>	<b>EXPERIMENTAL SETUP.....</b>	<b>61</b>
6.1	$\mu$ -Loss Monitors for DONES .....	63
6.2	Diamond detector .....	67
6.3	Cryogenic system .....	70
6.4	Data acquisition and experiment control.....	72
6.5	Experiment simulations.....	77
6.6	Measurements.....	81
6.6.1	Ions .....	82
6.6.2	$\gamma$ -rays .....	83
6.6.3	Neutrons .....	85
<b>7</b>	<b>DETECTOR PERFORMANCE EVALUATION .....</b>	<b>87</b>
7.1	Charge Collection Efficiency .....	87
7.2	Detector Performance.....	93
7.3	Transient Current Technique .....	99
7.4	Signal Benchmarking .....	106
7.5	PSD of Neutron/ $\gamma$ -ray Signals.....	109
<b>8</b>	<b>CONCLUSION .....</b>	<b>123</b>
	<b>BIBLIOGRAPHY .....</b>	<b>127</b>

## List of Tables

2.1	<i>Neutron induced reaction in carbon.</i> .....	9
2.2	<i>Converter layer reactions for the detection of slow neutrons with a diamond detector.</i> .....	10
2.3	<i>Neutron source reactions</i> .....	11
3.1	<i>Comparison of diamond detector properties with other detector materials.</i> .....	15
3.2	<i>Transit time for charge carriers [29].</i> .....	20
3.3	<i>Exciton lifetime dependence on temperature [31][44].</i> .....	23
4.1	<i>Parallel noise sources.</i> .....	34
4.2	<i>Comparison of filter performance to the optimum filter.</i> .....	40
5.1	<i>Summary of neutron/<math>\gamma</math>-ray discrimination methods from literature.</i> .....	58
6.1	<i>Calculated ion energies for same depth in a diamond crystal. *<math>E_{eh} = 13.6</math> eV [100].</i> .....	77
7.1	<i>Summary of CCE drop per impeding particle. For neutrons, the CCE value at 80 K is given since the evaluation of the CCE was not possible below this temperature.</i> .....	94
7.2	<i>Noise RMS values for different filter parameters. The parameters corresponding to the highlighted values were further evaluated on various signal shapes.</i> .....	102
7.3	<i>FOM results for the evaluation of the presented two PSD methods at different temperatures.</i> .....	120

## List of Figures

2.1	<i>Ionization profile of 5.5 MeV alpha particles in diamond.</i>	6
2.2	<i>Neutron cross section for <math>^{12}\text{C}</math> [19].</i>	9
2.3	<i>Neutron cross section data for <math>^6\text{Li}</math> and <math>^{10}\text{B}</math> [19].</i>	10
2.4	<i>Various mechanisms of radiation detector based on interaction volume.</i>	13
3.1	<i>Induced current from a) alpha particle and b) minimum ionizing particles (MIP) [29], [31].</i>	19
3.2	<i>e-h pair screening effect [46].</i>	24
3.3	<i>Polarization [47].</i>	25
3.4	<i>Measured charge as a function of temperature [31].</i>	27
4.1	<i>General signal processing chain used to acquire signals from an ionizing radiation detector.</i>	29
4.2	<i>Typical pulse expected at the output of the detector, integrating preamplifier and after analog filtering stage. The height of the shaped pulse is proportional to the deposited energy of the impinging radiation. [58].</i>	30
4.3	<i>Charge Sensitive and Current Sensitive Preamplifier schematic [59].</i>	30
4.4	<i>Detector Coupling [59].</i>	32
4.5	<i>Noise equivalent circuit of an AC coupled charge sensitive preamplifier [59].</i>	33
4.6	<i>Noise sources between the detector and the preamplifier [59].</i>	38
4.7	<i>The top graph shows the input signal (exponentially decaying signal from a preamplifier), the middle graph shows the impulse response of the filter, while the bottom graph shows the output of an optimum filter. [59].</i>	39
4.8	<i>CR-RC Filter.</i>	40
4.9	<i>Synthesizing a trapezoidal function.</i>	42
4.10	<i>Implementation of a trapezoidal filter in a DSP system [63].</i>	43
4.11	<i>FPGA implementation of trapezoidal filter.</i>	43
4.12	<i>Top level of multiparameter FPGA acquisition system implementation with the pulse processor subsystem expanded in the inlay. The pulse processor consists of a 1. Delay block, 2. Trapezoidal filter, 3. Fast filter, 4. Noise estimator, 5. Baseline restorer, and 6. Pileup rejector.</i>	44

4.13	<i>Simulation of a preamplifier pulse processed by the acquisition system algorithm. The delayed preamplifier pulse (blue) is shaped into a trapezoidal unipolar (red) and bipolar (purple) pulse. The output of the fast filter is displayed in yellow.</i>	44
4.14	<i>Pileup occurs when two pulses are close in time and are recognized as a single event by the acquisition system. a) Two pulses are accurately recognized b) Overlapped pulses recognized as a single pulse c) Complete overlap of the pulses recognized as one [58].</i>	46
4.15	<i>Ion Beam Analysis (IBA) techniques.</i>	46
4.16	<i>Imaging of a diamond detector using the IBIC method. The image on the left illustrates the measured energy by the detector across its surface. The plots (a,b) show the acquired IBIC spectrum from ROI a) and b). The region a) has lower charge collection efficiency than region b) due to polarization as discussed in section 3.2.</i>	48
5.1	<i>Spectra for Neutrons of 7 to 20 MeV [70].</i>	50
5.2	<i>Spectrum of fast neutrons below 6.2 MeV [26].</i>	50
5.3	<i>Spectra for neutrons with <sup>6</sup>LiF converter layer of various thicknesses.</i>	51
5.4	<i>Single and Sandwich Detector Configurations.</i>	52
5.5	<i>Pulses generated by a) <math>\gamma</math>-ray and b) Alpha Particles [75].</i>	53
5.6	<i>Pulse shape discrimination parameters.</i>	54
5.7	<i>Alpha particle current profile vs generation depth in a diamond detector [75].</i>	55
5.8	<i>Output signals of neutron and gamma radiation from a scintillator detector coupled to a charge sensitive preamplifier [77].</i>	56
5.9	<i>Coincidence discrimination based on nuclear reaction products.</i>	57
6.1	<i><math>\mu</math>-loss monitor location.</i>	64
6.2	<i>Radiation at <math>\mu</math>-loss monitor location. a) combined plot, logarithmic energy scale. b) separate plots, linear energy scale for <math>\gamma</math> radiation.</i>	65
6.3	<i>Neutron energy loss spectra and simulations [3].</i>	66
6.4	<i>Front End Electronics Setup.</i>	67
6.5	<i>Detector assembly. a) Electrode configuration on the diamond crystal b) Diamond mounted on PCB.</i>	68
6.6	<i>I-V Measurement of diamond detector.</i>	69
6.7	<i>Detector PCB with connector and pad for diamond crystal.</i>	69
6.8	<i>Exploded view of experimental setup.</i>	70

6.9	<i>Cross-section view of experimental setup.</i>	71
6.10	<i>Instrument Control Schematic.</i>	72
6.11	<i>Signal processing chain. a) Charge sensitive preamplifier for energy spectra acquisition. b) Current sensitive preamplifier for TCT signal acquisition.</i>	73
6.12	<i>SRIM simulation for ions. a) 0.8 MeV H<sup>+</sup> b) 3 MeV He<sup>2+</sup> c) 5.6 MeV Li<sup>2+</sup> d) 12.8 MeV C<sup>4+</sup>.</i>	78
6.13	<i>Geant4 simulation of gamma ray energy deposition in a diamond crystal. a) 200 keV b) 440 keV c) 800 keV d) 2000 keV.</i>	79
6.14	<i>Simulated spectra of the <sup>23</sup>Na(p,p'γ) reaction which produces two γ rays of higher intensities at energies 440 keV and 1634 keV.</i>	80
6.15	<i>GEANT4 simulation of 14.1 MeV neutrons on a diamond crystal.</i>	81
6.16	<i>Experimental setup installed downstream from the nuclear microprobe.</i>	82
6.17	<i>Experimental setup installed at a beam line for high current 2 MeV H for <sup>23</sup>Na(p,p'γ) γ production.</i>	84
6.18	<i>Experimental setup installed the neutron generator downstream from a tritium target.</i>	85
7.1	<i>Pulse height histograms obtained with a 12.8 MeV C<sup>4+</sup> ion beam at 50 K, 60 K, 90 K, 110 K, 130 K, and 150 K [94].</i>	88
7.2	<i>Histogram peak centroid position plotted with temperature for a) 0.8 MeV H<sup>+</sup>, b) 3 MeV He<sup>2+</sup>, c) 5.6 MeV Li<sup>2+</sup> and d) 12.8 MeV C<sup>4+</sup> ion beams [94].</i>	89
7.3	<i>Fitting the Compton edge in the experimental data obtained during the experiments with γ-rays. Plots a) and b) illustrate the simulated spectra for 440 keV and 1634 keV γ-rays overlaid with the fit functions used in the inlayed subplot, respectively. Plot c) illustrates the experimental spectrum with the cumulative fit function used in the inlayed subplot. ....</i>	91
7.4	<i>Acquired spectra (blue) overlapped with simulated (grey) spectra. For a) 14.1 MeV neutrons and b) <sup>23</sup>Na(p,p'γ) γ-rays [95].</i>	91
7.5	<i>Acquired pulse height spectra at each temperature setpoint for a) neutrons and b) <sup>23</sup>Na(p,p'γ) γ-rays [95].</i>	92
7.6	<i>Fitted centroid position for a) <sup>12</sup>C(n,α)<sup>9</sup>Be reaction and b) 440 keV γ-ray Compton edge [95].</i>	93
7.7	<i>CCE vs Temperature for a) ions b) γ-rays and neutrons. The data for 3 MeV He ion is added to both plots for comparison purposes.</i>	94



7.8	<i>Ionization profile of impinging <math>\alpha</math> particles at a) 3 MeV b) 5.5 MeV and c) 8.3 MeV.</i>	96
7.9	<i>Energy spectra collected from a triple alpha source from RT down to 46 K [95].</i>	97
7.10	<i>Influence of the detector bias voltage change from 1 V/<math>\mu</math>m to 1.33 V/<math>\mu</math>m on the CCE for ions a) H, b) He, c) Li and d) C.</i>	99
7.11	<i>Acquired TCT signal in a) time domain and b) frequency domain before signal processing. The TCT signal is highlighted along with the frequency of the superimposed noise at 107 MHz.</i>	100
7.12	<i>Impact on the signal for various notch filter parameters. a) Original signal with the frequency spectrum marked with a vertical red line at the maximum value of 107 MHz. b) 2<sup>nd</sup> order notch filter centered at 112 MHz with a width of 12 MHz c) 20<sup>th</sup> order notch filter centered at 107 MHz with a width of 2 MHz. d) Magnitude response of each filter, lower order in blue (filter #1) and the higher order in red (filter #2).</i>	101
7.13	<i>Implemented digital filter magnitude response for a) Notch Filter and b) Lowpass Filter.</i>	103
7.14	<i>Signal after a) Notch filter and b) Lowpass filter presented in both the time (top) and frequency (bottom) domain.</i>	103
7.15	<i>TCT signals acquired from a) 12.8 MeV C beam and b) 440 keV <math>\gamma</math>-rays.</i>	104
7.16	<i>TCT signals acquired by neutrons at a) 120 K and b) 55 K.</i>	105
7.17	<i>TCT pulse shapes correlated with their position in the energy spectrum [95].</i>	107
7.18	<i>a) FWHM based PSD and b) TCT traces (right) with their 1<sup>st</sup> derivative (left).</i>	110
7.19	<i>Frequency domain analysis. The top plot contains the FFT of the two neutron shapes (blue, red) and the <math>\gamma</math>-ray shape (black). Bottom plot contains the associated spectrograms of the same three shapes: a) multi-step neutron, b) square neutron, c) <math>\gamma</math>-ray.</i>	111
7.20	<i>2D histogram of cosine similarities of the datasets to an ideal line (x-axis) and ideal square (y-axis).</i>	115
7.21	<i>2D Histogram of results obtained with Method #2 at 120 K.</i>	116
7.22	<i>PSD Method #1 results presented as 2D histogram (left) and linear projection (right) at temperatures a) 120 K b) 110 K c) 100 K d) 90 K e) 80 K f) 70 K g) 60 K h) 55 K and i) 46 K.</i>	118

7.23 PSD Method #2 results presented as 2D histogram (left) and linear projection (right) at temperatures a) 120 K b) 110 K c) 100 K d) 90 K e) 80 K f) 70 K g) 60 K h) 55 K and i) 46 K..... 119

## List of Acronyms

$\mu$ BLM	Micro Beam Loss Monitors
$\mu$ LoM	Micro-Loss ( $\mu$ -Loss) Monitors
ADC	Analog to Digital Converter
CCD	Charge Collection Distance
CCE	Charge Collection Efficiency
CERN	European Council for Nuclear Research
CVD	Chemical Vapor Deposition
DAQ	Data Acquisition
DEMO	Demonstration Power Plant
DLC	Diamond-like Carbon
DONES	DEMO Oriented Neutron Source
DSP	Digital Signal Processing
EMI	Electromagnetic Interference
ENC	Equivalent Noise Charge
ENIG	Electroless Nickel Immersion Gold
EPICS	Experimental Physics and Industrial Control System
ESA	European Space Agency
EXFOR	Experimental Nuclear Reaction Data
FEE	Front-End Electronics
FET	Field Effect Transistor
FIR	Finite Impulse Response
FPGA	Field Programmable Gate Array
FWHM	Full Width at Half Maximum
HMI	Human Machine Interface
HTHP	High Temperature High Pressure
HWR	Half Wave Resonator
IAEA	International Atomic Energy Agency
IBA	Ion beam Analysis

IBIC	Ion Beam Induced Charge
IFMIF	International Fusion Material Irradiation Facility
IIR	Infinite Impulse Response
ITER	International Thermonuclear Experimental Reactor
LHC	Large Hadron Collider
LIPAc	Linear IFMIF Prototype Accelerator
GRAS	Geant4 Radiation Analysis for Space
MIP	Minimum Ionizing Particles
NNDC	National Nuclear Data Center
PCB	Printed Circuit Board
pCVD	Polycrystalline CVD
PHA	Pulse Height Analysis
PID	Proportional Integral Derivative
PSD	Pulse Shape Discrimination
RMS	Root Mean Square
scCVD	Single Crystal CVD
SNR	Signal to Noise Ratio
SRIM	Stopping and Range of Ions in Matter simulation
TCT	Transit Current Technique



## 1 INTRODUCTION

In the past decade there have been many significant advances in fusion research, most notably with the construction commencement of the International Thermonuclear Experimental Reactor (ITER). Outlined in [1], ITER is a key facility in the European roadmap towards fusion electricity and a stepping stone towards the Demonstration power plant (DEMO). However, the step between ITER and DEMO is quite large with many issues still unresolved. One of these issues is the effects of neutrons generated by fusion on materials in the immediate surrounding of the reactor core. To study this issue in more detail, a dedicated International Fusion Material Irradiation Facility – DEMO Oriented Neutron Source (IFMIF – DONES) is being planned to produce a similar neutron environment as expected in DEMO to enable research of materials suitable for extreme environments in it. The DONES design is based on a superconductive accelerator which will accelerate deuterium ions to 40 MeV of energy with a beam current of 125 mA onto a liquid lithium target to produce a neutron fluence of  $10^{18}$  n/m<sup>2</sup>/s [2]. Due to the high beam power (5 MW), the importance and requirements of the beam diagnostic systems become crucial for the operation of the accelerator and personnel safety.

Micro-loss ( $\mu$ -loss) monitors ( $\mu$ LoM) or micro beam loss monitors ( $\mu$ BLM) are part of this diagnostic system and are required to trigger the Machine Protection System in case of beam loss.  $\mu$ BLM should be able to monitor beam losses down to the levels of 1 W/m (or  $10^{-6}$  of the total beam power) and should be also used for the fine tuning of the accelerator beam optics parameters during normal operation [3], [4]. To satisfy these requirements, the detector must be mounted as close as possible to the beam, placing additional requirements on the detector [5]:

- High radiation tolerance
- Stability at cryogenic temperatures (4.5 K)
- Fast response time
- High sensitivity to neutrons and lower sensitivity to  $\gamma$ -rays

Radiation detectors based on single crystal diamonds fulfill all these requirements due to their size, physical and electrical properties, much better than conventionally used scintillators that would be unsuitable for such harsh operating conditions. Gamma radiation is detected through three interaction mechanisms: Photoelectric absorption, Compton scattering and Pair production. Out of these three interaction methods, photoelectric absorption and Compton scattering are the most probable for lower energy  $\gamma$ -rays. The probability of the photoelectric effect scales with  $Z^{3-4}$

and linearly with  $Z$  for Compton scattering and its sensitivity is proportional to the  $Z$  number of the element. Therefore, diamond (carbon) is the least sensitive solid-state detector to  $\gamma$  radiation. Low  $Z$  materials have also the additional benefit to be more radiation resistant to high energy particles because nuclear fragments are light and cause a small amount of non-ionizing energy loss inside the material [6], [7]. Further radiation hardness comes from the high displacement energy required to move a carbon atom out of its lattice position, decreasing the number of vacancies created and therefore creating less traps for charge carriers. Due to these properties, the European Organization for Nuclear Research (CERN) created a dedicated research group (RD42) to investigate diamond-based detectors for future large hadron colliders [8]–[11]. To achieve fast response times in the detector and thus enable high counting rate, it is also desirable to have the charge carrier velocity as large as possible, for which diamond is also among the most suitable materials. This is further enhanced by the possibility to increase the electric field across the diamond device until the charge carrier velocities reach saturation. The large dielectric strength of diamond allows for very large bias voltages to be applied without causing breakdown. At these high bias levels, the leakage current through the device is still in the order of pico- to nanoamps due to the low intrinsic resistance of diamond. This low leakage current results in very low noise from the detector [12]. Taking advantage of this low detector noise requires an optimized signal processing chain with particular emphasis on the front-end electronics and digital signal processing techniques.

In spite of the above noted superior characteristics of diamond radiation detectors, there is still very limited knowledge about its operation at low temperatures, in particular for the detection of neutrons. Therefore, this work was performed to test the hypothesis that a diamond-based detector can be successfully used as a neutron detector at cryogenic temperatures as well. To prove this hypothesis, the performance of a diamond-based detector collecting signals from neutrons at cryogenic temperatures had to be evaluated. Following this, a method had to be developed that could discriminate the neutron signal from other types of radiation, since  $\mu\text{LoM}$  are envisioned to operate in a mixed radiation environment. However, to develop a successful discrimination method, the performance of the diamond detector to other expected types of radiation had to also be evaluated.

In this work, two ion beam analysis techniques, namely IBIC (Ion Beam Induced Charge) and TCT (Transient Current Technique), were employed to study the response of a diamond detector

to various radiation fields over a large temperature range to evaluate its performance as a potential  $\mu\text{LoM}$ . Each of the ion beam techniques used specific signal processing chains, each of which was optimized to introduce the least amount of noise into the measurements. Data was collected from experiments conducted with the use of particle accelerators and neutron generators in the temperature range from 46 K to 295 K using, for this to work, a purpose-built test apparatus. The results of the measurements were analyzed and insight into the charge collection efficiency as a function of temperature and parameters affecting it are presented. Furthermore, the acquired signals from the detector were benchmarked and compared to theoretically expected signal shapes to facilitate with the process of creating a pulse shape discrimination technique to separate neutron from  $\gamma$ -ray radiation. The developed discrimination techniques were applied offline to the datasets collected during the experiments and their performance evaluated.

The structure of this work is as follows: section 2 discusses the interaction of ionizing and nonionizing radiation (neutrons) with matter and the various types of reaction that are possible with a specific emphasis on diamond. Section 3 expands this discussion by outlining how the interactions of radiation with a diamond lattice can be used to create a detector and also presents phenomenon which influence the performance of the detector. Section 4 is devoted to the signal processing chain required to properly acquire and process the information in the pulse from the detector. Section 5 provides an overview of discrimination techniques that are applied to the processed pulses from the detector in order to separate neutron and  $\gamma$ -ray events. Section 6 presents the apparatus built for the purpose of studying the performance of a diamond detector at cryogenic temperatures. Additionally, Monte Carlo based simulations which were used to set the experimental parameters are also presented along with the final signal processing chains used to acquire the experimental data. Section 7 outlines the steps taken to analyze the data obtained during the experiments. While in latter part of section 7, conclusions based on this data are presented and discussed. Two methods for pulse shape discrimination are also presented in this section and their performance evaluate.





## 2 INTERACTION OF RADIATION WITH MATTER

In order to understand how a single crystal diamond can be used as a radiation detector, it is important to understand how radiation interacts with matter. The interaction mechanism of radiation with the detector depends on the type of radiation, more specifically, is the radiation in the form of charged particles (ions, electrons), neutral particles (neutrons) or photons. Charged particles and photons lose energy predominantly through Coulomb interactions with the atoms and nuclei of the detector material and therefore can be detected directly. While neutral particles first must transfer part of their energy to charged particles inside the detector volume through collisions or nuclear reactions which can then be detected. The amount of energy a particle loses in matter can be quantified by means of macroscopic and microscopic interaction probabilities. Macroscopic probability of interaction for photons is usually defined as the linear attenuation coefficient which describes the interaction probability per unit path length. For charged particles this probability is described by the amount of energy lost per unit path length. Microscopic probabilities for all radiation types, called cross sections, are defined as the effective cross-sectional area of the matter to the incident radiation for a given interaction mechanism and is usually presented in Barn units, 1 barn is equal to  $10^{-28} \text{ m}^2$  [13].

### 2.1 Charged Particles

Fast charged particles (e.g. ions, electrons) interact with the detector material predominantly through the Coulomb force with atomic electrons of the detector material. In the case of ions, the energy transfer from the impeding ion to electrons in the material is small, therefore many collisions are required before the ion loses all of its energy resulting in a trail of ionization along its trajectory [14]. For heavy charged particles this mean energy loss, or stopping power, is described by the Bethe equation or more generally by the Bethe-Bloch equation and is valid over a larger energy range. The Bethe-Bloch equation with the low energy correction is presented below in equation 2.1:

$$-\frac{dE}{dx} = \frac{4\pi e^4 z^2}{m_0 v^2} NZ \left[ \ln \left( \frac{2m_0 v^2}{I} \right) - \ln \left( 1 - \frac{v^2}{c^2} \right) - \frac{v^2}{c^2} \right] \quad (2.1)$$

where  $v$  is the velocity and  $z$  is the charge of the primary particle,  $N$  is the number density,  $Z$  is the atomic number and  $I$  is the average ionization energy of the detector material,  $m_0$  is the electron rest mass and  $e$  is the electron charge. Note that for nonrelativistic particles where  $v \ll c$ , the last two term of the equation can be discarded [15]. From the Bethe-Bloch equation 2.1, it can be concluded that the energy loss is inversely proportional to the impeding ion velocity. Therefore, most of the ion energy is deposited at the end of its trajectory inside the detector resulting in a Bragg peak after which there is no more ionization. This phenomenon is illustrated in Figure 2.1 for 5.5 MeV alpha particles in diamond using the Stopping and Range of Ions in Matter simulation software (SRIM) which calculates the ionization profile using the Monte Carlo technique [16]. The width of the Bragg peak is a result of energy straggling which is caused by the energy loss being a statistical or stochastic process where not all particles transverse the same path in the material.

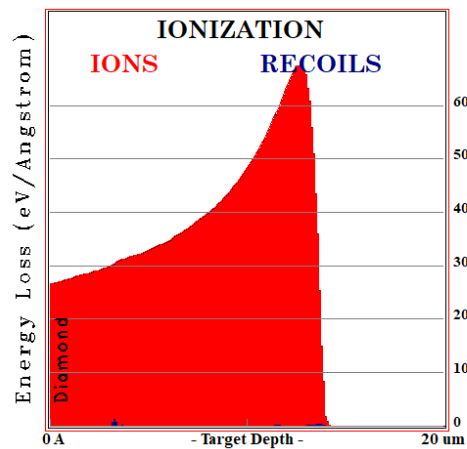


Figure 2.1 - Ionization profile of 5.5 MeV alpha particles in diamond.

The above equation is only valid for heavy ions and must be modified for lighter particles such as electrons. Fast electrons lose a larger fraction of their energy with each collision and have larger deviation in their trajectories due to their mass being equal to the electrons in the material. Additionally, electrons lose a significant portion of their energy through radiative process along with coulomb interactions. Radiative process such as bremsstrahlung is emitted when any charged particle decelerates. The amount of energy loss through bremsstrahlung depends greatly on the  $Z$  number of the detector material and increases as the size of the atoms in the detector material increase [17].

## 2.2 Photons

High energy photons, such as the those created by nuclear reactions ( $\gamma$ -rays), atomic inner shell ionization (x-rays) and electron bremsstrahlung, transfer their energy to the detector material predominantly through three mechanisms: photoelectric effect, Compton scattering and pair production. The energy transfer can be partial or complete and greatly depends on the energy of the incoming photon. The photoelectric effect dominates for lower photon energies, where the photon energy is completely transferred to a bounded electron which is then ejected from the inner atomic shells of an atom. The ionized atom consequently fills this vacancy by capturing a free electron or rearranging electrons from other shells. Relocation of electrons from outer shells to the K shell results in the emission of an X-ray photon. The atom can also de-excite through the emission of an electron from the outer shell. These emitted electrons are called Auger electrons [15], [17]. At intermediate photon energies, the Compton effect dominates where the incident photon is scattered off an electron, recoiling the electron and resulting in the emission of a lower energy photon. Furthermore, if the incident photon energy is more than twice the rest mass energy of an electron (1.02 MeV), pair production is possible. Pair production converts the photon energy into the creating of an electron-positron pair with all the energy above 1.02 MeV transferred equally to the kinetic energy of the created particles. Consequently, the positron annihilates with an electron resulting in the emission of two 511 keV gamma rays emitted in opposite directions to conserve momentum.

## 2.3 Neutrons

Neutrons carry no charge and therefore cannot interact with the detector directly through the Coulomb force as is the case for directly ionizing radiation. Neutrons interact almost exclusively with atomic nuclei through nuclear interaction that can be observed either as an elastic or nuclear reaction. In both cases, recoiled nuclei and nuclear reaction products are directly ionizing radiation types and as such can be used to indirectly detect neutrons.

Neutron capture is one of the most common nuclear reactions that take place when the neutron is absorbed by the detector material nucleus to form a compound nucleus. If the compound nucleus is left in the ground state, the reaction will be indistinguishable from neutron elastic scattering. In elastic scattering, the incident neutron transfers a portion of its energy to the atom ( $E_R$ ), which can

be calculated by scattering theory;  $E_R = \frac{4AE_n}{(1+A)^2}$  where  $E_n$  is the neutron energy and  $A$  is the mass of the material nucleus. In a diamond detector, a 1 MeV neutron will transfer 0.284 MeV of its energy to a carbon atom, which is about 28 % of its energy [18]. However, if the compound nucleus is left in an excited state, the scattering is inelastic and a nuclear reaction occurs. Scattering on nuclear potential, on the other hand, is always elastic, in which the incident neutron is scattered by the nucleus of an atom in the detector [13].

The probability of the type of reaction is heavily dependent on the incident neutron energy. This probability per unit path length is constant for a fixed neutron energy and is expressed in terms of cross section in units of the barn. Neutron elastic scattering or nuclear reaction cross sections are empirically derived through experiments and generally exhibit resonance behavior. Databases of cross sections are available online through the International Atomic Energy Agency's (IAEA) on their Experimental Nuclear Reaction Data (EXFOR) [19] and through the National Nuclear Data Center's (NNDC) Nudat [20]. Interactions are commonly divided into two groups, slow and fast neutrons interactions with fast neutrons being anything above 0.5 eV (the cadmium cutoff energy) [15].

### 2.3.1 Fast Neutrons

In general, nuclear reaction cross sections decrease with increasing neutron energy and scattering becomes the dominant neutron energy transfer mechanism. Due to the mass of a neutron, a significant amount of energy can be transferred in a single collision. These collisions displace atoms in the detector which produces a detectable signal. After each collision, neutrons lose energy to become slow neutrons in a process known as neutron moderation. Moderation is widely used in nuclear reactors to bring the neutron energy down to favorable levels for nuclear reactions. However, in some elements, nuclear capture channels open only at higher energy levels allowing for nuclear reactions to take place only with fast neutrons. In the context of this paper, we will focus on diamond, that is on carbon for which nuclear reactions are only possible for neutrons of higher energy. Table 2.1 summarized most common neutron induced nuclear reactions in carbon, however many more reactions with carbon exist [21].

Table 2.1 - Neutron induced reaction in carbon.

Reaction	Q-Value [MeV]	E <sub>th</sub> [MeV]
$^{13}\text{C}(n,\alpha)^{10}\text{Be}$	-3.836	4.134
$^{12}\text{C}(n,\alpha)^9\text{Be}$	-5.702	6.182
$^{12}\text{C}(n,n+2\alpha)^4\text{He}$	-7.275	7.886
$^{12}\text{C}(n,p)^{12}\text{B}$	-12.587	13.645
$^{12}\text{C}(n,d)^{11}\text{B}$	-13.732	14.887

The Q value in Table 2.1 depicts the energy required (endothermic) for the reaction while the E<sub>th</sub> represents the threshold energy at which such a reaction can occur. Using the Q value and a kinematic calculator (such as CATKIN [22]), the expected energy of the nuclear reaction products can be calculated. Taking the reaction of a neutron with  $^{12}\text{C}$ ,  $E_n - 5.702 = E_\alpha + E_{\text{Be}}$ . As will be later demonstrated, this is the key principle in detection of neutrons based on secondary products [23]. The reaction threshold energy (E<sub>th</sub>) can be observed for the  $^{12}\text{C}(n,\alpha)^9\text{Be}$  reaction in cross section data as illustrated by the grey line in Figure 2.2. The figure additionally contains the total, elastic, inelastic and (n,α) reaction cross section information for  $^{12}\text{C}$  in barns for incident neutrons in the energy range of  $0.5 < E_n < 20$  MeV. As can be observed from the figure, the alpha channel (grey line) opens at 6.182 MeV and peaks below 10 MeV.

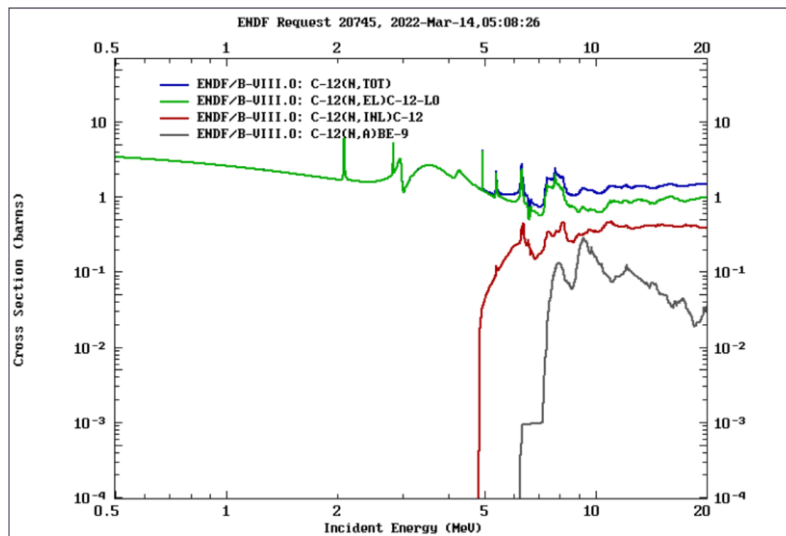


Figure 2.2 - Neutron cross section for  $^{12}\text{C}$  [19].

### 2.3.2 Slow Neutrons

In contrast to fast neutrons, very little energy is transferred by slow neutrons through elastic scattering, and they do not displace the atoms in the material by a detectable amount. These collisions eventually bring the neutron into thermal equilibrium with the material, which at room temperature is 0.025 eV. As depicted in Table 2.1, slow neutrons are not directly detectable with a diamond detector because their energy is lower than the threshold energy for required for nuclear reactions with C, and therefore a converter layer must be introduced to detect them. Most commonly a thin layer of  ${}^6\text{Li}$  or  ${}^{10}\text{B}$  is placed before the diamond detector to convert the neutron into other ionizing particles. The associated reactions and Q-values are summarized in Table 2.2, along with their cross sections in Figure 2.3.

Table 2.2 - Converter layer reactions for the detection of slow neutrons with a diamond detector.

Reaction	Q-Value [MeV]	Product Energy [MeV]
${}^6\text{Li}(n,\alpha){}^3\text{H}$	4.79 [24]	$E_\alpha = 2.06, E_T = 2.73$
${}^{10}\text{B}(n,\alpha){}^7\text{Li}$	2.792 [25]	$E_\alpha = 1.47, E_T = 0.84$

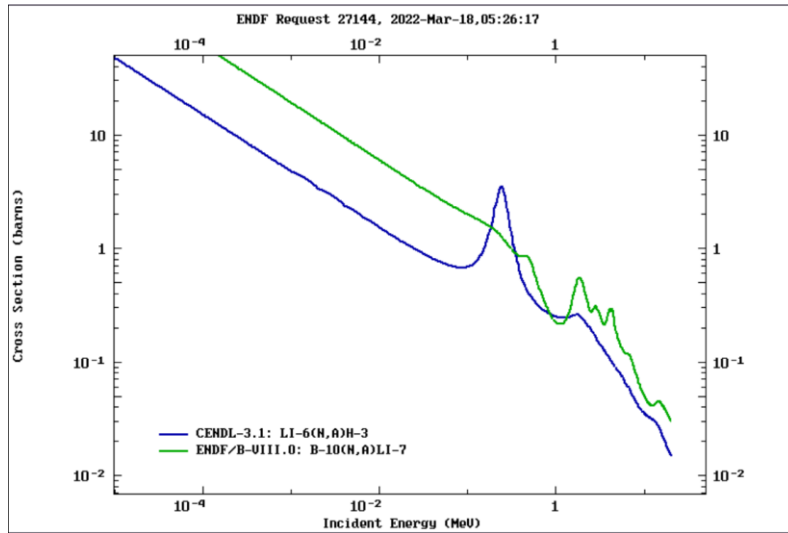


Figure 2.3 - Neutron cross section data for  ${}^6\text{Li}$  and  ${}^{10}\text{B}$  [19].

Both reactions release an alpha particle along with an ion which can be detected with the diamond detector. As is the case for fast neutrons, the energy of these secondary particles can be calculated using the Q-value of the reaction and a kinematics calculator. Additionally, from Figure

2.3 it can be observed that the reaction probability (cross section) is an order of magnitude higher than for the  $^{12}\text{C}(n,\alpha)^9\text{Be}$  for neutron energies under 1 MeV. Out of the two converters,  $^6\text{Li}$  is preferred even though it has a lower cross section, because of the high Q-values of the reaction. This high Q-value means that the reaction products have a larger kinetic energy making them easier to detect in the diamond and less sensitive to the converter layer thickness. Typical energies of the alpha particle generated from the  $^{10}\text{B}$  and  $^6\text{Li}$  are 1.47 MeV and 2.06 MeV, respectively resulting in a penetrating depth of 7.8  $\mu\text{m}$  in  $\text{B}_2\text{O}_3$  and 19.5  $\mu\text{m}$  in  $\text{LiF}$  [26].

## 2.4 Neutron generation

In order to perform experiments with neutrons, a stable, preferably monoenergetic source of neutrons of an appropriate energy are required. In this section, we will briefly outline the most common methods of generating neutrons for experiments as it is important to understand the reactions involved to correctly interpret spectrum data obtained from the detector. Neutron sources are divided into two categories, radioisotope sources and accelerator reaction-based sources. Both types of sources release an array of secondary products along with a neutron in the form of  $\gamma$ -ray, x-ray radiation as well as other ions which are used to calculate the neutron flux but also add a significant background to the detector being tested. Table 2.3 summarizes applicable neutron sources of importance for this work [27]. Furthermore, for simulating a fusion environment, Deuterium-Deuterium (D-D) and Tritium-Deuterium (T-D) are used, as the majority of fusion devices are based on these reactions [26].

Table 2.3 - Neutron source reactions.

	Neutron Energy [MeV]	Properties
<b>Radioisotopes</b>		
$^{252}\text{Cf}$	2.1	Average energy - Broad spectrum neutrons
$^{241}\text{Am}^9\text{Be}$	4.2	
<b>Accelerator induced reactions</b>		
$^7\text{Li}(p,n)^7\text{Be}$	0.2 – 0.7	Monoenergetic - Neutron energy based on primary ion energy
$^3\text{H}(p,n)^3\text{He}$	0.7 – 3	
$^2\text{H}(^2\text{H},n)^3\text{He}$ (D-D)	3.5 – 8	
$^3\text{H}(p,n)^3\text{He}$	3 – 13	
$^3\text{H}(^2\text{H},n)^4\text{He}$ (T-D)	14 – 20	



## 2.5 Distinguishing radiation by interaction volume

As was introduced in section 1, the main motivation for this work came from the fact that diamond detectors have been selected to function as  $\mu\text{LoM}$  as part of the beam diagnostic system for the IFMIF DONES accelerator. These monitors have the task of measuring scattered radiation along the beam axis of the accelerator, with the capability to distinguish the two most important components of the expected radiation, namely, neutrons and  $\gamma$ -rays. The most conventional approach for this purpose is based on the fact that different radiation types are absorbed in the detector materials in different interaction volumes.

These interaction volumes depend also on the energy range that needs to be detected, more specifically, the range of energies expected at the position of the  $\mu\text{LoM}$  in the DONES environment. According to simulation given by Marroncle et al [5] neutron with energies around 0.5 to 5 MeV and  $\gamma$ -rays up to 10 MeV in energy are expected at the location of the first  $\mu\text{LoM}$ . Under these circumstances, it can be assumed that the dominant energy loss mechanism in materials for  $\gamma$ -rays will be Compton scattering, while for neutrons it will be elastic scattering and nuclear reactions ( $n,\alpha$ ) for higher neutron energies. Since Compton electrons and photons are weakly ionizing particles, they lose their energy in many subsequent events in rather large detector volumes (hundreds of micrometers), which is very different from neutron interactions. If scattered, neutrons give a portion of their energy to recoil carbon ions (or alpha particles if nuclear reactions occur), which are stopped in small distance of up to 10 micrometers. The various mechanisms of radiation detection in detectors are illustrated in the Figure 2.4. Each of these mechanisms will be discussed in more detail and in the context of a diamond detector in chapter 3.

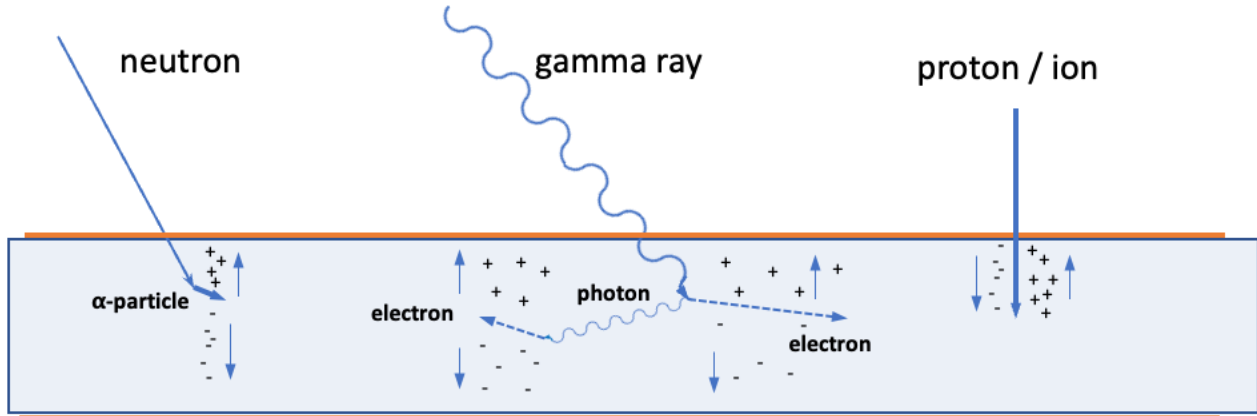


Figure 2.4 - Various mechanisms of radiation detector based on interaction volume.

Considering this, it is evident that investigations of processes that occur in detectors that are supposed to discriminate different radiation types can be studied only with techniques that utilize radiation types that can change the interaction volume and therefore emulate the expected environment in the DONES accelerator. Since the only radiation for which the energy range can be easily changed in the MeV region are protons and other heavier ions, accelerator-based techniques have been used.



### 3 RADIATION DETECTION WITH DIAMONDS

A typical diamond radiation detector is composed of an electronic grade single crystal diamond sandwiched between two coplanar electrodes on each side and operates as a solid-state ionization chamber [28]. Unlike narrow-band semiconductors where a PN-junction must be fabricated by doping to form a sensitive volume with low charge carrier concentrations, diamond is a wide-band semiconductor, and it intrinsically contains low charge carrier concentrations. Therefore, the sensitive volume is defined by the size (area) of the electrodes and the thickness of the diamond. Decelerating charged particles produce electron-hole pairs in the detector by promoting electrons from the valence band into the conduction band. If no external electric field is present, the free charge carriers diffuse in random directions with a thermal velocity. However, if an external field is applied across the diamond by placing a large potential difference between the electrodes, the generated charge carriers then drift towards the electrodes under the influence of this external electric field. The number of e-h pairs generated is proportional to the deposited energy from the charged particle and can be calculated by dividing the deposited energy by the average energy required to generate an e-h pair ( $E_{\text{pair}}$ ), which in diamond is approximately 13.6 eV [29]. However this is only true if the carrier lifetime is much larger than the carrier drift time [30]. Charge carrier mobility and lifetime are affected by many factors such as the purity of the crystal lattice (concentration of defects), but also on temperature, as it will be discussed in detail in section 3.2.

The properties of diamond compared to silicon and germanium are summarized in Table 3.1. As some values vary in literature, these are therefore presented here in a range [3], [29]–[33]. Additionally, the last column in Table 3.1 highlight how the specific properties benefit a detector based on diamond.

*Table 3.1 Comparison of diamond detector properties with other detector materials.*

	<b>Diamond</b>	<b>Silicon</b>	<b>Germanium</b>	<b>Diamond Advantage</b>
Atomic Number (Z)	6	14	32	Radiation hardness
Bandgap [eV]	5.48	1.12	0.67	Lower noise
Dielectric strength [V/cm]	$10^7$	$3 \cdot 10^5$	$10^5$	Large bias
Intrinsic resistivity [ $\Omega/\text{cm}$ ]	up to $10^{16}$	$2.3 \cdot 10^5$	50	Lower leakage current

Electron mobility [ $\text{cm}^2/\text{Vs}$ ]	1300 - 4500	1350	3900	Fast response
Hole mobility [ $\text{cm}^2/\text{Vs}$ ]	1800 - 3800	480	1900	Fast response
Electron lifetime [s]	$10^{-10}$ - $10^{-6}$	$> 10^{-3}$	$> 10^{-3}$	Better charge collection
Hole lifetime [s]	$10^{-10}$ - $10^{-6}$	$10^{-3}$	$2 \cdot 10^{-3}$	Better charge collection
Dielectric constant	5.72	11.9	16	Low capacitance
Displacement energy [eV]	43	13 - 20	28	Radiation hardness
Energy to create e-h pair [eV]	11.1 - 24	3.62	2.96	Disadvantage - lower output signal

The large range of values reported in Table 3.1 results from variations in the quality of diamonds used for detectors. Most of the highest quality diamonds are manufactured using the chemical vapor deposition (CVD) method, where a diamond is grown layer by layer from a seed. Using this method single crystal CVD (scCVD) or polycrystalline (pCVD) can be manufactured. scCVD diamonds are preferred for detector use since they have no grain boundaries resulting in fewer traps for charge carriers. This improves the charge collection efficiency and output signal amplitude up to a factor of 3 in comparison to pCVD diamonds [6]. Electronic grade scCVD diamonds have less than 5 ppb of nitrogen and boron impurities. However, they are significantly more expensive, and their size is limited to approximately 5 x 5 mm. pCVD diamonds are not limited in size, cheaper to manufacture and therefore preferred in some applications where a lower charge collection efficiency can be tolerated under the benefits of a larger detector area.

Furthermore, as depicted in Table 3.1, the energy required to eject an electron into the conduction band, the bandgap energy ( $E_g$ ), is 5.47 eV while the average energy required to create an e-h pair is much higher. This is due to non-ionizing energy losses as a portion of the incident particle energy  $E_0$  goes into the creation of phonons.

$$E_0 = E_{ph}N_{ph} + E_gN_i \quad (3.1)$$

$E_{ph}$  and  $N_{ph}$  represent the average phonon energy and number of phonons, respectively while  $E_g$  is the bandgap and  $N_i$  is the number of e-h pairs created. Therefore, approximately 8 eV (60 % of the energy) goes into the creation of phonons. A further benefit of the relatively large bandgap energy

of diamond compared to silicon (1.12 eV), is a lower noise in the signal from the detector due to insufficient thermal energy at room temperature to generate electron hole pairs.

Furthermore, with the incident energy (of the incoming radiation) being fixed, equation 3.1(3.1) can be rewritten in terms of the fluctuation in the number of phonons and e-h pairs as follows [31]:

$$E_g \Delta N_i = E_{ph} \Delta N_{ph} \quad (3.2)$$

thus, over many events the standard deviation in the number of e-h pairs, which is the intrinsic resolution of the detector, can be written as

$$\sigma_Q = \sqrt{F \frac{E_0}{E_{pair}}} \quad (3.3)$$

where F is known as the Fano factor. The Fano factor ranges from 0.08 to 0.14 for semiconductor materials. There is no reliable experimental data for the diamond Fano factor, but it has been theoretically predicted to be 0.08. The Fano factor for silicon is 0.115 [30], [34].

### 3.1 Signal generation

When the incoming radiation creates a large number of charge pairs in a diamond crystal, these generated charge carriers drift through the material with a drift velocity which is proportional to the electric field strength (E). This proportionality constant is defined as the mobility ( $\mu$ ) and has units of  $\text{cm}^2/\text{Vs}$ . Theoretically, the drift velocity can increase indefinitely with increasing electric field strength, however in practice there is a limit to the maximum drift velocity due to increased phonon scattering. This maximum drift velocity is known as the saturation velocity. Considering the saturation velocity ( $v_s$ ), the drift velocity ( $v_{dr}$ ) is expressed as a function of the low field mobility ( $\mu_0$ ) as [35]:

$$v_{dr} = \frac{\mu_0 E}{1 + \frac{\mu_0 E}{v_s}} \quad (3.4)$$

however, this is only an approximation for ideal conditions such as infinite coplanar electrodes. The real drift velocity is position dependent since the electric field is dependent on the detector electrode configuration. The general expression for drift velocity can be obtained by the differential equation  $\frac{dx}{dt} = \mu(E)E(x)$  [29]. As is the case with charge carrier mobility values in diamond (Table 3.1), the saturation velocity also varies in literature values and is in the range of  $1.2 \times 10^5$  m/s to  $9.6 \times 10^5$  m/s and  $1.2 \times 10^5$  to  $14.1 \times 10^5$  m/s for electrons and holes at room temperature, respectively [29], [35].

As the charge carriers move inside the diamond under the influence of the electric field, they induce current in the electrodes of the detector as described by the Shockley-Ramo theorem [36]. Shockley-Ramo showed that the current on the electrode is the sum of the electrostatic influence of the charges at each moment as they drift inside the diamond. The resulting current on the detector electrode is described by the following equation simplified for the case of a detector configured as a parallel plate capacitor.

$$I = q \frac{v_{dr}}{d} \quad (3.5)$$

$q$  is the charge of the electron and  $d$  is the thickness of the detector. The drift velocity can be also simplified to  $v_{dr} = \mu E$  from equation 3.4(3.4) by disregarding the saturation velocity, resulting in an expression for the current from the detector:

$$I = q \frac{\mu_0 E}{d} \quad (3.6)$$

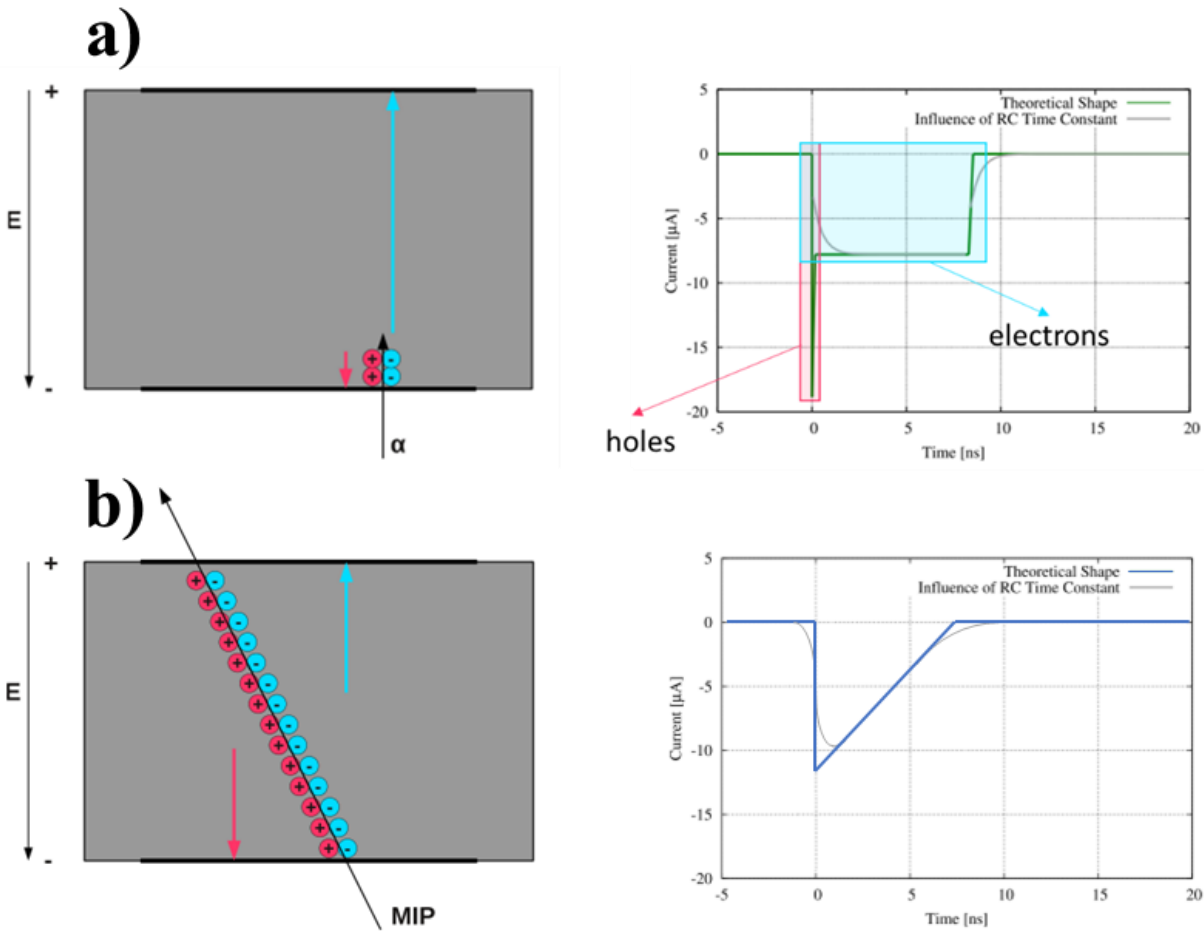


Figure 3.1 - Induced current from a) alpha particle and b) minimum ionizing particles (MIP) [29], [31].

The induced current is the superposition of the contribution of electrons and holes as they drift towards opposite electrodes. Figure 3.1 illustrates two extreme cases, one for charge particles that have very small range in the detector (alpha particles) and one that traverse through the whole detector volume. The latter one is referred to as the minimum ionizing particle (MIP), usually a relativistic high energy electron that has constant energy loss. These two cases are selected as they represent a similar response of a diamond detector to neutrons, which are detected by alpha particles from neutron induced reactions, and  $\gamma$ -rays which are detected through a number of uniformly spread electrons.

The induced current resulting from an alpha particle impinging a diamond detector with coplanar electrodes is often measured using the decay of a  $^{241}\text{Am}$  radioisotope that produces an



alpha particle with energy of 5.5 MeV which penetrates 14  $\mu\text{m}$  into diamond [16]. This produces on average  $4.04 \times 10^5$  e-h pairs using the average energy required to create an e-h pair ( $E_{\text{pair}}$ ) to be 13.6 eV as stated above, corresponding to 65 fC of charge deposited in the diamond.

$$Q_0 = \frac{qE_\alpha}{E_{\text{pair}}} = 65 \text{ fC} \quad (3.7)$$

$$N_{eh} = \frac{E_\alpha}{E_{\text{pair}}} = 4.04 \times 10^5 \quad (3.8)$$

The generated electrons have to transverse the full thickness of the diamond to reach the positive electrode, while generated holes travel only 14  $\mu\text{m}$  to reach the negative electrode. For a typical thickness of a diamond detector of 500  $\mu\text{m}$  and 1 V/ $\mu\text{m}$  electric field the maximum transit times for electrons and holes are given in Table 3.2 [29]:

Table 3.2 - Transit time for charge carriers [29].

	$v_{\text{dr}}$ [m/s]	d [ $\mu\text{m}$ ]	t [ns]
Electrons	$6 \times 10^4$	500	8.3
Holes	$8.5 \times 10^4$	14	0.165

From the graph on the right of Figure 3.1a, the influence of each charge carrier on the total induced current on the electrodes can be observed. The short transit time for holes (165 ps) results in a current spike while electrons travel 8.3 ns through the bulk of the diamond detector to reach the other electrode. The current  $I = \frac{Q_0}{t} = 7.8 \mu\text{A}$  which, when measured through a 50  $\Omega$  based system, results in a 0.4 mV signal. Furthermore, not all the charges are instantaneously accelerated towards the electrodes as the outer charge carriers in the generated charge cloud screen the inner charge carriers from the electric field. This affects the rise time of the current pulse as not all the charge carriers reach the drift velocity at the same time. This effect is compounded by the RC constant of the system which limits the bandwidth, causing the hole contribution to be difficult to observe resulting in a signal depicted by the gray curves in Figure 3.1 [29]. This will be further discussed later in section 7.3.

An alpha particle of sufficiently low energy to stop inside the volume of the detector was used to illustrate the basic principle of charge generation and collection inside a diamond detector. Here, it is important to note that if an alpha particle is induced by a neutron, the interaction point will not be always on the surface. In these cases, a spike observed in Figure 3.1a will become wider, depending on the depth of the interaction. The shape of the signal will still have two components, the first one (higher) consisting of the contribution of both charge carriers and the second one (lower) consisting of the contribution of just one charge carrier, the one that must travel a longer path [37].

The resulting current profiles are very different for MIPs, which transverses the whole volume of the detector and do not stop in the detector. A MIPs particle deposits 36 e-h pairs per  $\mu\text{m}$  in diamond ( $E_e/h$ ) [38], therefore passing through a detector of 500  $\mu\text{m}$ , the particle will deposit only  $Q_0 = E_e/h \cdot d \cdot q = 2.9 \text{ fC}$ . Signal generation for MIPS, that are essentially relativistic electrons, is similar to  $\gamma$ -rays which lose energy in many different interactions, but mostly through Compton scattering and photoelectric effect. The result of these interactions are many electrons that are distributed mostly uniformly and are losing energy within the large detector volume.

Therefore, as it can be concluded from the above considerations, the shape of the signal will depend very much on the type of radiation being detected by the diamond detector. In practice, experimental current profiles may be even more complex and will be studied in more detail in section 7.3.

The performance of a diamond detector is graded by the charge collection efficiency (CCE) or by the charge collection distance (CCD). The CCE is defined as the total measured charge over the total generated charge (3.9), and equals one for the ideal detector. In realistic devices, there are defects that can trap charges, which can be described by the CCD which is the average distance that charge carriers travel before being trapped (3.10). The CCD can also be defined in terms of electron mobility ( $\mu$ ) and lifetime ( $\tau$ ) [38].

$$CCE = \frac{Q_m}{Q_0} \quad (3.9)$$

$$CCD = \frac{Q_m}{Q_0} d \quad (3.10)$$

$$CCD = (\mu_e \tau_e + \mu_h \tau_h)E \quad (3.11)$$

Taking into account the trapping and detrapping of charge carriers influence on the CCE, we arrive at the Hecht equation [39]:

$$CCE = \frac{\mu_h \tau_h E}{d} \left( 1 - e^{\left(\frac{-z}{\mu_h \tau_h}\right)} \right) + \frac{\mu_e \tau_e E}{d} \left( 1 - e^{\left(\frac{z-d}{\mu_e \tau_e}\right)} \right) \quad (3.12)$$

These quantities give an insight to the quality of the diamond detector because charge carriers that get trapped while drifting towards the electrodes stop contributing to the total measured induced charge. Under ideal conditions, all charge generated by an impinging ion is measured as it drifts towards the electrodes. However, charge carriers can be trapped and/or recombined before reaching the electrode resulting in a decrease in the CCE [33]. Unirradiated scCVD based diamond detectors typically have 100 % CCE while pCVD detectors only achieve between 40 % to 60 % CCE. This is mainly due to charge losses at the grain boundaries [40].

### 3.2 Effects of defects in diamond on charge transport

Any distortion to the periodicity of the diamond lattice or the addition of different impurities, influences the electronic and phononic transport properties of the material and possibly creates traps for the generated charge carriers. The charge carrier lifetime is inversely proportional to the trap density ( $n_{\text{trap}}$ ), carrier thermal velocity ( $v_{\text{th}}$ ) and trapping cross-sections ( $\sigma$ ).

$$\tau = \frac{1}{\sigma v_{\text{th}} n_{\text{trap}}} \quad (3.13)$$

The energy levels of these traps can be located in the bandgap, stopping the charge carriers from drifting towards the detector electrodes. Once trapped, the charge carriers can be detrapped at a later time or recombine leading to a lower detector CCE [41]. Charge carriers can be promoted back to the conduction band by phonons, however this detrapping time is exponentially proportional to the lattice temperature. It ranges from ps at room temperature and increases to  $\mu\text{s}$  at cryogenic temperatures [31].

At cryogenic temperatures, which is the focus of this work, the dominant mechanism of charge carrier trapping is hypothesized to be due to the creation of excitons. Excitons were first proposed by Y. Frenkel in 1931 and have since been observed in silicon and in diamond [42]. When an

electron is promoted to the conduction band leaving behind a hole, due to the Coulomb force, the electron can be bounded to the hole in a hydrogenic state, this state is referred to as an exciton. The binding energy of this bond is  $80.0 \pm 0.5$  meV [43]. The exciton lifetime at room temperature is very short due to the energy in the diamond lattice being high enough to break the exciton bond and promote the electron to the conduction band. However, at cryogenic temperatures, this is not the case and the exciton lifetime increases significantly. The increased lifetime of the exciton also increases the probability that the exciton will recombine (the electron and hole will recombine). This recombination leads to less charge carriers drifting in the detector and therefore less current induced on the electrodes. The lifetime of an exciton is the combination of two processes,  $\frac{1}{\tau} = \frac{1}{\tau_{rec}} + \frac{1}{\tau_{evap}}$ , where  $\tau_{rec}$  is the recombination lifetime and  $\tau_{evap}$  is the evaporation lifetime. Both of which are temperature dependent. Table 3.3 summarizes the exciton lifetime with temperature [31]. The recombination time at lower temperatures was not found in literature.

Table 3.3 - Exciton lifetime dependence on temperature [31][44].

<b>T [K]</b>	<b><math>\tau_{evap}</math></b>	<b><math>\tau_{rec}</math></b>
300	30 ps	< 10 ns
100	10 ns	10 ns
50	150 $\mu$ s	

However, in the presence of a large electric field, the electron and hole pair should start drifting as soon as they are created, decreasing the probability of entering into an exciton state. It is theorized by Jansen [31], [45] that this is not observed due to a not even distribution of the electric field in the volume of generated e-h pairs.

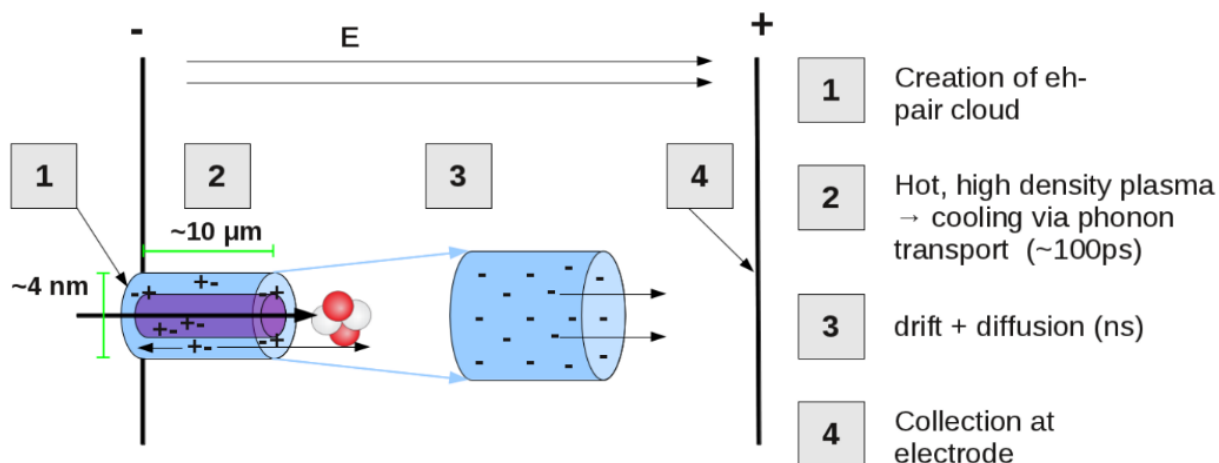


Figure 3.2 - e-h pair screening effect [46]

As illustrated in Figure 3.2, as a particle impacts the diamond detector (an alpha particle is illustrated), it creates a plasma cloud of e-h pairs along its trajectory. The dimensions of this plasma cloud depend on the type and energy of the impinging ion. Due to the density of this plasma cloud, e-h pairs located inside the plasma cloud are influenced less by the external electric field effectively decreasing the rate of separation of the charge carriers. This screening effect increases the probability of exciton formation inside the plasma cloud leading to recombination and only the e-h pairs located on the outside of the plasma cloud contribute to the induced current of the detector electrodes [31]. This implies that the amount of charge carriers collected in the inner region of the plasma cloud depends on the strength of the electric field. Therefore, if a higher bias voltage is applied across the detector, the CCE should increase at cryogenic temperatures. Furthermore, impinging radiation which creates a plasma cloud of lower density will be less affected by this phenomenon.

### 3.3 Polarization phenomenon in scCVD diamond

In the context of charge carrier transport, it is also important to mention that not all charge carriers trapped in defects recombine instantly but accumulate in defect sites along their drift path in the diamond bulk. This leads to a phenomenon known as polarization which can significantly decrease the CCE of the detector. Holes drift toward the negative electrode, resulting in a higher density of holes being trapped closer to the negative electrode. While electrons drift towards the positive electrode, resulting in a higher density of trapped electrons closer to the positive electrode.

The separated trapped charges create an internal electric field which acts in the opposite direction to the external electric field created by the application of a bias potential at one of the detector electrodes, effectively decreasing the electric field strength in some regions of the detector. This is visually depicted on the right hand side of Figure 3.3 [47].

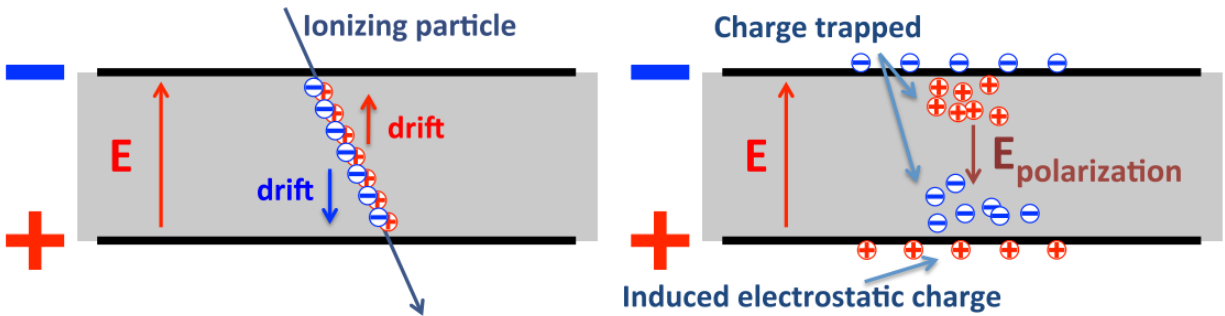


Figure 3.3 - Polarization [47].

The decreased electric field strength increases the probability of recombination and deteriorates charge transport properties resulting in lower charge collection. The degree of polarization is not constant but increases with more accumulated charge causing drastic differences in experiments depending on the fluence of radiation. Furthermore, the built up space charge can be randomly detrapped causing a sudden burst of charge carriers at random periods [33]. Polarization is not only affected by the space charge in the bulk of the detector but is also affected by the type of contact between the detector electrode and diamond. A Schottky contact can enhance the trapping of charge carriers leading to more polarization [48].

For experiments to be accurate and reproducible, steps must be taken to mitigate the effects of polarization. As polarization cannot be completely avoided, it can be minimized or reversed during an experiment by applying one of the following techniques [31], [47], [49]:

- **Limiting the particle flux on the detector:** Decreasing the number of e-h pairs generated will decrease the amount of space charge trapped in the detector, minimizing polarization.
- **Increasing the bias (external electric field strength):** Decreases the probability of charge trapping and more space charge has to accumulate to polarize the detector to the same degree.

- **Alternating the bias (changing the bias polarity):** Switching the polarity of the external electric field will cause the trapped space charge to move in the opposite direction and recombine effectively depolarizing the detector.
- **Detrapping charge carriers using light:** Diamond is a wide bandgap semiconductor and not sensitive to visible light. However, light will have enough energy to promote trapped charges into the conduction band from trap levels inside the bandgap.

### 3.4 Low temperature dependences

Unlike with silicon detectors, lowering the temperature of a diamond detector does not decrease the noise level significantly due to the low intrinsic free charge carrier concentration [50]. Diamond is a wide bandgap semiconductor and at room temperature, the lattice does not have enough energy to promote electrons across the bandgap. However, as with silicon detectors, the mobility of charge carriers does increase due to lower lattice vibrations as the temperature is decreased [51]. The mobility along with the drift velocity saturates to a maximum value below 100 K [31], [45], [52]. Furthermore, negative differential mobility (NDM) was also observed in diamond below 140 K. Negative differential mobility occurs when the electron mobility decreases with increasing electric field strength. NDM can lead to Gunn oscillations, introducing a high frequency oscillation to the output current of the detector. This was only observed at low electric field strengths under  $0.2 \text{ V}/\mu\text{m}$  [53].

Literature on diamond detector behavior at temperatures under 80 K is very scarce. As mentioned earlier, only a few research papers were found for the study of radiation hardness and charge transport at cryogenic temperatures. The most relevant work is by Jansen [31] and Sauer [54] who investigate the charge mobility in diamond from room temperature to 2 K and discovered a significant drop in detector efficiency which was attributed to exciton recombination. The results of this work are summarized in Figure 3.4. Figure 3.4 illustrates the measured charge for a 5.5 MeV alpha particle hitting a diamond detector in the temperature range  $2 \text{ K} < T < 300 \text{ K}$  for electrons and holes. In both figures, at 300 K, all of the deposited charge is measured, the CCE is 100 %. However, as the temperature decreases the amount of charge measured starts to decrease sharply around 150 K before reaching another lower plateau around 60 K. The measured charge decreases with temperature while the deposited charge is constant.

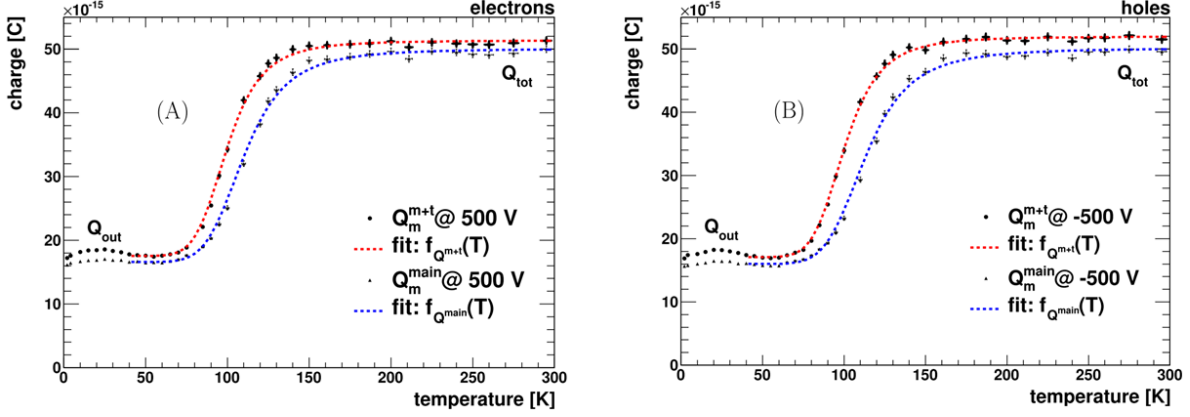


Figure 3.4 - Measured charge as a function of temperature [31].

Recently, diffusion and lifetimes of excitons in diamond at cryogenic temperatures were investigated in more detail with the motivation of developing deep ultraviolet emitting diodes. The large binding energy of excitons in diamond leads to light emission at 235 nm at room temperature which is effective for use in sterilization but still safe for human exposure [55]. Since it is postulated that the main reason so the decrease in CCE of a diamond radiation detector at cryogenic temperatures is due to the formation and recombination of excitons, the results of work in this field are also explored. It is observed that the density of excitons in a charge cloud of free carriers varies with the total carrier density and temperature. This relationship can be modeled using the mass-action law, which is also referred to as the Saha equation:

$$\frac{n_{eh}^2}{n_{ex}} = AT^{\frac{3}{2}} e^{\left(\frac{-E_{ex}}{k_B T}\right)} \quad (3.14)$$

the ratio of free carrier density ( $n_{eh}$ ) to the exciton density ( $n_{ex}$ ) is dependent on temperature ( $T$ ), exciton binding energy ( $E_{ex} = 80$  meV), Boltzmann constant ( $k_B$ ) and a coefficient  $A$  which represents the exciton density of states and was experimentally estimated to be  $4.4 \pm 2.7 \times 10^{14} \text{ cm}^{-3} \text{ K}^{-3/2}$  [56]. From equation 3.1, it can be concluded that the density of excitons is significantly higher at cryogenic temperatures because fewer excitons have enough thermal energy to overcome the binding energy ( $E_{ex}$ ).



### 3.5 CCE measuring techniques at low temperatures

Under these conditions it is important to find an appropriate method that can be used to evaluate the performance of a diamond detector at low temperatures, taking into account the intended final application. Unfortunately, as the detection of a wide range of radiation types is required, the pool of available techniques that can be used to test the capabilities of a diamond detector is rather small.

In the laboratory environment, the most frequent technique used to test semiconductor detectors in general is the Transient Current Technique, TCT. It utilizes excitation by intensive and pulsed ( $< 1$  ns) laser light to create charge carriers, which are then measured as a current signal at the detector electrodes using a fast storage oscilloscope. The wavelength of the laser light depends on the material being studied, therefore the most frequent setup is adjusted for silicon utilizing a red laser light. TCT systems for diamond are less available as they should utilize ultraviolet lasers to be able to induce current signals in the wide band gap diamond material [55]. Unfortunately, to simulate strongly localized ionizations that are expected from neutron detection events, the intensity and controllability of the pulsed laser light for the TCT technique are at present not available. Another alternative would be the two photon, TP-TCT technique, a novel technique that is based on the absorption of two photons in the same time [57]. However, this technique is also not appropriate as it does not have the capability to enable high ionization densities. Another version of this technique is the alpha particle TCT technique that was used originally by Jansen [45]. However, in this experimental setup, utilizes only alpha particles at a fixed energy and is therefore very limited. Simulating the conditions required for  $\mu$ LoM in DONES with this technique would be very difficult.

The only technique that could be capable of fulfilling all the requirements, that is spatial sensitivity and the capability of using different radiation types, is the Ion Beam Induced Charge technique, IBIC. IBIC is only available in several accelerator laboratories worldwide, including IRB. However, it has to be stated that none of the IBIC setups available worldwide before this work are capable of measuring with a diamond detector at low temperatures required for the development of  $\mu$ LoM for the DONES accelerator. Therefore, the setup had to be designed and constructed for this purpose, the development of each component of this setup is presented in chapter 6.

## 4 DETECTOR SIGNAL PROCESSING

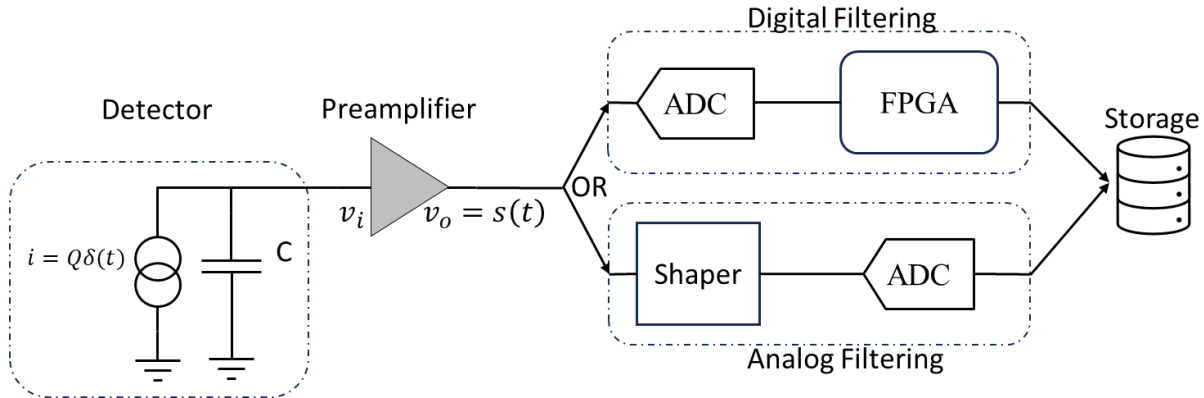


Figure 4.1 - General signal processing chain used to acquire signals from an ionizing radiation detector.

A typical signal processing chain for ionizing radiation detector is illustrated in Figure 4.1. It consists of a detector, preamplifier, filtering/shaping section which digitizes the signal and stores it on a computer. The two parallel filtering strategies shown in Figure 4.1 represent the two most common methods used in nuclear instrumentation based on a literature review. The analog filtering method was preferable in the past, but it is slowly being outperformed by the digital strategy due to the speed and quality of modern ADCs [58]. The detector is presented as a current source in parallel with a capacitor. The capacitor is added to model the real device as all detector material has some inherent capacitance which affects the output signal. The current generated from impinging radiation on the detector can be approximated by a current pulse which is mathematically described by a delta function. This small current pulse is passed to a preamplifier which amplifies the signal and, depending on the application as will be discussed in the text, can also integrate the current pulse. The output of the preamplifier is further processed in the analog or digital domain to increase the signal to noise ratio and adapt the signal so the required information can be extracted from it. A simplified diagram of the pulse expected after each stage of the signal processing chain containing an integrating (charge sensitive) preamplifier and an analog shaper/filter are illustrated in Figure 4.2.

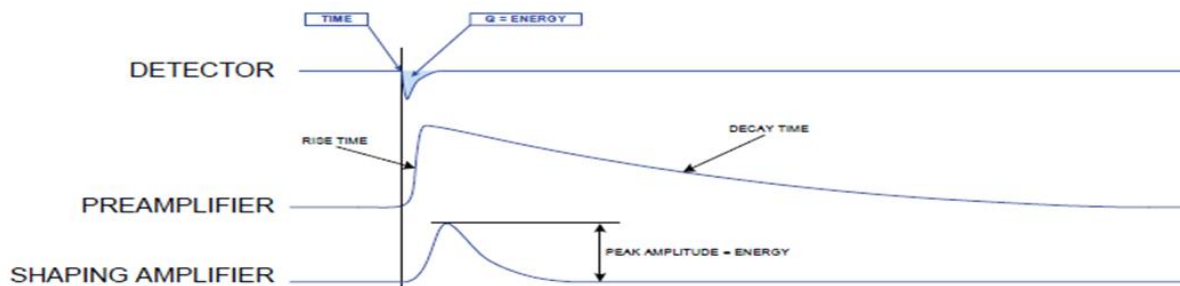


Figure 4.2 - Typical pulse expected at the output of the detector, integrating preamplifier and after analog filtering stage. The height of the shaped pulse is proportional to the deposited energy of the impinging radiation. [58].

The previous section of this work focused on the generation of the signal in the detector and all the possible shapes that are theoretically expected. This section however describes the next steps in the signal processing chain, starting with the preamplifier in section 4.1 and the shaping/filtering stage in section 4.3. Section 4.2 is dedicated to the theoretical analysis of noise sources which influence the design of shaping filters.

#### 4.1 Preamplifiers for radiation detectors

As described above, the signal level at the output of a diamond detector is very small and amplification is required followed by signal processing to extract information and to limit the influence of noise. This is achieved by placing a preamplifier as close as possible to the detector. There are three types of preamplifiers used with radiation detectors: voltage sensitive, current sensitive and charge sensitive amplifiers. For the scope of this work, the focus will be on the latter two.

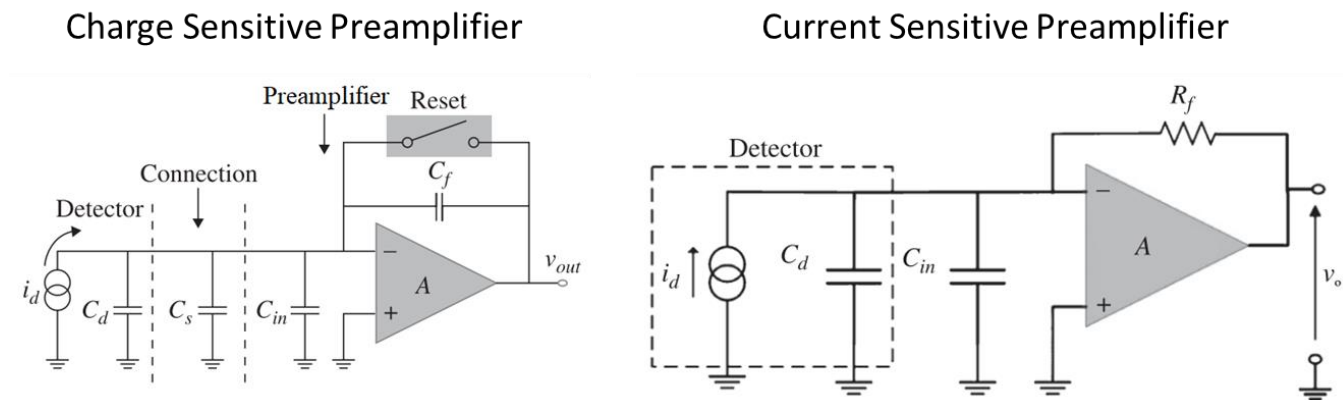


Figure 4.3 - Charge Sensitive and Current Sensitive Preamplifier schematic [59].

The voltage at the output of the charge sensitive preamplifier (schematic on the left of Figure 4.3) is obtained by:

$$v_{out} = -\frac{Q_0}{\frac{A+1}{A}C_f + \frac{C}{A}} \quad (4.1)$$

where  $C = C_d + C_{in} + C_s$ , that is the sum of the detector, cable, and preamplifier capacitance, respectively. Most preamplifiers have a large open loop gain ( $A \gg 1$ ), and the output voltage can be approximated to:

$$v_{out} \approx -\frac{Q_0}{C_f} \quad (4.2)$$

therefore, the output voltage is determined by the feedback capacitor. In practice, not all charge induced in the detector is transferred to the feedback capacitor, some is lost to other input capacitances. The ratio of the charge transferred to the preamplifier can be expressed as:

$$\frac{Q_f}{Q_0} = \frac{Q_f}{Q_{loss} + Q_f} = \frac{1}{1 + \frac{C}{(A+1)C_f}} \quad (4.3)$$

Decreasing the sum of input capacitances ( $C$ ) results in more induced charge to be transferred to the feedback capacitor. Therefore, it is better to use detectors with low capacitance and minimize the cable length between the detector and the preamplifier. Charge sensitive preamplifiers are characterized by a parameter called sensitivity which is expressed in units of mV/MeV, as defined for silicon. Combining equations 3.7 and 4.2, yields the sensitivity parameter:

$$\frac{v_{out}}{E} = \frac{q}{E_{pair}C_f} \quad (4.4)$$

In the charge sensitive preamplifier schematic on the left of Figure 4.3 a reset switch is shown which is required to discharge the feedback capacitor, otherwise the output voltage would saturate. There are many reset strategies employed in preamplifiers, however the most common one is the introduction of a large resistor parallel to the feedback capacitor which allows for continuous discharging.

There are two main ways of connecting the detector to the preamplifier and the high voltage supply: AC coupling through a capacitor or DC coupling without the capacitor as illustrated in Figure 4.4.

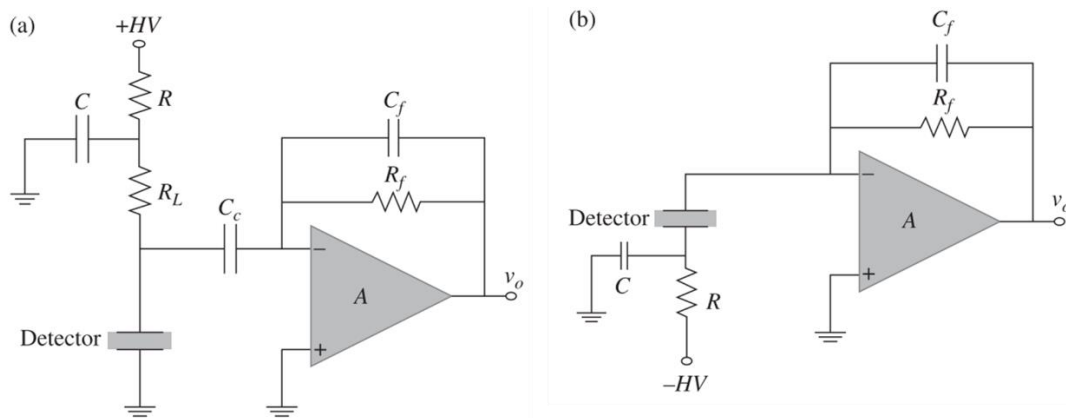


Figure 4.4 - Detector Coupling [59].

The coupling capacitor ( $C_c$ ) blocks leakage current from the detector from entering the preamplifier which lowers the noise. However, additional noise is introduced by the load resistor ( $R_L$ ) after the high voltage input filter which is chosen to be as large as possible to limit the voltage drop due to the detector leakage current. DC coupling is beneficial for detectors that have a very low leakage current (below  $10^{-14}$  A) because it eliminated the noise associated with the load resistor and minimizes the stray capacitance which can improve the signal to noise ratio (SNR) [59].

Furthermore, a current sensitive preamplifier, illustrated on the right side of Figure 4.3, does not have a feedback capacitor and the output voltage is related to the input current by  $v_{out}(t) = -i_{in}(t)R_f$  which allows for the shape of the induced current to be directly transferred to a voltage pulse at the output of the amplifier.

## 4.2 Characteristics of noise

Since the signal induced on the electrodes of a diamond detector is very small, any noise introduced into the system will greatly degrade the accuracy of the information extracted from the signal and impose higher requirements on further pulse processing. The most common types of noise found in a radiation detector system are:

- **Thermal (Johnson) Noise** – White noise caused by the random motion of free charge carriers in a resistive material. Increases with system bandwidth without limits.
- **Shot Noise** – White noise caused by charge carriers having a discrete amount of charge. This introduces random fluctuation of current around an average value. The leakage current is one source of this type of noise.
- **Flicker Noise (1/f noise)** – Frequency dependent noise resulting from the generation and recombination of charge carriers in a semiconductor due to impurities. This type of noise is also generated from the fluctuation in conductivity due to imperfect contact between two materials. The input transistor of the preamplifier generates 1/f noise.
- **Dielectric noise** – Frequency dependent noise which increases with frequency. Any fluctuation in the dielectric properties of a material caused by temperature, mechanical vibration, or age will introduce noise. This can be reduced by using dielectric materials with low losses, such as quartz, ceramics, Teflon, and polystyrene.

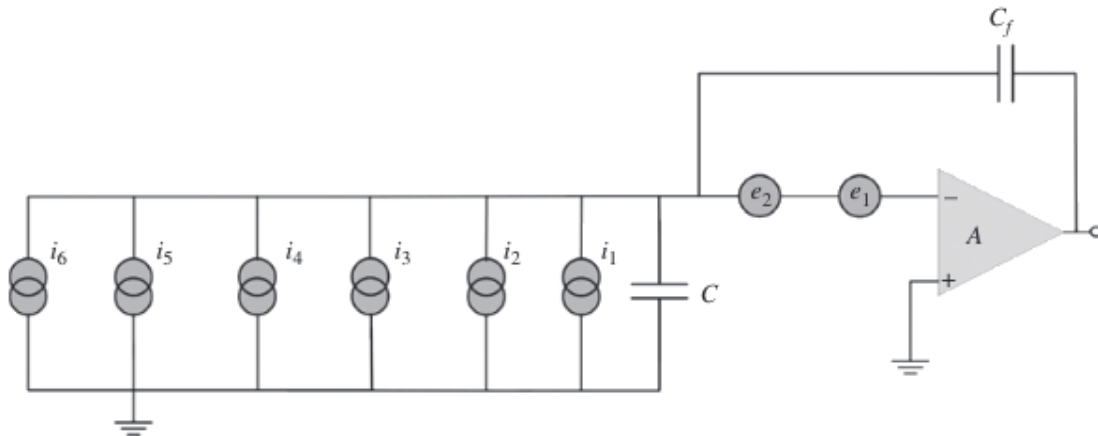


Figure 4.5 - Noise equivalent circuit of an AC coupled charge sensitive preamplifier [59].

Using the types of noise described above, an equivalent circuit of an AC couple preamplifier can be constructed as illustrated in Figure 4.5 where each component is replaced by a noise source connected in series or parallel. The two serial voltage noise sources ( $e_1$  and  $e_2$ ) represent the input transistor thermal and 1/f noise for which the voltage noise density can be written as [59]:

$$\frac{de_1^2}{df} = 4kTR = 4kT \frac{\gamma}{g_m} = 4kT \frac{0.7}{g_m} \quad (4.5)$$

$$\frac{de_2^2}{df} = \frac{A_f}{f} \quad (4.6)$$

where  $\gamma$  depends on the channel length of the FET and is usually 0.7,  $g_m$  refers to the transconductance of the amplifier, and  $A_f$  is a characteristic constant for the transistor. The parallel noise sources are summarized in Table 4.1.

Table 4.1 - Parallel noise sources.

	Description	Expression
$i_1$	Shot noise of the transistor gate leakage current	$\frac{di_1^2}{df} = 2qI_g \quad (4.7)$
$i_2$	Feedback resistor thermal noise	$\frac{di_2^2}{df} = \frac{4kT}{R_f} \quad (4.8)$
$i_3$	Bias resistor thermal noise	$\frac{di_3^2}{df} = \frac{4kT}{R_b} \quad (4.9)$
$i_4$	Induced transistor gate current noise	$\frac{di_4^2}{df} = S_{ws}\omega^2 C_{gs}^2 \delta \quad (4.10)$
$i_5$	Shot noise from the detector leakage current	$\frac{di_5^2}{df} = 2qI_L \quad (4.11)$
$i_6$	Dielectric noise	$\frac{di_6^2}{df} = 4kT(DC_D)\omega \quad (4.12)$

The total noise power density can be calculated by evaluating the above circuit with the presented noise sources, yielding the following expression:

$$\frac{dv_o^2}{df} = \left[ 4kT \frac{0.7}{g_m} + \frac{A_f}{f} \right] \frac{(C + C_f)^2}{C_f^2} + \left[ 2q(I_L + I_g) + 4kT \left( \frac{1}{R_f} + \frac{1}{R_b} \right) \right] \frac{1}{\omega^2 C_f^2} + \frac{4kT(DC_D)}{\omega C_f^2} \quad (4.13)$$

The above equation can be rewritten as:

$$\frac{dv_o^2}{df} = \frac{1}{C_f^2} \left[ aC_{tot}^2 + \left( A_f C_{tot}^2 + \frac{b_f}{2\pi} \right) \frac{1}{f} + \frac{b}{(2\pi)^2} \frac{1}{f^2} \right] \quad (4.14)$$

where the constant  $a$  is the series white noise,  $b$  is the dielectric noise and  $b_f$  the parallel white noise. A similar approach can be applied to a current sensitive preamplifier to derive an expression of the noise power density. The main difference between the two preamplifiers is the size of the feedback resistor and the presence of the feedback capacitor. Since the value of the feedback resistor has to be smaller for the current sensitive preamplifier, the level of noise is going to be higher due to the thermal noise [59]. An analytical analysis of the noise sources in a preamplifier, as well as all the parameters that affect them are described above. There is no ideal preamplifier that works in all situations and a compromise is made between the noise introduced by the preamplifier and its operating range, i.e. the maximum signal amplitude at the input and signal frequency. As will be discussed in section 6.4 of this work, three different preamplifiers have been tested with different first stage transistors, feedback resistors and coupling capacitors which vary the parameters described above in order to find the optimal configuration for processing signals from a diamond detector.

Noise can be also introduced into the system through interference (parasitic noise), the most common types being electromagnetic interference (EMI), grounding related interference and vibrations. EMI is the result of stray magnetic fields from surrounding equipment, such as power supplies, vacuum pumps, pressure gauges and computers. All electronic devices emit electromagnetic waves which can be picked up by the sensitive electronics at the input of the preamplifier. EMI falls off with the  $\frac{1}{r^2}$  rule (where  $r$  is the radius from the source) and therefore moving sources of EMI further away from the detector is the best solution. However, this is not



always possible and therefore it is good practice to enclose the detector in a Faraday cage. It is also important to ground the Faraday cage because parasitic capacitance between the circuit and shield can provide a feedback path from the output to the input. The electrodes on the diamond detector and the conductor to the input of the preamplifier act as a very sensitive antenna and any EMI present in the surrounding is induced and superimposed on the signal. As will be discussed in section 7.3 and can be observed from the signal frequency spectrum in Figure 7.11, higher frequency noise was successfully eliminated by selecting specific trigger criteria while the lower frequency noise could not be eliminated and required further digital filtering. Furthermore, ground-related interference results from ground loops. Ground loops are created when the ground connection between instruments is not at an equipotential resulting in a current to flow between the grounds of different instruments. Noise is also added to the system by vibration (Microphonic Noise), mechanical vibrations of the detector and preamplifier cause slight changes in the capacitance throughout the system leading to noise. This noise is usually observed in signals at multiples of the vibration frequency and therefore can be filtered out.

The noise added by the preamplifier and amplifier is expressed as equivalent noise charge (ENC). ENC is defined as the amount of charge required to be added to the input of a preamplifier that would change the output voltage by only the root mean square (RMS) value of noise. In other words, the amount of charge that yields a SNR of one [60]. The SNR is defined as the ratio of the mean pulse height to the RMS value of the noise. This can be calculated from the acquired experimental energy histogram using equation 4.15, where  $E_{fwhm}$  refers to the width of the acquired peak and  $E_{pair}$  is the energy required to generate e-h pairs in the specific material.

$$\frac{ENC}{Q} = \frac{V_{noise}}{V_{pulse}} = \frac{E_{fwhm}}{2.35 E_{pair}} \quad (4.15)$$

### 4.3 Digital signal processing of preamplifier signals

As described in the previous section, a charge sensitive amplifier integrates the current pulse induced on the electrode of the detector and therefore the amplitude of the pulse at the output of the preamplifier is proportional to the energy deposited by radiation in the detector. As will be discussed in more detail in section 5.3 and 7.3, the pulse shape from a detector is either of a triangular or square shape. When this signal passes through a charge sensitive preamplifier, the

signal is integrated, and this results in an exponentially decreasing pulse which a decay RC time constant set by the preamplifier. Furthermore, noise is superimposed on the signal and signal processing techniques must be applied to improve the SNR and increase the accuracy of the pulse height analysis (PHA).

Signal processing increases the SNR by attenuating components of the input signal that lie outside the frequency range of the signal of interest. Due to the nature of the signal produced by the preamplifier, there is always a compromise between noise minimization and signal alteration. Mathematically it is possible to compute the optimal filter by representing output signal from the preamplifier in the form  $s(t) = Ax(t) + n(t)$ , where A is the amplitude of the signal, x(t) is the waveform of the pulse and n(t) is the noise in the signal. The output of the filter can be calculated by convoluting the input signal with the impulse response function of the filter. Taking the Fourier transform of the input and filter impulse response ( $h(t)$ ), convolution becomes multiplication in Fourier space. The output of the filter can then be calculated by taking the inverse Fourier transform as follows [59]:

$$s(t) = Ax(t) + n(t) \quad (4.16)$$

$$S(\omega) = AX(\omega) + N(\omega) \quad (4.17)$$

$$v_o(t) = \frac{A}{2\pi} \int H(\omega)X(\omega)e^{j\omega t}d\omega \quad (4.18)$$

Similarly, the RMS noise at the output of the filter can be calculated with the noise power density of the filter  $N(\omega)$ :

$$v_n^2 = \frac{1}{2\pi} \int |H(\omega)|^2 N(\omega) d\omega \quad (4.19)$$

Therefore, the SNR ( $\eta$ ) is given by:

$$\eta = \frac{v_o^2}{v_n^2} = \frac{A^2 \int |H(\omega)|^2 |X(\omega)|^2 d\omega}{2\pi \int |H(\omega)|^2 N(\omega) d\omega} \quad (4.20)$$

As observed from equation 4.14 above, the noise at the output of a preamplifier can be expressed as a combination of white, pink, and brown noise, which depend on frequency as  $f$ ,  $1/f$  and  $1/f^2$  respectively. Initially only series (a) and parallel (b) white noises sources are assumed:

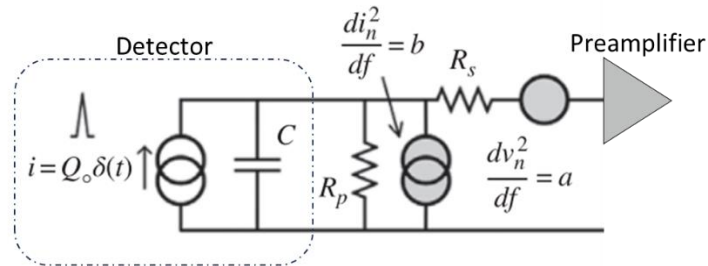


Figure 4.6 - Noise sources between the detector and the preamplifier [59].

$$N(\omega) = a + \frac{b}{C^2 \omega^2} \quad (4.21)$$

Or rewritten as:

$$N(\omega) = a \left( 1 + \frac{1}{\tau_c^2 \omega^2} \right) \quad (4.22)$$

The optimal filter can be calculated by maximizing equation 4.20. The details procedure for obtaining the solution for the optimal filter from the above relation can be found in literature and will not be outlined here [59]–[61]. The impulse response of an optimum filter for an exponentially decreasing function (as illustrated in the top graph of Figure 4.7) is characterized for the measurement time  $T$  by the following function:

$$h(t) = x(T - t) \quad (4.23)$$

which is the time inverted input signal delayed by the measurement time. The output of such a filter is:

$$v_o(t) = e^{-\frac{|t-T|}{\tau_c}} \quad (4.24)$$

where  $\tau_c$  is the corner time constant representing the inverse frequency at which the contribution of the serial (a) and parallel (b) noise are equal,  $\tau_c = C \sqrt{\frac{a}{b}}$ , while  $C$  is the total input parallel capacitance ( $C_d + C_i$ ). The optimum filter has a cusp shape with infinite length. The input and output of the optimum filter are illustrated in Figure 4.7.

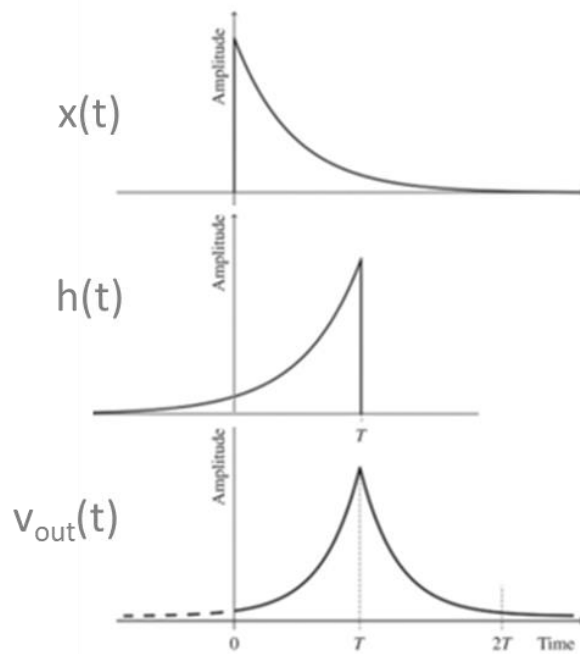


Figure 4.7 - The top graph shows the input signal (exponentially decaying signal from a preamplifier), the middle graph shows the impulse response of the filter, while the bottom graph shows the output of an optimum filter. [59].

The cusp filter described above is the theoretical optimal filter for radiation detector systems, however it is not practical and cannot be implemented. The sharp rise to maximum amplitude makes amplitude measurement difficult and makes it prone to ballistic effects. Furthermore, the slow signal return to baseline is prone to pile up effects due to the stochastic nature of radiation which further deteriorates the effectiveness of the filter at higher event frequencies. Since the cusp filter is the optimum filter in terms of signal to noise, it is useful as a comparison to other filters

which are more practical to implement. In this work we will consider only two practical filter types and their performance compared to the optimum infinite cusp filter are presented in Table 4.2 [15].

Table 4.2 - Comparison of filter performance to the optimum filter.

Filter	S/N ratio to optimum filter
Infinite Cusp	1
Triangular	0.930
CR-RC	0.736

As mentioned above, the SNR is improved by limiting the frequency response of the system, effectively creating a bandpass filter which attenuates frequencies that are below and above the signal frequency. The most commonly used practical filter for pulse processing is the CR-RC filter, consisting of a highpass filter in series with a lowpass filter as illustrated in Figure 4.8. The highpass section is labeled the differentiator and the lowpass section, the integrator since they differentiate and integrate the input pulse, respectively.

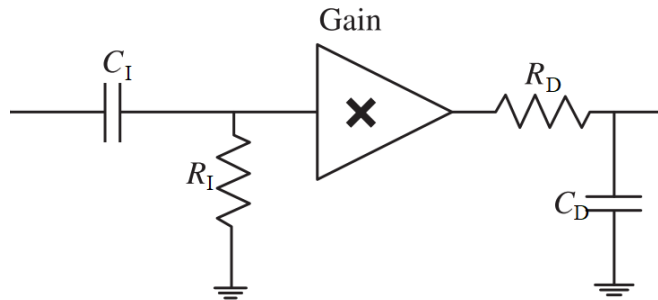


Figure 4.8 - CR-RC Filter.

Due to its simplicity, it is easy to implement and easy to analyze. The transfer function for each part of the filter can be easily derived to be:

$$H_I(s) = \frac{s\tau_I}{1 + s\tau_I}, \tau_I = R_I C_I \quad (4.25)$$

$$H_D(s) = \frac{1}{1 + s\tau_D}, \tau_D = R_D C_D \quad (4.26)$$

$$H(s) = H_I(s) \cdot H_D(s) = \frac{s\tau_I}{(1 + s\tau_I)(1 + s\tau_D)} \quad (4.27)$$

For a unit step input, the output in the time domain is then:

$$v_o(t) = \frac{\tau_D}{\tau_D - \tau_I} \left( e^{-\frac{t}{\tau_D}} - e^{-\frac{t}{\tau_I}} \right) \quad (4.28)$$

The best SNR for this type of filter is achieved when the integrator and differentiator time constants are equal,  $\tau_I = \tau_D = \tau$  [60], therefore the transfer function and output become:

$$H(s) = \frac{s\tau}{(1 + s\tau)^2} \quad (4.29)$$

$$v_o(t) = \frac{t}{\tau} e^{-\frac{t}{\tau}} \quad (4.30)$$

The maximum amplitude with such a filter is achieved at  $t = \tau$ , however the filter introduces a long tail which takes many time constants to return to baselevel. This makes the filter susceptible to pileup events which limit the measurement rate of the system, as will be at the end of this section.

From Table 4.2, it can be seen that the simple CR-RC filter has a 26 % worse SNR than the optimal cusp filter. Better performance can be achieved by a triangular filter which has become the standard filter implemented for radiation detector digital signal processing (DSP). Practically, a trapezoidal filter is used instead of a triangular filter to mitigate ballistic effects which will be discussed later. A trapezoidal filter is essentially a triangular filter where the maximum amplitude is held for a specific time. The transfer function of a trapezoidal filter can be synthesized by examining the input and required output functions. The input is, as discussed above, an exponentially decaying signal with a time constant ( $\tau$ ) and amplitude ( $E$ ).

$$f_{IN}(t) = E e^{-\frac{t}{\tau}} \Rightarrow F_{IN}(z) = E \frac{z}{z - \beta} = E \frac{1}{1 - \beta z^{-1}}, \beta = e^{-\frac{T}{\tau}} \quad (4.31)$$

$\beta$  is known as a pole-zero cancellation coefficient which is depended on the sampling period of the digitizer (T). The output function can be synthesized by examining the trapezoidal shape illustrated in Figure 4.9 [62], [63].

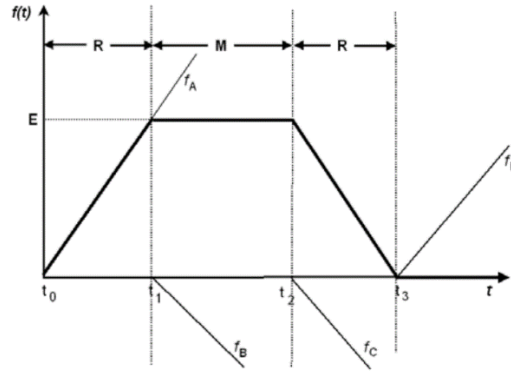


Figure 4.9 - Synthesizing a trapezoidal function.

$$f_{OUT}(t) = f_A(t) + f_B(t) + f_C(t) + f_D(t) \quad (4.32)$$

$$F_{OUT}(z) = \frac{E}{R} (1 - z^{-R})(1 - z^{-(R+M)}) \frac{z^{-1}}{(1 - z^{-1})^2} \quad (4.33)$$

Combining equations 4.31 and 4.33, to get the transfer function of the filter:

$$H_{TRZ}(z) = (1 - z^{-R})(1 - z^{-(R+M)}) \frac{(1 - \beta z^{-1})}{1 - z^{-1}} \frac{z^{-1}}{1 - z^{-1}} \frac{1}{R} \quad (4.34)$$

where the parameters R and M represent the represent the trapezoid rise/fall and flat top time, respectively. The transfer function presented above is a combination of a Finite impulse response (FIR) and infinite impulse response (IIR) filter which can be implemented in a DSP system [64]. Jordanov et al. [63] presented an implementation of such filter as a three units as illustrated in Figure 4.10. This implementation consists of two delay-subtract units followed by a highpass deconvolver unit (digital zero-pole compensator) where the parameters k and l determine the duration of the rising and falling edges of the filter, while the m parameter is used to compensate for zero/poles present in the system.

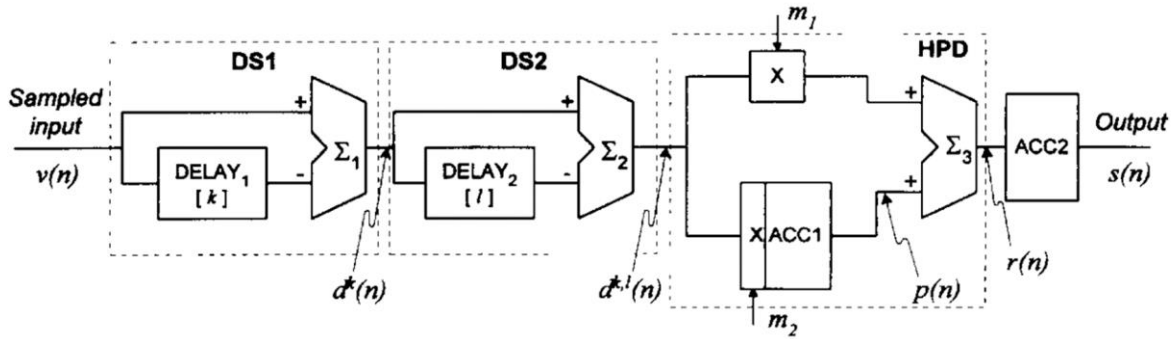


Figure 4.10 - Implementation of a trapezoidal filter in a DSP system [63].

This filter was implanted in a Virtex 6 FPGA along with other components required for data extraction, storage and communication with a computer over the ethernet protocol [65]. The main components of the filter, presented in Figure 4.11, were programmed and simulated using the MATLAB Simulink toolbox (MathWorks, 2017) and synthesized into VHDL using the Xilinx System Generator for DSP design tool (Xilinx, 2017) [64].

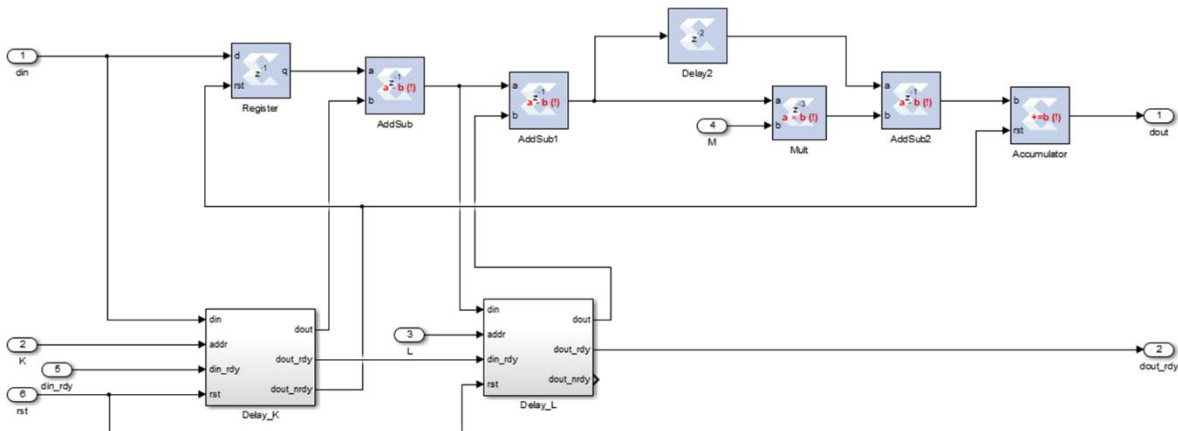


Figure 4.11 - FPGA implementation of trapezoidal filter.

Figure 4.12 presents the top-level implementation of the multiparameter acquisition system which contains this filter at its core (located in block labeled 2 in the figure). However other signal processing components are also required for the acquisition system to trigger on the proper event and extract the relevant data. The main components of the implemented acquisition system are: 1. signal delay block, 2. trapezoidal filter, 3. fast filter, 4. noise estimator, 5. baseline restorer, and 6. pileup rejector. The signal from the ADC is first fed into a fast filter (3) with the same trapezoidal design but with a very short shaping time to recognize the pulse and record a time stamp. If the acquisition process is triggered by the fast filter, the higher resolution but slower trapezoidal filter



(2) processes a copy of the original signal supplied by the delay block (1). Furthermore, for accurate triggering on real pulses, the acquisition system estimates the noise in the original signal with block 4. While blocks 5 and 6 adjust the trapezoidal filter output for more accurate amplitude reading.

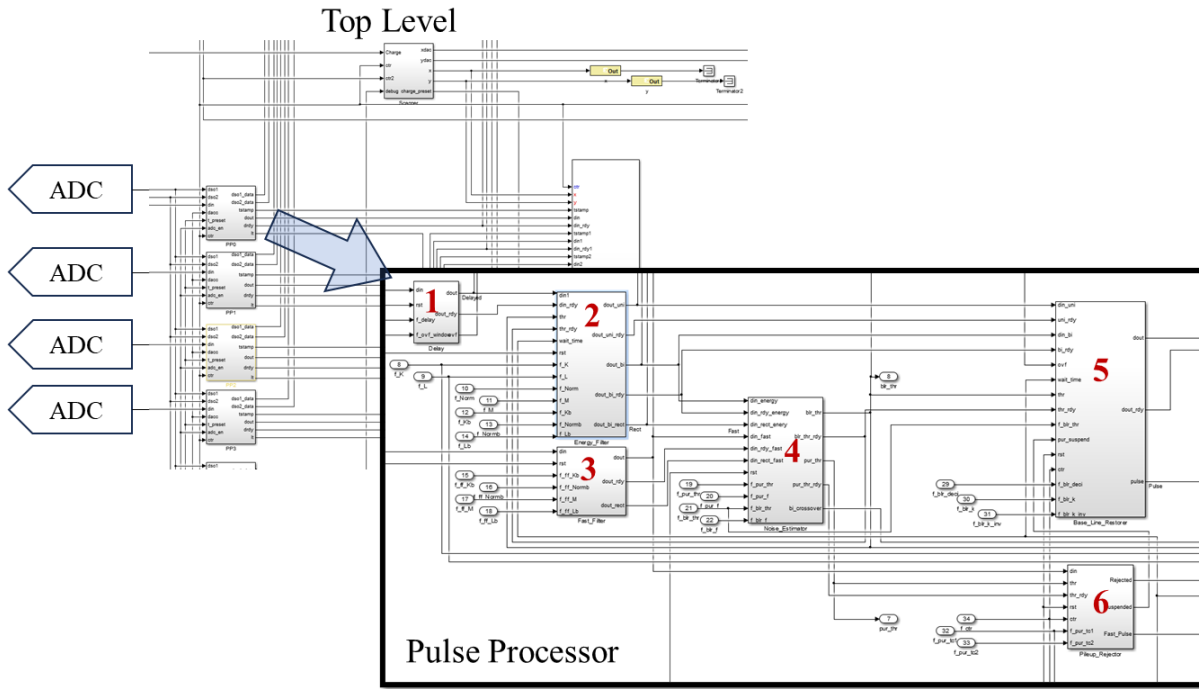


Figure 4.12 - Top level of multiparameter FPGA acquisition system implementation with the pulse processor subsystem expanded in the inlay. The pulse processor consists of a 1. Delay block, 2. Trapezoidal filter, 3. Fast filter, 4. Noise estimator, 5. Baseline restorer, and 6. Pileup rejector.

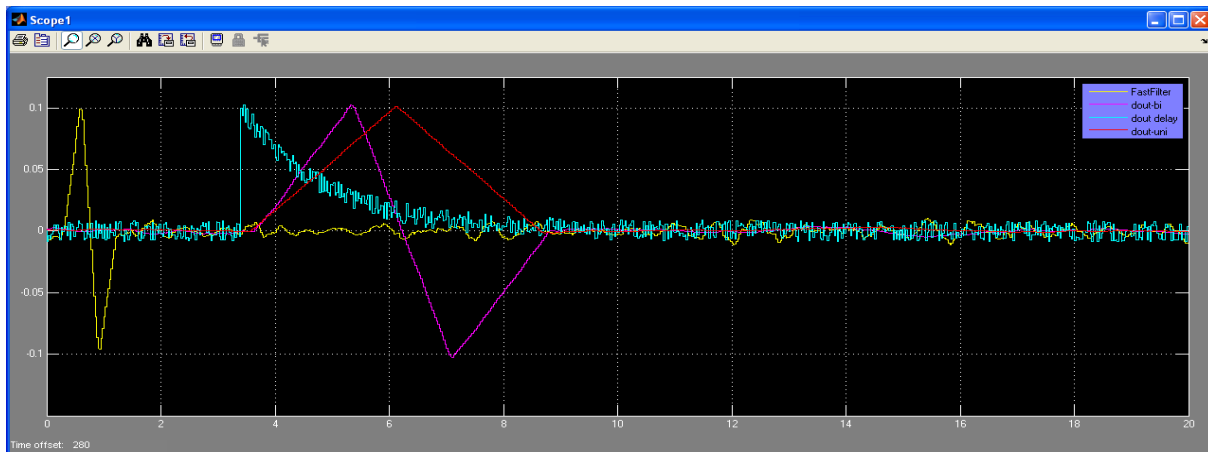


Figure 4.13 - Simulation of a preamplifier pulse processed by the acquisition system algorithm. The delayed preamplifier pulse (blue) is shaped into a trapezoidal unipolar (red) and bipolar (purple) pulse. The output of the fast filter is displayed in yellow.

This process can be observed visually in Figure 4.13. In this figure the original signal from the ADC is processed by the fast filter (yellow) which triggers the trapezoidal filter to process a delayed copy of the signal (blue) which outputs a unipolar (red) and bipolar (purple) signal after correcting the baseline. The maximum amplitude of the unipolar (red) pulse is recorded along with the timestamp and coordinates of the scanner position into memory which is then read by the acquisition software running on a computer. The acquisition software generates a histogram and 2D map with this collected data.

As mentioned above, in real systems, factors such as ballistic deficit, pileup and baseline shifts must be considered when designing filters. These effects will now be explained in more detail. Ballistic deficit refers to the dependence of the pulse height after processing on the rise time of the input signal. Therefore, fluctuations in the charge carrier collection time in the detector can cause variations in the signal amplitude after signal processing. CR-RC filters are more susceptible to this effect than trapezoidal filters because the max amplitude of the signal is held for a longer time in trapezoidal filters. By increasing the time constant of a CR-RC filter or increasing the “flat top” of the trapezoidal filter, this effect can be minimized but at the expense of increasing the probability of pileup. This parameter is optimized experimentally based on the measurement conditions. The amount of current provided by the accelerators varies depending on the ion that is accelerated, the energy of the ion and which experimental beam line is used as each chamber has its specific electromagnetic optics which influence the total current delivered to the target. To optimize the flat top or time constant parameter, the amount of pileup in the spectra as well as the resolution of the individual peaks is observed. Increasing the flat top will increase the amount of pileup and increase the resolution to a point. The optimal flat top parameter balances the resolution and the amount of pileup present in the spectrum. Pileup occurs when two signals are close to each other in time causing their pulses to overlap, as illustrated in Figure 4.14b and Figure 4.14c. The second pulse is then superimposed on top of the first pulse because the first signal has not returned to the baseline value before the second signal arrived, causing an incorrect height reading. The larger the shaping time, the higher the probability of pileup. The same problem occurs if the baseline, the reference point from which signal amplitudes are measured, is not stable. Fluctuations in the baseline value leads to fluctuations in the measurement of the pulse height which degrades the energy resolution of the system. Baseline fluctuations can occur due to high pulse rates, detector leakage current in dc couple systems, uncorrected pole-zero, or thermal drifts in electronic components.

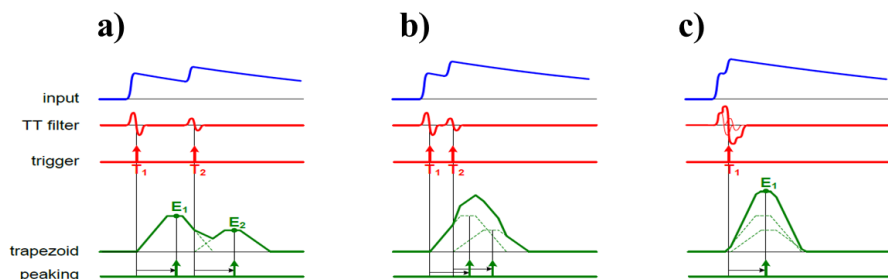


Figure 4.14 - Pileup occurs when two pulses are close in time and are recognized as a single event by the acquisition system. a) Two pulses are accurately recognized b) Overlapped pulses recognized as a single pulse c) Complete overlap of the pulses recognized as one [58].

#### 4.4 Ion beam analysis

The versatility of electrostatic accelerators which can accelerate a variety of ion species from simple ions like hydrogen and helium, to very heavy ions such as gold and lead, using a wide range of acceleration voltages (e.g. from 0.1 MV up to 5 MV at RBI) made them a ideal tool for various applications. These applications can be grouped into those that are using the ion beams to characterize materials exposed to ion beams, or to modify their properties by ion beam irradiation or implantation. Figure 4.15 illustrates the main characterization techniques used along with the type of radiation there are based on.

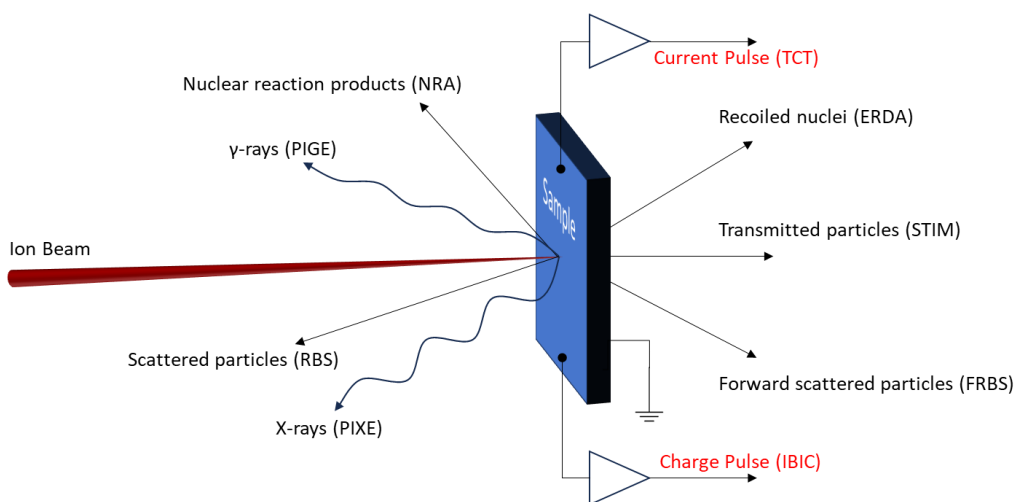


Figure 4.15 - Ion Beam Analysis (IBA) techniques.

For the purpose of this work, we will focus on two techniques (highlighted in red in Figure 4.15), Ion Beam Induced Charge (IBIC) [66] and the Transit Current Technique (TCT) [67]. IBIC spectroscopy is a widespread tool used for the characterization of charge transport in

semiconductor materials. It utilizes an ion beam on very low current ( $< \text{fA}$ ) from an accelerator to induce charge carriers along the ion path in a detector volume [66]. The performance of the detector can be evaluated by measuring the amount of induced charge acquired by the detector. For this technique a charge sensitive amplifier is used with pulse processing to extract the pulse height which is proportional to the induced current on the detector electrodes. By collecting the height of each pulse over time, a histogram can be created representing a spectrum of collected charge by the detector as a function of energy. For a mono energetic beam on a detector with 100 % CCE, the pulse height should be always the same resulting in a single peak in the histogram at the specific beam energy. However, due to the presence of noise in the signal, the peak will be broadened. The width of the peak can be measured by its full width at half maximum (FWHM) and it represents the contribution of the noise in the detector and signal processing chain. If the CCE of the detector is not 100 %, the peak will shift to lower energies. Additionally, the ion beam can be scanned over the surface of the detector providing 2D information about the efficiency of the detector. By plotting the histogram peak position (energy) for every beam position, a map can be generated of the detector efficiency as illustrated in Figure 4.16. It can be observed from Figure 4.16 that the detector efficiency is lower at the edges of the electrode and damaged regions of the detector. Furthermore, TCT utilizes a current sensitive broadband preamplifier and information about charge transport in the diamond detector can be evaluated by the shape, rise, and fall times of the current pulses [12]. Figure 3.1 illustrates an example of a TCT pulse on an oscilloscope with the significance of each portion of the pulse outlined. This method is useful because it can provide information on which charge carrier was generated, how many charge carriers were generated and where. This information can be used by a digital system to discriminate between different types of radiation, specifically between gamma and neutrons in the context of this work. However, due to the use of a broadband preamplifier and no signal processing techniques to increase the SNR, noise minimalization is essential for TCT.

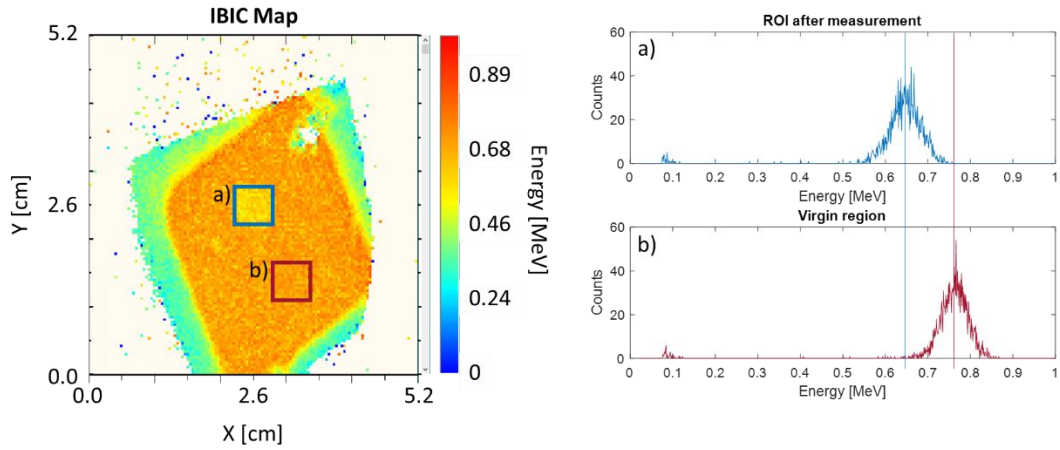


Figure 4.16 - Imaging of a diamond detector using the IBIC method. The image on the left illustrates the measured energy by the detector across its surface. The plots (a,b) show the acquired IBIC spectrum from ROI a) and b). The region a) has lower charge collection efficiency than region b) due to polarization as discussed in section 3.3.

## 5 NEUTRON DISCRIMINATION

Over the years many neutron detectors have been developed [68] and none of them are exclusively sensitive only to neutron, but detect other forms of radiation as well. To isolate only the neutron portion of the signals from these detectors, discrimination techniques must be applied. Many techniques have been employed to discriminate neutrons from other forms of radiation both in the digitally and in the analog domain [69]. As will be discussed in this section, the main discrimination strategies are either based on detection of associate particles from nuclear reactions (see section 2.3), coincidence measurements or through the analysis of the pulse shape from the detector. Some of these methods have been already applied to diamond detectors and they will be investigated here in sections 5.2, 5.3 and 5.4. It should be noted that all these methods have only been demonstrated previously at room temperature with diamond detectors. For the purpose of this work, it was chosen to focus primarily on one type of discrimination method, that is pulse shape discrimination (PSD) and apply it to a diamond detector operating at cryogenic temperatures. PSD was chosen due to the design restriction imposed on  $\mu$ LoMs and the specific environment where they will operate. Furthermore, PSD has the additional benefit of being able to work in conjunction with other discrimination methods and further enhance them.

### 5.1 Neutron induced spectra in diamond detectors

As mentioned in section 2.3, diamonds are used to detect neutrons indirectly through nuclear reactions which produce ionizing particles. For fast neutrons, the associated reactions are listed in Table 2.1 which produce ionizing particles throughout the detection volume of the diamond detector. These secondary particles create electron hole pairs as they interact with the diamond which drift and induce current in the detector electrodes. The expected spectra are illustrated in Figure 5.1 [70]. The figure on the left shows the spectrum obtained by 20.5 MeV and 8.3 MeV neutrons in black and blue, respectively. Due to the kinematics of the reaction and differences in the amount of energy transferred to the secondary particles, the spectrum shifts with incident neutron energies. The figure on the right of Figure 5.1 shows more spectra for neutron energies from 7.33 MeV to 20.5 MeV. Spectra under 7.33 MeV are not shown since the threshold for nuclear reactions is at 6.2 MeV. Below this threshold, no nuclear reactions take place, and the spectrum is composed only of system noise, gamma, x-ray radiation, and signals generated by neutron recoils with carbon atoms. This creates a “background” spectrum at lower energies whereby analyzing

only the height of the signal pulses from the detector, it is impossible to distinguish the source of radiation.

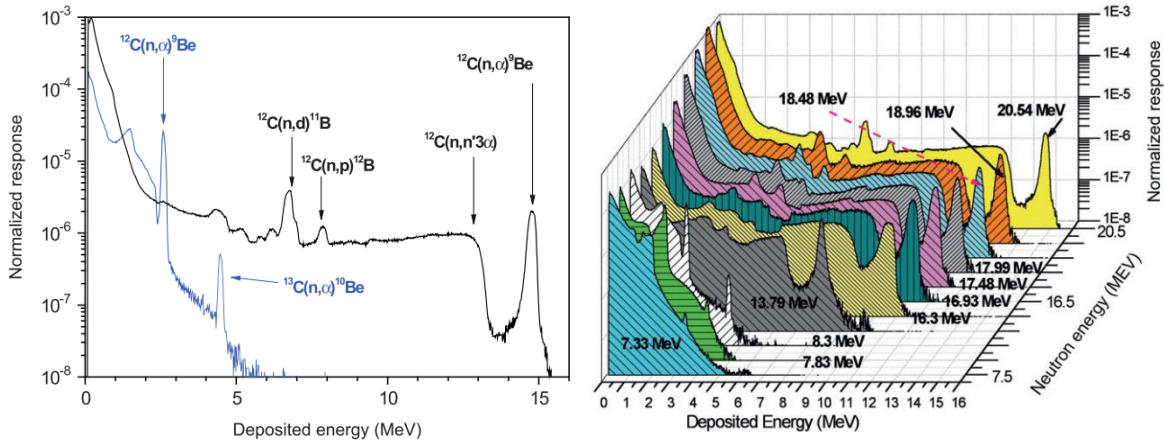


Figure 5.1 - Spectra for Neutrons of 7 to 20 MeV [70].

For neutron energies below the threshold energy for nuclear reactions, only elastic scattering occurs between the neutron and carbon atoms. In this process the carbon atom is recoiled, and this recoil is a movement of charge which also induces current on the detector electrodes. As mentioned in section 2.3, the maximum recoil energy can be calculated, and the spectrum will consist of a continuum of events up to this maximum recoil energy as illustrated in Figure 5.2 [26].

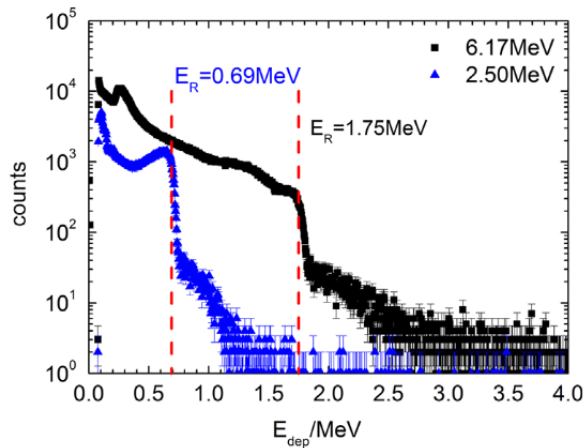


Figure 5.2 - Spectrum of fast neutrons below 6.2 MeV [26].

If the neutron flux has to be determined, it can be estimated from the  $^{12}\text{C}(n,\alpha)^9\text{Be}$  peak created from the nuclear reaction by neutrons of energies greater than 6.2 MeV. However, as can be observed from the lower energy spectra from Figure 5.1 and Figure 5.2, there is no distinctive peak that can be used to estimate the neutron flux for neutrons under 6.2 MeV. All features in the spectrum are a superposition of many processes which cannot be easily isolated. For these lower neutron energies, as mentioned in section 2.3, elements that have a higher probability of undergoing nuclear reactions can be placed on top of the detector to act as a “converter” layer to transform the neutrons to ionizing particles which can be detected by the diamond detector. Figure 5.3 illustrates spectra obtained by a diamond detector with a  $^6\text{LiF}$  converter of various thicknesses [18]. The  $^6\text{Li}(n,\alpha)\text{T}$  reaction takes place inside the film and the diamond detects the  $\alpha$  and T emitted from the film. This produces two peaks which are distinguishable and can be used to estimate the neutron rate. The figure also shows the impact of converter layer thickness on the spectrum. The thicker the converter layer, the more material which attenuates the  $\alpha$  and T particles before they reach the diamond detector. This straggling in the converter causes broadening of the peaks in the spectrum. However, the probability of neutron interaction with the converter increases with the thickness leading to a tradeoff between detection efficiency and resolution.

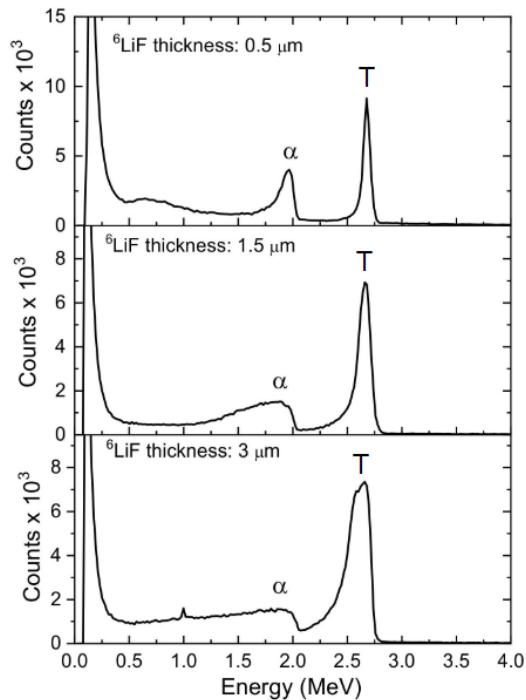


Figure 5.3 - Spectra for neutrons with  $^6\text{LiF}$  converter layer of various thicknesses.



## 5.2 Discrimination through detector configurations

The use of a converter layer is one of the possible ways to enable discrimination of neutrons as was discussed in the previous section. This concept can be taken a step further by sandwiching the converter between two diamond detectors. The single detector configuration is illustrated on the left of Figure 5.4, while the sandwich on the right [71].

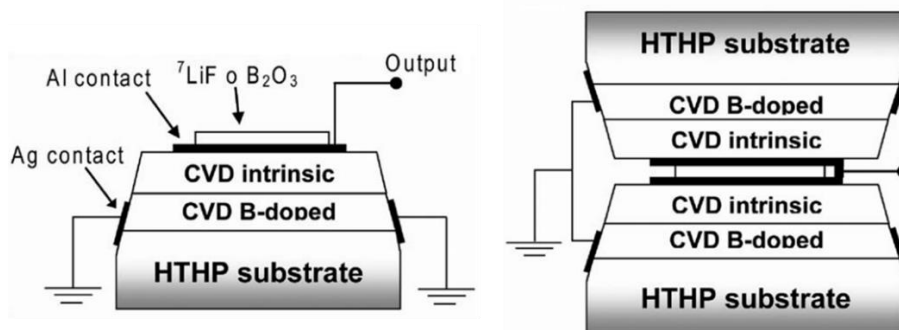


Figure 5.4 - Single and Sandwich Detector Configurations.

The single detector (right of Figure 5.4) operates as described in the previous section where the neutron undergoes a nuclear reaction in the converter layer ( ${}^6\text{LiF}$  or  ${}^{10}\text{B}_2\text{O}_3$ ) and the biproducts are detected in the diamond. In the above figure, the intrinsic diamond detector is built upon a boron doped diamond layer for contact purposes and has not been detached from the High Temperature High Pressure (HTHP) substrate from which the CVD diamond was grown, which acts as an insulator. It should also be noted that since the nuclear cross section of the converter layer (see Figure 2.3) drops exponentially for fast neutrons ( $E > 1$  MeV), the detector can simultaneously detect slow and fast neutrons. The sandwich configuration, on the other hand, is just a combination of two diamond detectors that share a common convert layer. This configuration increases the detection volume which makes it more efficient at detecting neutrons and allows for all products from the nuclear reaction in the converter layer to be collected (due to energy conservation, the products of the nuclear reaction are emitted at  $180^\circ$  to each other). Furthermore, if the two detectors in the sandwich configuration are read out independently, coincidence measurements can be made to discriminate neutrons [18], [23]–[25], [71]–[74]. Discrimination based on coincidence measurements will be discussed in more detail later in this section.

Neutron discrimination can also be achieved by specifically designing the electrodes on the diamond detector. Alpha particles released from the converter and diamond interactions with neutrons transverse only a few micrometers in diamond. Therefore, all created charge carriers are localized to a small region of a diamond as illustrated in Figure 3.1. Gamma radiation, on the other hand, interacts weakly with diamond and pass through the whole volume of the detector without losing too much energy and create charge carriers throughout the volume of the detector as illustrated on the right of Figure 3.3. By designing electrodes that can provide spatial information, ion interaction can be discriminated from photon interaction. However, the design on the electrodes also influences the detector capacitance which, as was discussed in the previous section, influences the SNR and can limit the system bandwidth.

### 5.3 Discrimination based on Pulse Shape Analysis

As mentioned above, ions and photons produce different ionization profiles since they interact with the diamond through different mechanisms. Photons produce charge carriers throughout the volume of the detector. These charge carriers start drifting to their respective electrodes at approximately the same time leading to an initial large induced current at the electrode which decreases linearly with time. As the charge reaches the electrode, they stop moving and therefore stop inducing current in the electrode. The charge that was generated closer to the electrode stops first, while the charge generated at the other end of the diamond must drift through the entire volume of the detector. Since the externally applied electric field is constant and the drift velocity of the charge carriers is constant, this leads to a triangular induced current profile as illustrated in Figure 5.5a [75].

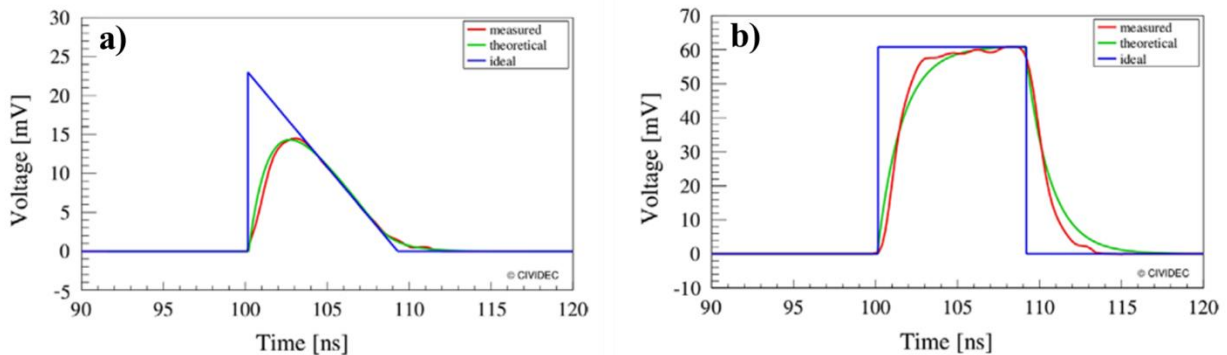


Figure 5.5 - Pulses generated by a)  $\gamma$ -ray and b) Alpha Particles [75].

Ions, such as the alpha particles emitted from nuclear reactions with neutrons do not have enough energy to pass through the whole volume of the detector and they transfer all their energy to the diamond in a few micrometers. Since most of the generated electron hole pairs are concentrated at one location, the induced current profile follows more of a rectangular shape as illustrated in Figure 3.1 and in Figure 5.5b. Using the TCT method, the general induced current profile can be detected with slight deviations from the theoretical shape due to the RC time constant of the system.

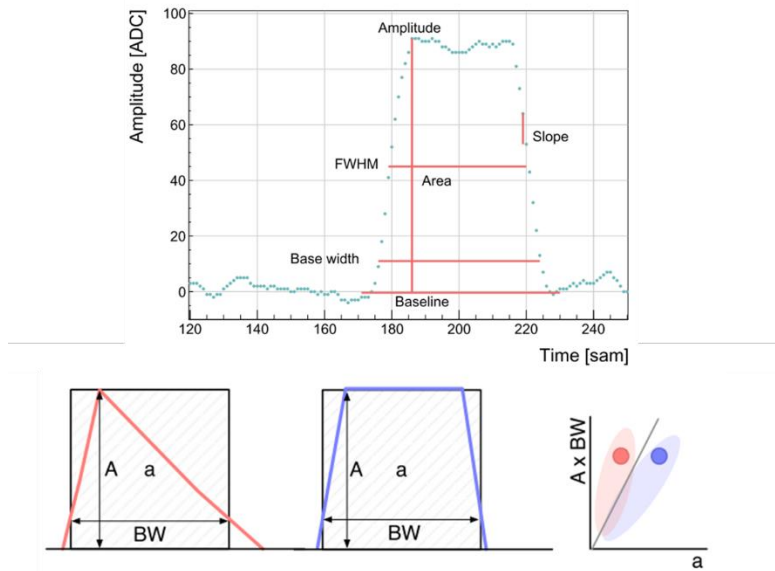


Figure 5.6 - Pulse shape discrimination parameters.

Algorithms have been developed to analyze the base width, amplitude, area and slope of each pulse and discriminate neutrons from gamma radiation based on two or more of these parameters as show in Figure 5.6 [40], [75]. However, TCT signals are obtained with a broadband amplifier without any further pulse processing to improve the SNR and this method is very sensitive to noise which can dramatically alter the shape of the pulse. Furthermore, fast neutrons can generate secondary ionization particles anywhere in the volume of the diamond detector which will also influence the induced current profile. As can be observed from the 3D plot of Figure 5.7, the induced current profile varies as a function of where the alpha particle is created in the diamond volume. Only near the electrode and in the ballistic center of the diamond detector will the induced current pulse be completely rectangular. At all other positions, the current profile will have a large

initial peak and then a rectangular pulse as illustrated on the right of Figure 5.7 [75]. More advanced signal processing techniques, that will be discussed in more details in section 7.5, such as signal first derivative counting, frequency domain analysis, wavelet power spectrum discrimination have also been applied to TCT signals for the purpose of PSD [76]. These techniques have been applied to discriminate neutrons from photons with a diamond detector, however only at room temperature. As discussed earlier in section 3.5, the CCE of a diamond detector drops significantly at low temperatures resulting in the TCT pulse amplitude to be 20 % of the room temperature value. This significantly degrades the SNR and makes discrimination based on current pulse shape very difficult.

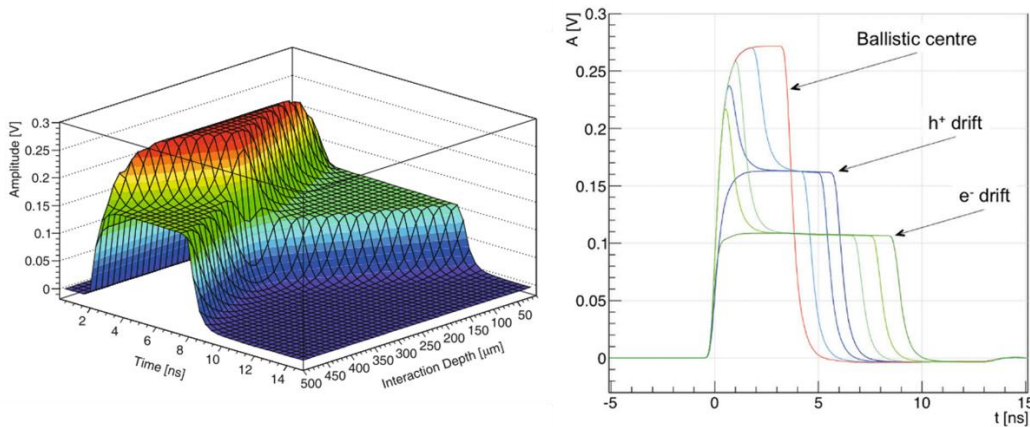


Figure 5.7 - Alpha particle current profile vs generation depth in a diamond detector [75].

Pulse shape discrimination can also be performed using a charge sensitive preamplifier since the different induced current profiles will influence the rise and fall time of the integrated current pulse. Although a lot of signal information is lost due to the bandwidth limits of the charge sensitive preamplifier, discrimination will still be possible utilizing the zero-crossing method. If the zero-pole correction is not applied to the output of a charge sensitive preamplifier or a bipolar shaper is used, the resulting signal will cross the baseline voltage level. Different rise and fall times will result in this zero-crossing point to occur at different times relative to the rising edge of the pulse. Discrimination can be performed by comparing the time between the leading edge of the signal and the zero-crossing point for various signals.

Such methods are widely applied to neutron-gamma discrimination in scintillator-based detector systems. As with diamond detectors, particles and photons are detected through different

mechanisms which produce different pulse shapes at the output of the detector. In scintillator-based detectors, the length of the signal pulse is much larger resulting in an observable difference in the output of a charge integrating preamplifier as illustrated in Figure 5.8.

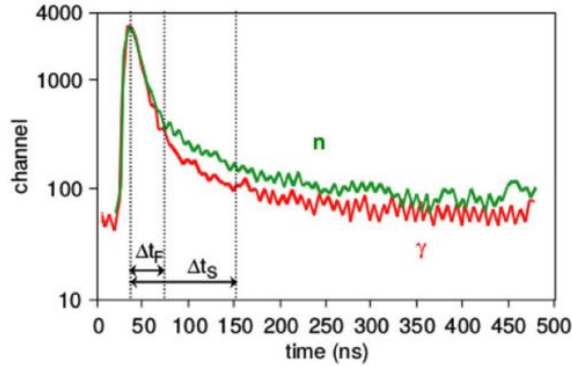


Figure 5.8 - Output signals of neutron and gamma radiation from a scintillator detector coupled to a charge sensitive preamplifier [77].

Signals presented in Figure 5.8 are successfully discriminated by comparing the integral of the signals over two intervals. This method is one of the few discrimination techniques which were implemented to run on FPGAs in real time [78]–[80]. Another method which was also implemented to run in real time is based on measuring the similarity of two vectors by calculating the cosine of the angle between them. Mathematically this is expressed as:

$$\cos \theta = \frac{x \cdot y}{|x||y|} = \frac{\sum_i^p x_i y_i}{\sqrt{\sum_i^p x_i^2} \sqrt{\sum_i^p y_i^2}} \quad (5.1)$$

where the input pulse  $x$  is compared to a template pulse  $y$  over  $p$  number of points and discrimination can be performed based on the cosine of the angle between the two pulses. This method can be further simplified replacing the template function with a unit step function and only comparing a portion of the signal, such as the rising edge of the signal. In this case the equation simplifies to [81]:

$$\cos \theta = \frac{\sum_i^p x_i}{\sqrt{p} \sqrt{\sum_i^p x_i^2}} \quad (5.2)$$

The above presented methods are easier to implement and provide pulse shape discrimination for signals from a scintillator detector, however these methods are not 100 % efficient and the discrimination criteria has to be set manually. Due to these shortfalls, these methods are not reliable enough for radiation rate measurements in applications such as machine control and safety. In recent years, more advanced techniques utilizing machine learning and artificial neural networks are being applied to pulse shape discrimination to develop a more robust and reliable system and very high discrimination efficiencies have been achieved with these techniques [77], [82]–[84]. However these techniques require a vast dataset of reliable data for training purposes, which is not available for diamond detectors at low temperatures.

Furthermore, the same problem of neutron gamma discrimination also exists in  $^3\text{He}$  neutron detectors. Advanced discrimination techniques such as Linear Discriminant Analysis and Multivariate Analysis were successfully applied both offline and in real time to signals from this type of detector to separate neutrons from gamma events [85].

#### 5.4 Discrimination based on event coincidences

As mentioned above in section 5.2, a detector layout can be chosen to allow for discrimination based on the coincidence of two signals in time. One example of this is with the sandwich detector layout where signals from one detector are compared to signals from the other and expected neutron reactions are discriminated by setting a coincidence time window.

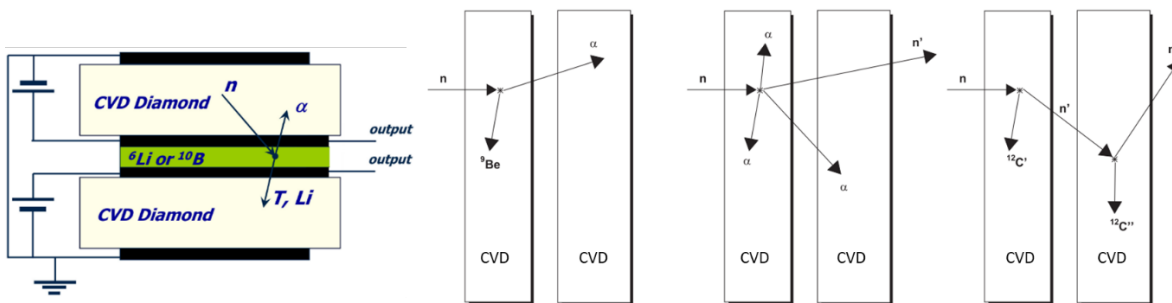


Figure 5.9 - Coincidence discrimination based on nuclear reaction products.

Figure 5.9 illustrated a sandwich detector with possible strategies for detecting only neutrons. The figure on the left shows the reactions  $^6\text{Li}(n,\alpha)^3\text{H}$  and  $^{10}\text{B}(n,\alpha)^7\text{Li}$  for slow neutrons. Neutrons can be discriminated by only accepting events where both products of the reaction are detected. If

the output of the top and bottom CVD diamond detectors are combined, the energy from both reaction products will be detected resulting in a peak in the spectrum at higher energy, allowing for discrimination based on energy as well [18]. The figure on the right of Figure 5.9 illustrates possible reaction for fast neutrons, specifically  $^{12}\text{C}(n,\alpha)^9\text{Be}$ ,  $^{12}\text{C}(n,n')3\alpha$  and  $^{12}\text{C}(n,n')^{12}\text{C}^*$  reaction where \* denotes an excited state. Neutrons can be discriminated by looking for events where only the specific coincidence of signals occur [74].

### 5.5 Summary of discrimination techniques

Chapter 5 focused on discrimination techniques found in literature which could be applied to the signal generated by a diamond detector. Many of these techniques have been applied to diamond detectors, however techniques which were applied to other types of detectors were also presented. The following table presents a broader overview of discrimination techniques found in literature with the reasons why some were applied in this work while others were not.

Table 5.1 - Summary of neutron/ $\gamma$ -ray discrimination methods from literature.

Discrimination Technique	Description	Used with detector type	Applicable to this work
Voltage Threshold (Charge Integration)	Setting a limit to the amount of charge expected to be deposited in the detector by each type of radiation.	Scintillators [15], Semiconductors [32], [86]	Not applicable to this work since the deposited charge by neutron and $\gamma$ -ray can be the same.
Pulse rise/fall time analysis	Different radiation types interact with matter differently resulting in differences at the beginning and end of the pulse.	Scintillators [15]	Not applicable to this work as neutrons can generate a variety of rise/fall times depending on their point of interaction inside the detector (see sections 3.1 and 5.3).
Zero-Crossing	Taking the second derivative of the pulse and discriminating based on when the base-line crossover occurs for	Scintillators [87]	Not applicable to this work since signals from a diamond detector do not have a specific second derivative zero

	each type of radiation.		crossing based on the type of radiation.
FWHM	Discrimination based on the triangle vs square pulse shaped of $\gamma$ -rays and neutrons, respectively.	Semiconductors [75], [76]	Applicable to this work
1st Derivative Peak Counting	Neutron signals will contain multiple sharp changes in amplitude while $\gamma$ -rays produce one sharp change followed by gradual return to baseline. Counting these events can identify the type of radiation detected.	Semiconductors [76]	Applicable to this work
Frequency Domain Analysis	Discrimination by examining the different frequency components present in each signal.	Scintillators [88], Semiconductors [76]	Applicable to this work
Wavelet Power Spectrum Analysis	Similar to Frequency Domain Analysis with the addition of showing frequency changes in the signal over time.	Scintillators [88], Semiconductors [76]	Applicable to this work
Pulse Gradient Analysis Frequency Gradient Analysis	Based on the different in the zero-order frequency (DC component) for neutron and $\gamma$ -ray signals.	Scintillators [89]	Not applicable to this work since neutron and $\gamma$ -rays do not produce the same difference in signal shapes with a diamond detector.
Cosine Similarity	Fitting acquired pulses to models using the Cosine formula as described in section 5.3	Scintillators [81]	Applicable to this work due to its simplicity and flexibility to not only compare signals to models but to reference signals as well.



Least Square Similarity	Fitting acquired pulses to models using the Levenberg-Marquardt nonlinear least squares algorithm and evaluating the quality of the fit.	Scintillators [90]	Applicable for this work, however it was chosen to focus on the Cosine Similarity algorithm instead due to a less resource intensive implementation for a real time system.
Time of Flight	Discrimination based on the different relative speeds of neutrons and $\gamma$ -rays.	Scintillators [91], Gas Detectors [92]	Not applicable to this work since only one detector is used.
Time over Threshold	Measuring the time a signal is over a certain amplitude value.	Scintillators [93], Semiconductors [60]	Not applicable to this work as both neutron and $\gamma$ -ray signals can have similar times over a given threshold dependent on the energy of the radiation.
Sandwich Detectors	Using multiple detectors in coincidence to detect nuclear reaction products.	Scintillators [91], Semiconductors [18]	Not applicable to this work since only one detector is used.
Machine Learning	Using neural network, random forest or principal component analysis algorithms to help group pulse shape features which can be used to discriminate between neutrons and $\gamma$ -rays.	Scintillators [69], Semiconductors [84], Gas Detectors [85]	Not applicable to this work since machine learning algorithms require a vast dataset for training which is not available.

## 6 EXPERIMENTAL SETUP

Up to this point the theoretical background of signal creation and processing in diamond-based radiation detectors has been presented, along with the complications arising when operating such a detector at cryogenic temperatures. From the literature review, it was found that in certain cases (alpha particle detection) the performance of a diamond detector decreases drastically at cryogenic temperatures. This has been only tested using closed radioactive sources [31], [32] and has not been confirmed for other radiation types, including neutrons. From this, three main areas for scientific contribution were identified and are the basis of this work:

1. Develop an apparatus to test the charge collection efficiency of a diamond detector at cryogenic temperatures with light and heavy particles as well as neutrons and  $\gamma$ -rays. This requires the development of an experimental setup based on a cryogenic pump, instead of using a liquid helium Dewar as to our knowledge was the only previously used approach. In addition, this setup needs to be connected to a particle accelerator. Particle accelerators and cryogenic pumps contain a lot of noise sources, and the apparatus must be highly optimized to allow for the measurement of very small signals which are expected from the diamond detector at cryogenic temperatures [65], [94].
2. Assess for the first time the charge collection efficiency behavior from room temperature to cryogenic temperatures for various ion,  $\gamma$ -ray, and neutron radiation and identify the main physical parameters that affect the CCE at cryogenic temperatures to aid in the understanding of the underlying physics behind this phenomenon [94], [95].
3. Optimization of the analog and digital components of the signal processing chain to maximize neutron measurement efficacy in a mixed radiation environment at cryogenic temperatures. Benchmarking and the creation of a database of neutron and  $\gamma$ -ray TCT pulse shapes. Comparison of the pulse shapes to theory and development of a PSD algorithm to separate neutron events from  $\gamma$ -rays [95].

On the basis of the above, this chapter begins with the description of two experiments in section 6.1 that are, to our knowledge following a literature review, the most relatable to this work. Results and methodologies from these two experiments are particularly relevant to the aim of this

work. Both experiments utilized a liquid helium Dewar to achieve cryogenic temperatures and a radioactive source,  $^{241}\text{Am}$  and  $^{252}\text{Cf}$ , respectively [31], [32]. The results of the experiment utilizing the  $^{241}\text{Am}$  source are compared to data acquired in this work for alpha particles in section 7.2. As will be described in section 6.1, the data for neutrons acquired from the experiment utilizing the  $^{252}\text{Cf}$  source are inconclusive and could not be used as a reference. This section also describes in more detail the expected operating environment for the neutron detector ( $\mu\text{LoM}$ ) being developed and the constraints brought on by this. These constraints influenced the design of the detector, and it was also one of the reasons why PSD was chosen for this work (described previously in section 5). All the results described from section 6.2 to the end of this dissertation present original work performed as a part of this thesis. This is also a first experimental test of the original hypothesis which is to determine if a diamond-based detector can function as a neutron detector at cryogenic temperatures. This includes the design of the electrodes which were evaporated onto the diamond crystal, the design and construction of the detector PCB and enclosure for noise minimization, the design and construction of the vacuum chamber and integration with the cryopump. As well as the conceptualization and programming of the remote-control system and the data acquisition system along with modification to the DAQ software SPECTOR which all had to work synchronously. All the simulation also had to be performed as part of this work to determine the correct experimental parameters.

Section 6.2 describes the bare scCVD diamond crystal that has been purchased and which was made into a detector as a part of this work investigations. This allowed for the optimization of the experiment down to the lowest level, including the design of the electrodes. Section 6.3 describes the innovative cryogenic setup constructed to cool the detector and allow for various ion beams from particle accelerators to impinge on it. To operate this experimental setup, described in section 6.4, a custom control and acquisition system had to be developed and optimized for the expected signal characteristics. Furthermore, to successfully investigate the performance of the detector at cryogenic temperatures, experimental parameters had to be determined by performing Monte Carlo simulations (presented in section 6.5). From the simulations, experimental parameters such as which ion beam and at what energies should be used to systematically test the detector were determined. The last section in this chapter describes each performed experiment and the measurement procedure that was followed. Each experiment procedure was derived from information found in literature to minimize systematic errors. Systematic error that could arise from

polarization effects (section 3.3) or induced noise (section 4.2), among others, could greatly influence the results. Therefore, a lot of effort was dedicated to systematically going through each step in the experimental procedure and comparing them to the literature in order to ensure standards are followed.

To summarize, the whole chapter 6 is devoted to the design, development and construction of a test apparatus which has the capability of cooling and maintaining a diamond detector at various temperature setpoints from room temperature down to cryogenic temperature while allowing for the impingement of accelerator ions, gamma radiation and neutrons on the detector in a controlled environment. The following section will present the results of the experiments performed along with their analysis, evaluating the performance of a diamond detector at cryogenic temperatures in various radiation fields and identifying the main parameters which affect the performance. The final section of this work (chapter 7) will be devoted to the analysis of the TCT datasets obtained during the experiments, the processing of these datasets to benchmark the various signal shapes expected from the detector. Following this benchmarking, various PSD techniques will be applied to the datasets and their performance evaluated.

## **6.1 $\mu$ -Loss Monitors for DONES**

The design of the apparatus was dictated by the type of data which was going to be collected to prove the hypothesis that a diamond detector can be used at cryogenic temperatures for neutron detection. As stated in the introduction, this work is motivated by its potential application of using a diamond-based detector as a  $\mu$ LoM for the beam diagnostic in DONES. Therefore, work already performed in the preliminary studies by other authors, to evaluate the operation of a diamond detector at cryogenic temperatures will first be presented and their conclusions outlined as these guided the direction of this research and influenced the design of the experiments.

Preliminary research on the feasibility of using diamond detectors for  $\mu$ LoM to measure the neutron flux for the Linear IFMIF Prototype Accelerator (LIPAc) has been performed by a group from CEA Saclay Nuclear Research Center. This section will summarize their published work presented in [3]–[5], [32] since the DONES facility is an evolution of LIPAc. DONES will consist of two accelerators each capable of providing a deuterium beam of 40 MeV at 125 mA while LIPAc is a test setup of the first components of the accelerator as illustrated in Figure 6.1.

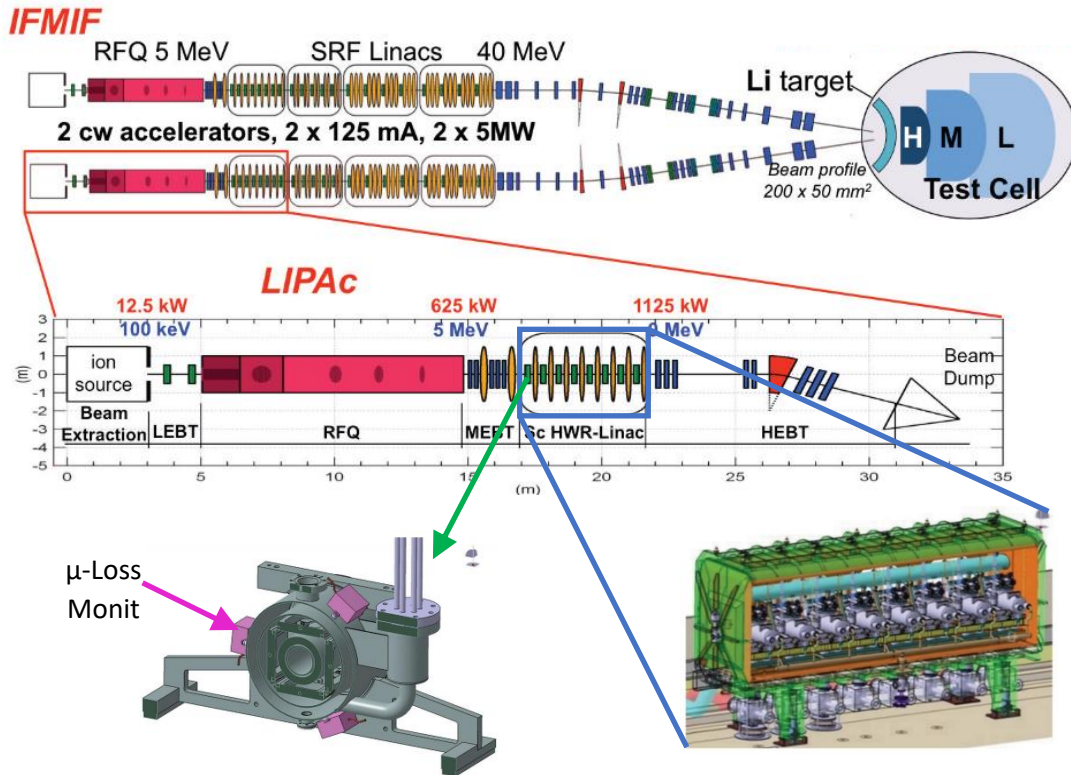


Figure 6.1 -  $\mu$ -loss monitor location.

The largest beam halos are expected right before the superconducting solenoid focusing magnets located inside the half wave resonator (HWR) cryostat and it is therefore recommended that the  $\mu$ LoM be placed as close as possible to the beam axis right next to the magnets as illustrated in Figure 6.1. Furthermore, to provide redundancy and angular information, three  $\mu$ -loss monitors are planned be placed at  $120^\circ$  to each other around the beam axis. Radiation at this location will be caused by the emission of secondary particles from the interaction of the deuterium beam with the beam tube wall. Neutrons are generated from the deuterium breakup and D-D reactions, along with  $\gamma$ -rays and x-rays from the superconductive cavities. The neutron and  $\gamma$ -ray flux at the  $\mu$ LoM location was simulated for the first HWR module which accelerates the deuterium beam from 5 MeV to 9 MeV. The simulated energy spectra are displayed in Figure 6.2 where the top plot (a) contains both the neutron and  $\gamma$ -ray spectrum on a logarithmic energy (x-axis) scale, while plots (b) show the same spectrum separately. It can be concluded from these spectra that the  $\mu$ LoM should be sensitive to neutrons up to a few MeV in energy and able to discriminate these neutrons in a  $\gamma$ -ray background with energies up to 10 MeV. X-ray radiation is also expected to be significant inside the HWR cryostat, however their energy range will be shifted to smaller energies and has

not yet been simulated. It is expected that the energy distribution of gamma and neutron radiation will shift to higher energies for the subsequent HWR where the beam energy is higher.

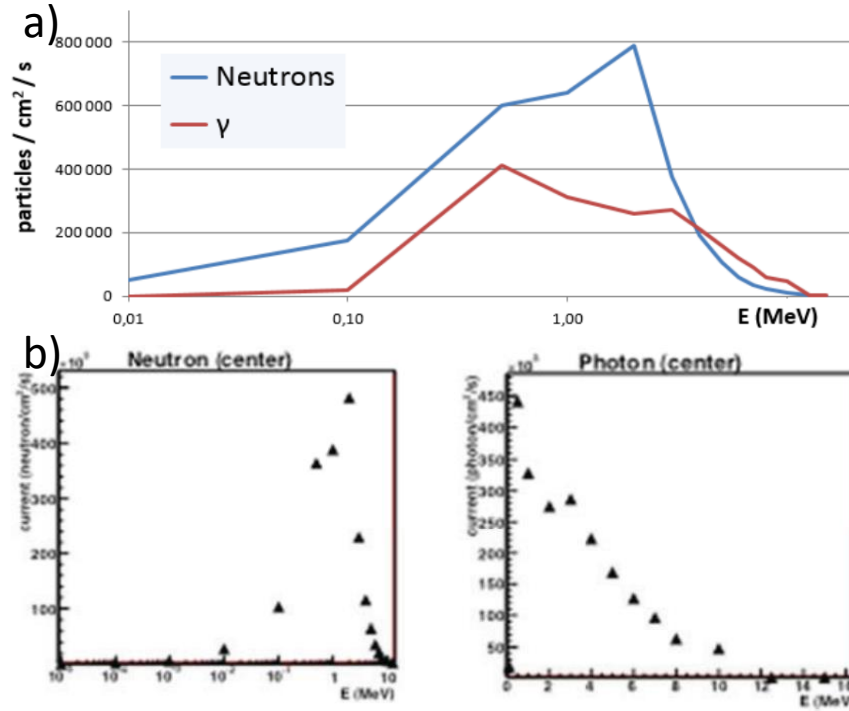


Figure 6.2 - Radiation at  $\mu$ -loss monitor location. a) combined plot, logarithmic energy scale. b) separate plots, linear energy scale for  $\gamma$  radiation.

Several experiments were performed by the CEA group to confirm the suitability of diamond for its operation as a  $\mu$ LoM. Jan Egberts [3], as part of his PhD thesis, tested a diamond detector in a Dewar with a Californium ( $^{252}\text{Cf}$ ) source at 77 K using liquid nitrogen and at 4.2 K using liquid helium.  $^{252}\text{Cf}$  decays to Curium ( $^{248}\text{Cm}$ ) by emitting a 6.1 MeV  $\alpha$  particle with 97% probability. More importantly,  $^{252}\text{Cf}$  has a 3% probability of undergoing spontaneous fission producing, on average, 3.75 neutrons with a most probable energy of 0.7 MeV and average energy of 2.1 MeV [92]. Since the source was placed outside of the Dewar, alpha particles were absorbed and only the neutron spectrum was expected to reach the diamond. However,  $\gamma$ -rays of energies below 150 keV are also emitted through the two decay chains of  $^{252}\text{Cf}$ . The resulting energy spectra acquired in their experiments at lower temperatures matched the room temperature spectra. The only recognized difference was in the high energy part of the acquired spectra which was expected due

to the lower CCE of the diamond at lower temperatures. These experiments confirmed that the diamond detector works at cryogenic temperatures, which was the primary goal of these experiments. However, since experiments were done in mixed  $\gamma$ -ray/neutron radiation fields, they did not confirm that the detector actually registered neutrons, since no differences in the energy spectra were observed when a  $\text{CH}_2$  neutron absorber was placed between the  $^{252}\text{Cf}$  source and the diamond. Experiments with neutrons of the same author were performed only at room temperatures using a particle accelerator. Neutrons of 0.6, 0.75, 1.2 and 2.1 MeV were generated using various beam-target combinations. The resulting neutron energy loss spectra discriminated based on time-of-flight with an associated  $\gamma$ -ray emission are presented in Figure 6.3.

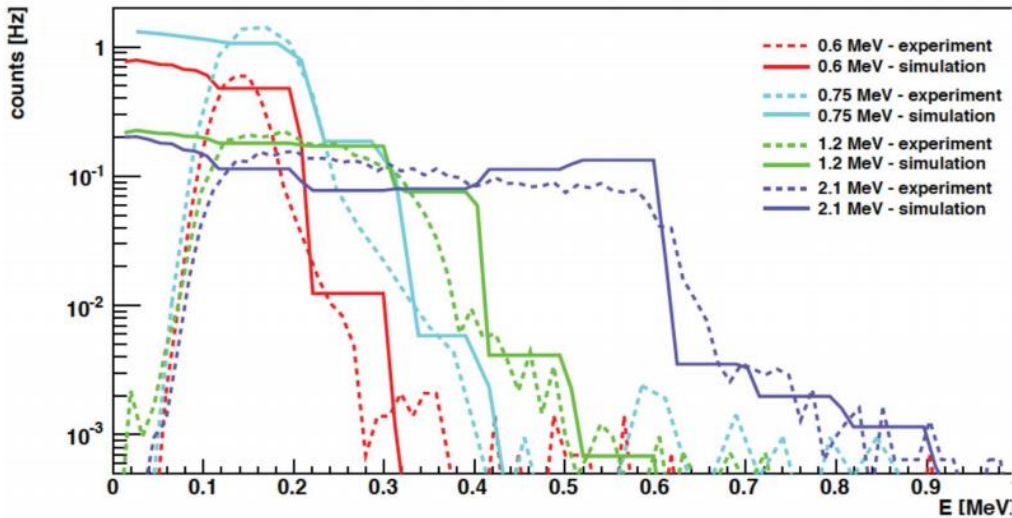


Figure 6.3 - Neutron energy loss spectra and simulations [3].

Furthermore, experiments were also conducted to test the Front-End Electronics (FEE) to estimate the effects of the superconducting solenoid, cable length and preamplifier placement will have on the acquired signal from the detector. Due to the  $\mu\text{LoM}$  position inside the HWR cryomodule, a minimum cable length of 3 meters is needed to separate the diamond from the preamplifier. Due to the low capacitance of diamond detector, the length and therefore capacitance of the cable itself will greatly impact the final noise in the signal arriving to the data acquisition system. It is therefore proposed to place a broadband radiation hard amplifier next to the cryostat three meters from the detector followed by another 20 meter cable leading to the electronics room as illustrated in Figure 6.4. The broadband amplifier was also used with a threshold counter/scaler

to determine the rate of particles impinging on the diamond detector. The experiment was performed using a Cobalt-60 ( $^{60}\text{Co}$ )  $\gamma$ -ray source and the signal arriving at the counter had a sufficient SNR for discrimination based on pulse height threshold. Further experiments were proposed to use a second shaping amplifier in the electronics area with an analog to digital converter (ADC) to obtain the full energy deposition spectrum. However, no publications were found for this proposal.

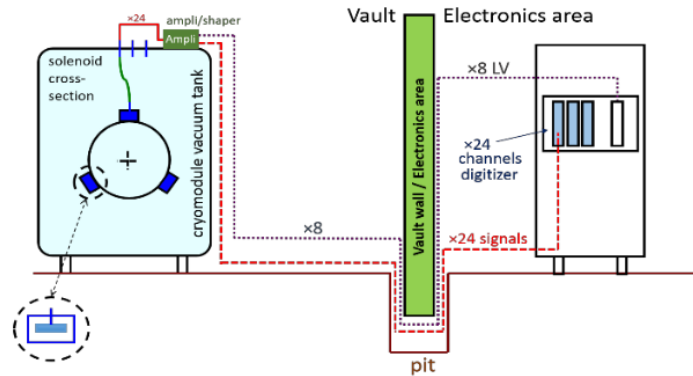


Figure 6.4 - Front End Electronics Setup.

Additional experiments were performed by the RD42 group at CERN at low temperatures but only to evaluate the radiation hardness of diamond detectors when exposed to large levels of radiation from proton beams at the Large Hadron Collider (LHC) [47], [96]. All performed experiments by the group confirm that a diamond detector can function as a  $\mu\text{LoM}$ . However, many other aspects must be explored in order to successfully create a  $\mu\text{LoM}$ .

## 6.2 Diamond detector

The design of the diamond detector used in this work was based on a scCVD diamond of detector grade produced by Element Six Ltd. (E6). The diamond crystal was an area of  $4.7 \times 4.7 \text{ mm}^2$  and a  $300 \text{ }\mu\text{m}$  thickness. To minimize the number of parameters and simplify the signal analysis, a simple coplanar geometry was chosen for the electrodes. The top and bottom of the crystal were metalized in the Diamond Sensors Laboratory of CEA-LIST with  $200 \text{ nm}$  thick tungsten with an area of  $3 \times 3 \text{ mm}^2$  by using the photolithographic technique (Figure 6.5a).



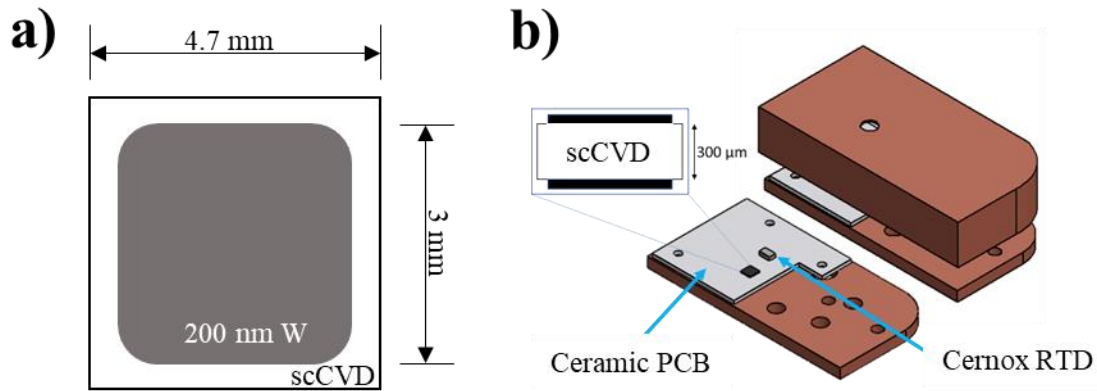


Figure 6.5 - Detector assembly. a) Electrode configuration on the diamond crystal b) Diamond mounted on PCB.

The quality of the bond between the electrodes and the diamond crystal is a critical parameter which influences the noise in the signal readout of the detector. It is desirable that the metal diamond interface is ohmic, that the current flowing through the device as a function of applied bias voltage is linear. However, this interface can also be nonlinear with respect to the bias voltage (Schottky contact) where a potential barrier is formed at the interface of the two materials. This potential barrier is the result of matching the work function of the metal contact with the Fermi level in the semiconductor at the metal-semiconductor interface. However, the metal that will create a good ohmic contact is not necessarily the best electrode material as it may be a poor conductor or may be difficult for connecting external wires. To overcome this issue, electrodes made from multiple layers (such as Ti/Pt/Au) or using diamond-like carbon (DLC) as the first layer are commonly used [18], [47]. For the purposes of this work, W was chosen for the contact metal due to its temperature stability and a work function that is close to that of diamond, knowing that wire bonding external leads to the electrode would be difficult. The I-V measurement of the detector, illustrated in Figure 6.6, shows an almost ohmic contact and a very low leakage current.

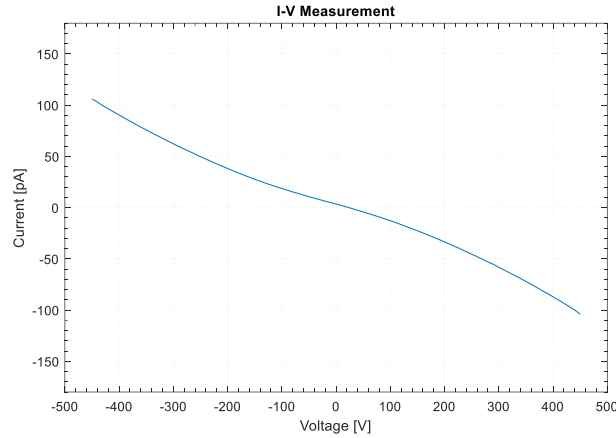


Figure 6.6 - I-V Measurement of diamond detector.

In order to study the behavior of the diamond detector at cryogenic temperatures, a printed circuit board (Figure 6.7) was designed and manufactured out of an aluminum nitrate ( $\text{Al}(\text{NO}_3)_3$ ) substrate instead of FR4 with the wire leads made from 70  $\mu\text{m}$  copper coated with electroless nickel immersion gold (ENIG). The diamond crystal and the Cernox CX-1070 temperature sensor were mounted on the PCB using a silver paste which has excellent thermal and electrical properties at cryogenic temperatures. Wire bonding alone to the W top contact resulted in a weak mechanical bond and a small amount of silver paste had to be used in conjunction with the wire bonding machine to secure the contact.

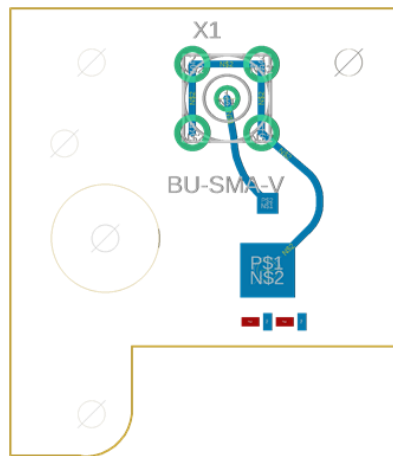


Figure 6.7 - Detector PCB with connector and pad for diamond crystal.

To further minimize the induced noise, the diamond crystal and PCB were enclosed in a copper case to act as a Faraday cage with only the signal wires protruding from the side and a hole left above the diamond crystal allowing for the ion beam to pass through as illustrated in Figure 6.5b.

### 6.3 Cryogenic system

As described above in section 6.1, previous studies achieved cryogenic temperatures by submerging the detector into a Dewar of liquid helium and closed radioactive sources were either attached to the detector inside the Dewar or placed right outside the Dewar. While this method achieves lower temperatures with minimal noise added to the system, it also limits the experiments to the use of closed radioactive sources. To avoid this limitation and allow for experiments using ion beams, it was decided to use a cryopump instead to achieve cryogenic temperatures at the expense of added noise due to the mechanical operating principle of such a system. The detector assembly was mounted on the cold-head of a Leybold-Heraeus RPK400 cryopump along with a 25 Ohm resistor for temperature regulation. A purpose build vacuum chamber was fabricated and attached to the cryopump containing feedthroughs for the detector signal, temperature sensors signal and heater connections. The experimental chamber was designed using the SolidWorks computer aided design (CAD) package (Dassault Systèmes, 2020) to assure a compact design and a proper alignment to the ion beam.

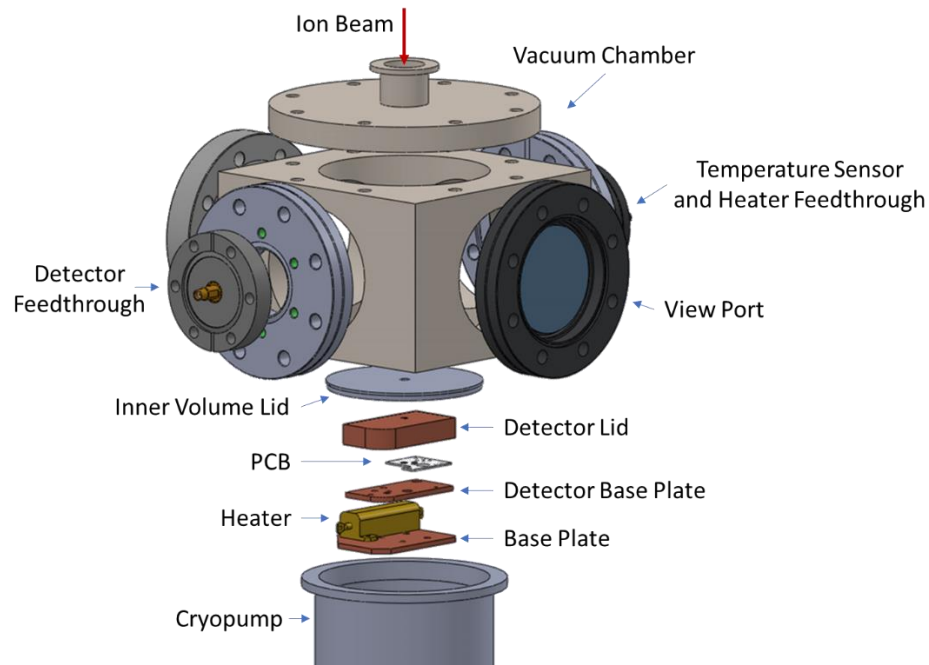


Figure 6.8 - Exploded view of experimental setup.

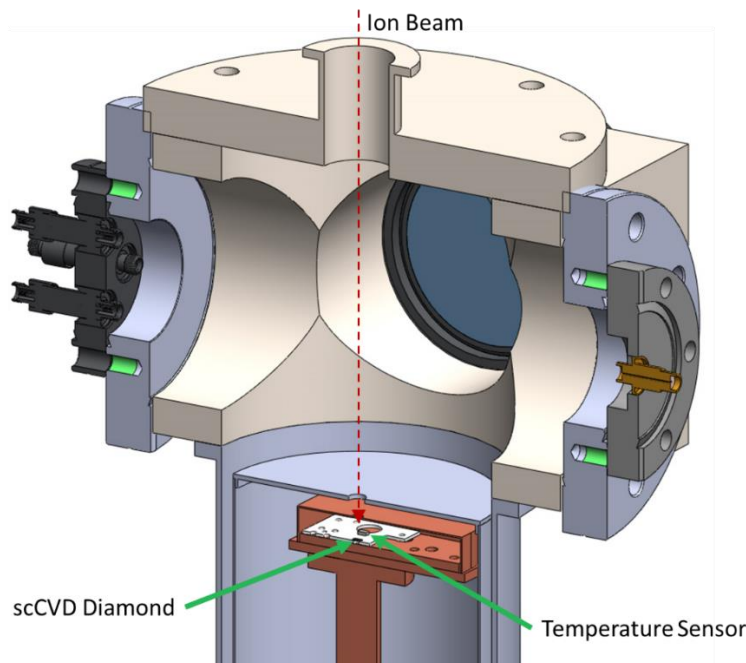


Figure 6.9 - Cross-section view of experimental setup.

Figure 6.8 illustrates all the components of the vacuum chamber and the cryopump assembly. As can be observed from the figure, the diamond crystal on the PCB is enclosed in the detector case which rests on top of a copper base plate along with the heater. The detector and heater are mounted on the cold-head of the cryopump as depicted in Figure 6.9. These components are further enclosed by a lid, creating an inner volume around the cryopump cold-head for better thermal isolation. Only the cables connecting the detector, thermometer and heater pass through the inner volume lid and are connected to the feed throughs located on the vacuum chamber. The temperature sensor and heater were connected using a phosphor bronze (CuSnP) alloy single lead wire which is optimized for cryogenic applications. The cryopump is designed to cool the detector to the minimum achievable temperature, the heater was added and used to achieve all intermediate temperatures required for this work. The detector is connected using a standard shielded coaxial cable with a subminiature version A (SMA) connector to minimize the amount induced noise, however this is not optimal for cryogenic purposes and limits the lowest achievable temperature the system can reach due to thermal leaks. Using a combination of a rotary mechanical vacuum pump coupled with a turbo molecular vacuum pump (Pfeiffer Vacuum HiCube 80 Eco), a pressure of  $\sim 10^{-6}$  mbar was achieved at room temperature. With these conditions, the lowest achievable temperature of the system at the position of the diamond was 46 K. The foreseen operating

temperature of 4.5 K required for  $\mu\text{LoM}$  in DONES was not achieved. However, based on previous studies found in literature and discussed above, the response of a diamond detector at 46 K should be comparable to the response at 4.5 K.

## 6.4 Data acquisition and experiment control

Experiments using this setup were performed with ion beams, neutron, and  $\gamma$ -rays, that is in intense radiation fields, therefore all data acquisition and instrument control had to be performed remotely. Remote control was achieved using the Experimental Physics and Industrial Control System (EPICS) framework [97]. Dedicated input output controllers (IOC) with individual drivers were written for each instrument used and compiled to run on a Raspberry Pi Model 3B+ single board computer. The Cernox CX-1070 RTD cryogenic temperature sensor signal was readout with a Lake Shore Cryogenic Model 211 Temperature Monitor which was connected to the Raspberry Pi using the RS-232 communication protocol. The 25 Ohm resistor (heater) was powered using a Hameg HMP2030 Power Supply while the bias voltage on the detector was provided by a ISEG NHQ-202M high voltage power supply. Figure 6.10 provides a schematic overview of the connection between each instrument and the control computer.

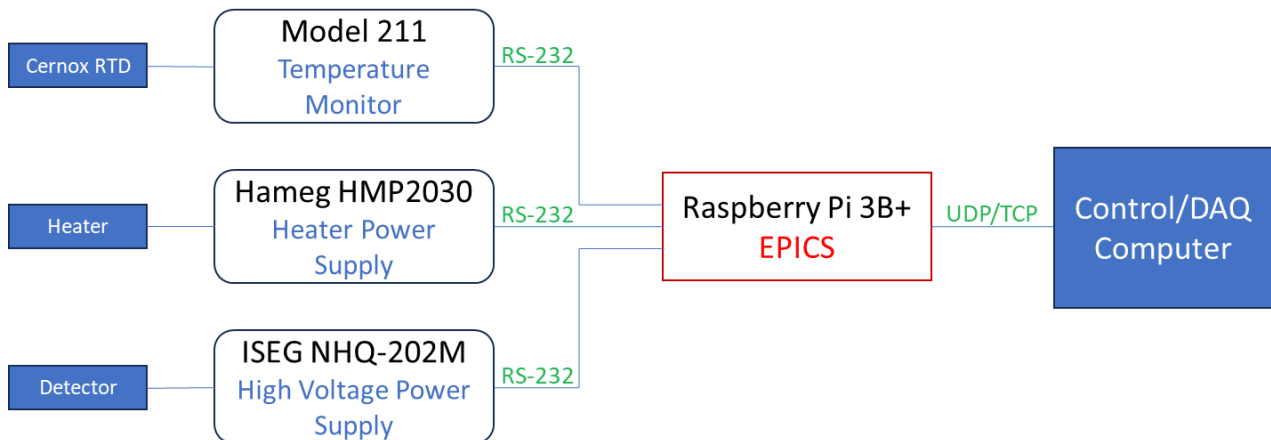
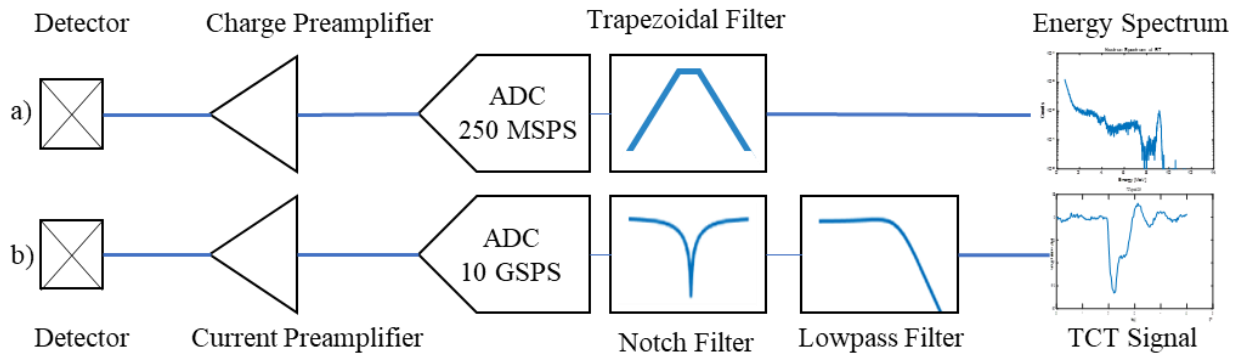


Figure 6.10 - Instrument Control Schematic.

Deploying EPICS allowed for the connection of multiple instruments using the RS-232 serial communication protocol with device specific commands to be abstracted to general commands which could be sent and received using the UDP/TCP protocol. Furthermore, the UDP/TCP protocol has the additional benefit of being compatible with the LAN network and allowed for

complete experiment control from a safe location. A soft proportional-integral-derivative (PID) controller was also programmed into EPICS to acquire temperature values and control the current output of the heater power supply. After calibrating the PID controller, temperature stability of  $\pm 0.1$  K was achieved. A human-machine interface (HMI) was created in Phoebus (Control System Studio, 2023) to control all three instruments from a single screen and automatically plotted all crucial information such as the temperature, heater current and detector leakage current.



*Figure 6.11 - Signal processing chain. a) Charge sensitive preamplifier for energy spectra acquisition. b) Current sensitive preamplifier for TCT signal acquisition.*

The signal processing chain and data acquisition setup varied depending on the type of data being collected. Two datasets were collected for each experiment to provide more information about the underlining physics of signal creation inside the diamond detector. Figure 6.11a illustrates the signal processing chain used for IBIC measurements to study the total energy of the impinging radiation collected by the detector. This is the first dataset acquired for this work. For this measurement a charge sensitive amplifier (described in section 0) was used to integrate the current pulse from the detector electrodes. Three different charge sensitive preamplifiers were studied, each optimized differently to maximize the SNR: Ortec 142, Amptek A250CF CoolFET and Cividec C6. The Ortec 142 preamplifier is the most commonly used preamplifier in nuclear instrumentation and achieves a good SNR for a wide variety of experiments involving the detection of ionizing radiation. An energy resolution of 181 keV for 5.1 MeV alpha particles was achieved with this preamplifier. However, when this amplifier was used in conjunction with the cryopump, dielectric noise caused by the vibration of the chamber and associated cables at the feedthroughs degraded the resolution and made it unusable at cryogenic temperatures. The Amptek A250CF

CoolFET preamplifier is also a general application preamplifier with the addition of a Peltier cooler added to the first stage transistor. This decreases the thermal noise in the transistor channel resulting in a better SNR. An energy resolution of 106 keV for 5.1 MeV alpha particles was achieved with this preamplifier. However, as with the Ortec 142 preamplifier, the dielectric noise caused by the vibration of the cryopump was too large for use at cryogenic temperatures. The two preamplifiers described thus far are general purpose preamplifiers which can be used with a wide variety of detector types.

The Cividec C6 detector preamplifier is specifically designed for diamond detectors. It is optimized for the fast signals expected from a diamond detector and has a Gaussian impulse response achieved by an RC-CR bandpass filter. The impulse response of this preamplifier is a Gaussian shape with a rise time of 3.5 ns and a pulse width of 10 ns [98]. This filter is specifically designed for signals generated from a diamond detector and therefore a more optimally chosen cut-off frequency. An energy resolution of 98 keV for 5.1 MeV alpha particles was achieved with this preamplifier. Additionally, due to the highpass filter dielectric noise from the cryopump was filtered out at the beginning of the signal processing chain allowing for a better SNR even at cryogenic temperatures. As further depicted in Figure 6.11a the fast exponentially decaying signals from the preamplifier were digitized using a 250 MSPS 12-bit ADC and processed with a digital trapezoidal filter with a rise/fall time of 80 ns, no flat top and the differentiation constant (M) set to 0 due to the fast decay time of the signal inside a Virtex 6 FPGA. This filter was used to further increase the SNR as described in section 4.3. The FPGA extracted the pulse height of each signal and stored it along with other parameters such as the signal timestamp and ion beam position to the onboard DDR4 memory. The acquisition/control computer running the SPECTOR software read out this information through the TCP protocol, compiled energy histograms and saved the data on an event by event basis for further analysis [65].

The second dataset was collected using the TCT method with a signal processing chain illustrated in Figure 6.11b. This dataset provides insight into the movement of the charge carriers generated inside the volume of the diamond detector for the purpose of identifying the impinging type of radiation based on the pulse shape. For these purposes a current sensitive preamplifier had to be used which acts as a broadband amplifier and does not alter the signal shape. The amount of noise induced in the signal at the first stage amplification is critical because all further stages will amplify this noise along with the signal. This makes the first stage amplifier the critical component

in signal processing chain as was deduced from the analysis of the signal processing chain in section 4.2. Charge sensitive amplifiers contain filters to limit the amount of noise that is amplified by later stages, however the broadband requirement of a current sensitive preamplifier for TCT measurement does not allow for this as it will modify the signal shape. Therefore, all noise is amplified along with the signal. Since this noise depends on the environment where the experiment is performed, the exact spectrum of the noise cannot be analytically determined. Two current sensitive preamplifiers were tested (Micron Semiconductor DBA-IV and Cividec C2-HV) in order to experimentally determine the impact of this noise and how to minimize it. Both preamplifiers are very similar in performance and the Cividec C2-HV preamplifier was chosen in the end due to the requirement of one less power supply in the experimental setup. As calculated in section 3, for 5 MeV alpha particles, 7.8  $\mu\text{A}$  of current is induced on the electrode with a pulse width of 5 to 10 ns at room temperatures. Therefore, using a preamplifier with a gain of 40 dB over a 50 Ohm system, a maximum pulse height of 400 mV is expected. Due to the width of the expected pulse, a fast digitizer had to be used. For the TCT experiments, the LeCroy WaveMaster 8500A oscilloscope with an acquisition speed of 10 GSPS and a bandwidth which was limited to 3 GHz was used due to the preamplifier bandwidth being only 2.5 GHz. Limiting the bandwidth to 2.5 GHz removes the sharper edges in the signal which result from higher frequency components and effectively smooths out the signal as can be observed when comparing Figure 7.14 a) and b), respectively. Two trigger conditions were set on the oscilloscope for isolating the TCT pulses from background noise caused by the operation of the accelerator and other equipment. An amplitude trigger condition was set to -20 mV, just outside the noise level. As illustrated in Figure 7.11a, sinusoidal noise caused by the interference of the neutron generator deuterium ion source plasma oscillator could not be completely eliminated. This superimposed noise limited how low the amplitude trigger level could be and consequently the minimum acquired signal amplitude. Neutrons and  $\gamma$ -rays with an energy less than 2 MeV were therefore not recorded. As is observed from Figure 7.4a this portion of the spectra is dominated by incomplete charge collection events, higher Q value reactions and elastic collisions. Due to the wide variety of different possible signal origins, this portion of the spectra provides no additional information for this work at room temperature. However, at cryogenic temperatures where the charge collection efficiency is low, this will result in far less events being recorded requiring longer experiment times to acquire the same number of traces. The second trigger condition was therefore set for the pulse width which



helped filter our high frequency burst noise caused by cell phones and other wireless antennas in the vicinity. The width trigger was estimated to be in the range of 4 ns at room temperature, using the values of mobility of the charge carriers from literature [51], the thickness of the diamond and the applied bias. Therefore, the minimum pulse width trigger condition was set to 3 ns and further decreased down to 2 ns at low temperatures. It was found that the aforementioned trigger criteria provided the optimal balance for acquiring the smallest signal levels without the trigger being dominated by noise. All data acquired was stored locally on the oscilloscope and further processed offline using the MATLAB (MathWorks, 2017) software package. Using this procedure, more than 3000 TCT traces were acquired at each temperature setpoint per experiment.

After evaluating the performance of three charge sensitive preamplifiers and two fast current sensitive amplifiers, the optimal signal processing chain for IBIC measurement was found to be the Cividec C6 charge sensitive preamplifier couple with the developed DAQ based on the Virtex 6 FPGA and 12-bit 250 MSPS ADCs. As described in the paragraph above, the parameters of the trapezoidal filter in the FPGA had to be modified beyond the usual functionality to disable the differentiation component in order to efficiently process the fast Gaussian impulse response of the non-standard preamplifier. The signal processing chain used by the most related experiment from literature, performed by Marrocle et al. [32] (described in section 6.1) used a fast charge sensitive amplifier developed by GSI [99] coupled with a commercially available digitizer (CAEN V1720) which has similar characteristics as to the DAQ used in this work. The impulse response function of the preamplifier was not found in literature, nor were the exact parameters used by the digital pulse processing unit in the CAEN digitizer. The optimal signal processing chain for the TCT measurement was derived from this work was the combination of a Cividec C2-HV preamplifier coupled with the LeCroy WaveMaster 8500A 10 GSPS oscilloscope with the bandwidth limited to 3 GHz. The novel approach of using two trigger conditions, as described in the paragraph above, to filter the acquired signals in real time with the added lowpass and notch filter (described in section 7.3) were not found to be used before in literature. The most related experiment found in literature, performed by Jansen et al. [31] (described in 6.1) also used a Cividec preamplifier however, the model was not specified. In this experiment similar two trigger conditions were used however, the width condition was not modified for measurements at lower temperatures. Furthermore, all recoded pulses with a  $SNR < 3$  were rejected and no filtering was applied to the data. For this work, rejecting pulses with a  $SNR < 3$  was not an option as these signals are valid

and need to be recognized by a  $\mu\text{LoM}$  installed in the DONES accelerator. The additional filtering developed in this work allowed for the successful processing of signal with a  $\text{SNR} < 3$ .

## 6.5 Experiment simulations

Simulations were performed for each experiment to choose the parameters that best characterize the subject which was being investigated. Also, simulations are performed to predict the results of experiments and help with their interpretation. Processes involving radiation are stochastic by nature and therefore Monte Carlo based simulation tools were used for the preparation of the experiments. For experiments with ions, the SRIM [16] software package was used to simulate the ionization profile of various ion inside the diamond crystal. To minimize the number of unknown parameters in the experiment, it was crucial to choose the energy of each type of ion impinging on the diamond detector, so their trajectory (depth) was the same. Figure 6.12 shows the results of the SRIM simulations, depth profiles (left graph) and ionization profile (right graph) for each ion used in the experiment. Table 6.1 summarizes these results. The depth of  $5.6 \mu\text{m}$  was set for each ion due to the limitation of the acceleration voltage achievable by the particle accelerator.

Table 6.1 - Calculated ion energies for same depth in a diamond crystal.  $*E_{eh} = 13.6 \text{ eV}$  [100]

Ion	Energy [MeV]	Longitudinal Range [ $\mu\text{m}$ ]	e-h Pairs*
$\text{H}^+$	0.8	$5.6 \pm 0.2$	60,377
$\text{He}^{2+}$	3	$5.6 \pm 0.1$	226,415
$\text{Li}^{2+}$	5.6	$5.6 \pm 0.1$	422,642
$\text{C}^{4+}$	12.8	$5.6 \pm 0.1$	966,038

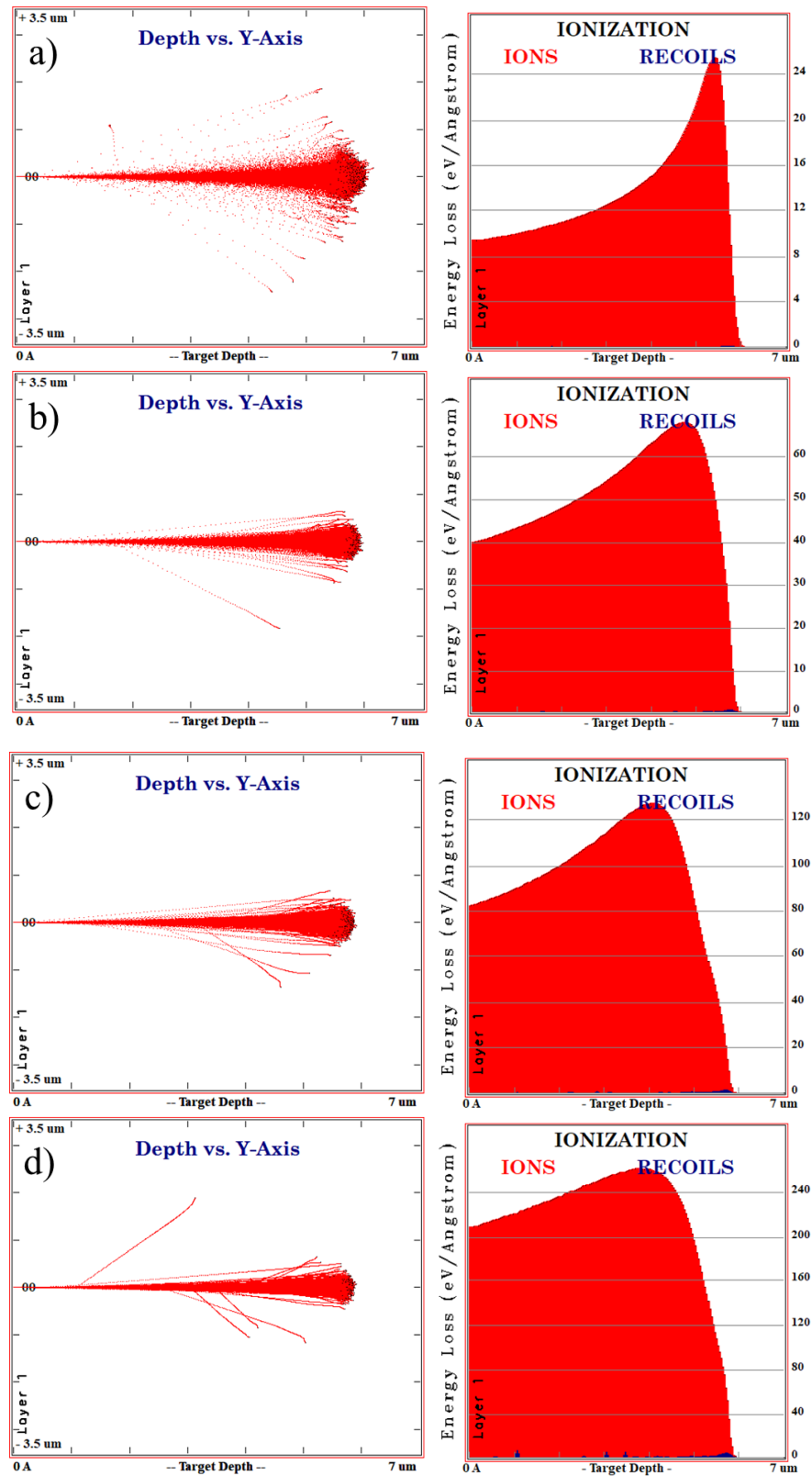


Figure 6.12 - SRIM simulation for ions. a) 0.8 MeV  $H^+$  b) 3 MeV  $He^{2+}$  c) 5.6 MeV  $Li^{2+}$  d) 12.8 MeV  $C^{4+}$ .

For experiments involving  $\gamma$ -rays and neutron radiation, Monte Carlo simulation were carried out by means of Geant4 (v9.6.3) [101] using the European Space Agency Geant4 Radiation Analysis for Space (ESA GRAS v3.3) simulation tool [102]. While CERN's ROOT Data Analysis Framework [103] was used to interpret the simulation. Geant4 allows for the simulation of the energy deposited inside materials using the Monte Carlo technique from which energy spectra can be calculated, predicting the ideal results of an experiment. These simulations were crucial for determining the energy of  $\gamma$ -rays most suitable for this work. That is, energy spectra which contain a well-defined Compton edge so they can be further evaluated as will be discussed in section 7.1 of this work. The Geant4 simulation results in a ROOT file with a tree structure containing all interaction locations and energy transfer from the impinging radiation to the set material. A ROOT script was written to process these results and calculate the cumulative energy deposition per  $\gamma$ -ray in the material and record these results in the form on a histogram as presented in Figure 6.13.

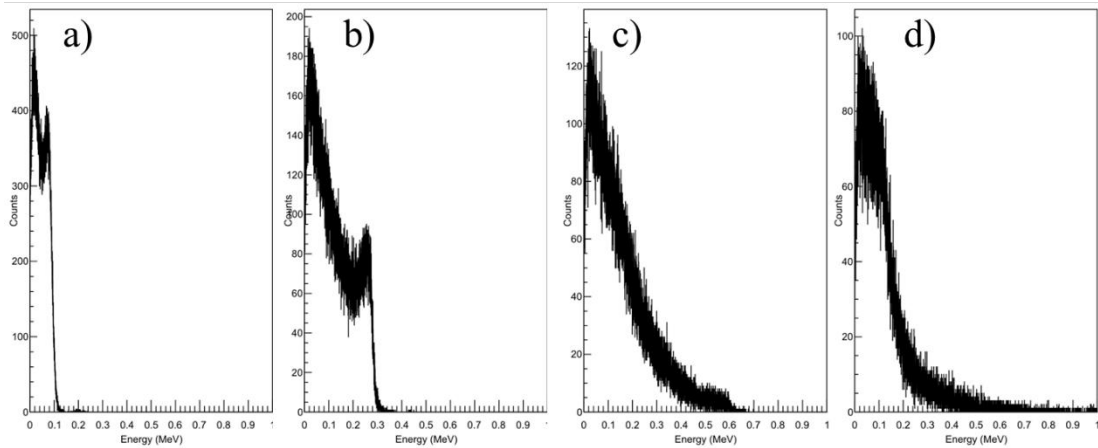


Figure 6.13 - Geant4 simulation of gamma ray energy deposition in a diamond crystal. a) 200 keV b) 440 keV c) 800 keV d) 2000 keV.

From the simulation results in Figure 6.13, it can be observed that the Compton edge is visible at lower  $\gamma$ -ray energies and is indistinguishable from the background at higher energies. Therefore for experiments with  $\gamma$ -rays, an energy of 440 keV which was possible to achieve using a particle accelerator and the  $^{23}\text{Na}(p,p'\gamma)$  reaction was chosen as will be discussed further in the following section. However the  $^{23}\text{Na}(p,p'\gamma)$  reaction produced two  $\gamma$  rays with higher intensity, specifically with energies of 440 keV and 1643 keV. Therefore, the resulting spectra will be a superposition of these two  $\gamma$ -ray energies as illustrated in Figure 6.14.

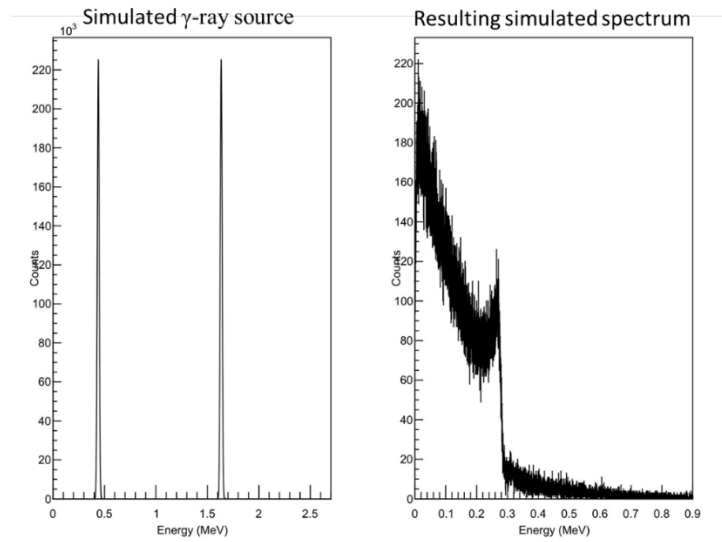


Figure 6.14 - Simulated spectra of the  $^{23}\text{Na}(p,p'\gamma)$  reaction which produces two  $\gamma$  rays of higher intensities at energies 440 keV and 1634 keV.

Neutron spectra were also simulated in Geant4 to aid with the analysis of the results. As described previously in section 2.3, neutrons can undergo many reactions inside the diamond crystal and simulations were vital to identify the various features in the neutron spectrum as illustrated in Figure 6.15.

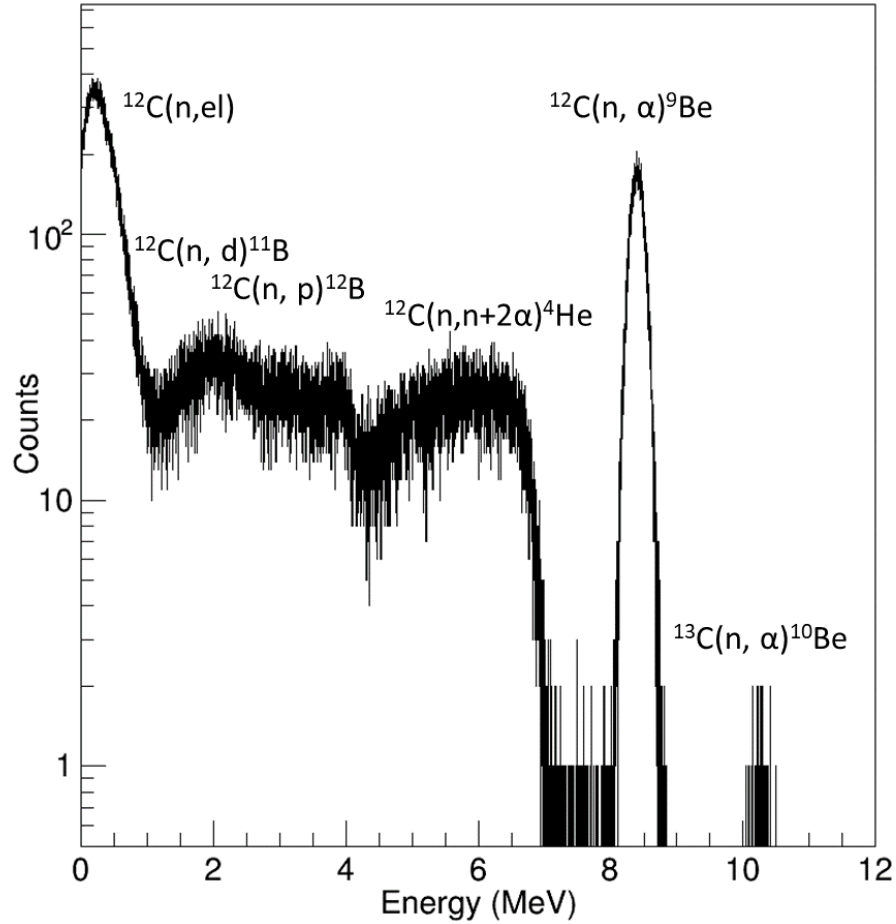


Figure 6.15 - GEANT4 simulation of 14.1 MeV neutrons on a diamond crystal.

## 6.6 Measurements

To evaluate the effectiveness of a diamond detector at cryogenic temperatures for such roles as a  $\mu\text{LoM}$ , three experiments were conducted using: 1. Ions, 2.  $\gamma$ -rays, 3. Neutrons. In this section all experimental parameters will be described as this is important for the evaluation of the resulting data. All experiments evaluated the response of a scCVD diamond detector from room temperature down to 46 K using the setup described in section 6.3 and collected data using the two methods described in section 6.4. Experiments with ions and  $\gamma$ -rays were performed at the Ruđer Bošković Institute Laboratory for Ion Beam Interaction, while experiments with neutrons were performed at the Ruđer Bošković Institute Neutron Generator facility and the Tandem Accelerator Facility at the Institute of Nuclear Physics, NCSR “Demokritos” in Athens, Greece.

### 6.6.1 Ions

For the experiment performed with ions, the setup was mounted downstream from the nuclear microprobe at the Laboratory for Ion Beam Interactions [104] as illustrated in Figure 6.16. The nuclear microprobe allowed for focusing the ion beam to micron dimensions and scanning the beam across the diamond detector surface. The main aim of this experiment was to measure the detector response from room temperature down to 46 K to different ions and compare their CCE. The ions and their associated energies used in this experiment were obtained from simulation and summarized in Table 6.1. As can be seen from Table 6.1, although the range of all ions is the same, the number of created electron hole pairs is significantly different between them. An average energy for charge pair creation of 13.6 eV [100] was used to approximate the generated number of charge carriers for each ion. This allowed for the study of the influence of ionization density on the CCE dependence on temperature since the carbon beam produced 16 times more charge carriers in approximately the same volume as the proton beam.

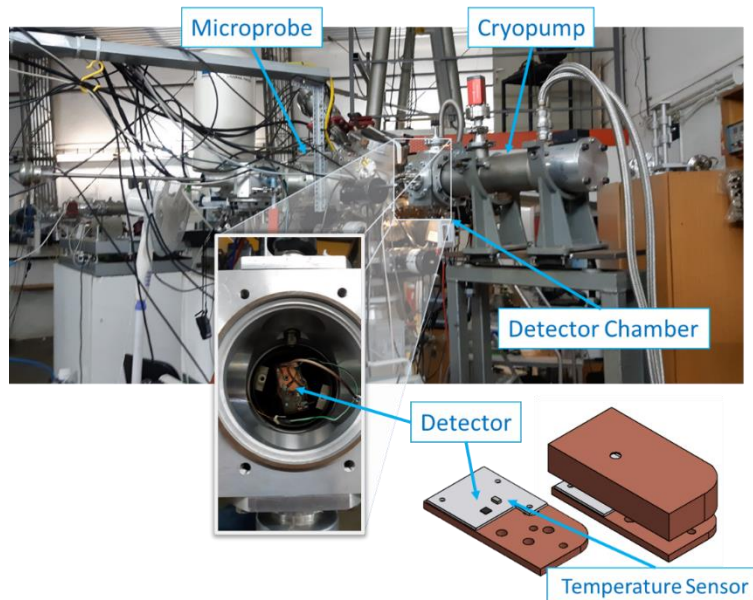


Figure 6.16 - Experimental setup installed downstream from the nuclear microprobe.

Before the experiment, the beam was focused and scanned over the detectors' surface at room temperature in order to select an appropriate region with homogeneous CCE. The typical size of the region of interest (ROI) selected for scans was of  $\sim 700 \times 700 \mu\text{m}^2$ , located between the detector

edge and the top electrode wire bond as can be observed from the IBIC map in Figure 4.16. The same figure illustrates an effect which is associated with creation of space charge within the scanned detector area and examined in section 3.3 of this work. In the region that was previously irradiated, the CCE of the detector gradually decreases. A shift in the spectrum is observed when comparing the signal from the ROI after irradiation (top blue spectrum of Figure 4.16) and a pristine region (bottom purple spectrum of Figure 4.16) of the detector. This is how polarization is presented in experimental measurement with diamond detectors. This phenomenon is not permanent and can be reversed, however, it had to be considered in order to obtain reproducible results. Therefore, when the temperature stabilized within  $\pm 0.1$  K of each set point, the bias on the detector was turned off and the detector was irradiated for 2 minutes. The detector was irradiated without bias to mitigate polarization effects, as during irradiation induced charges recombine with trapped charges accumulated during each measurement. This depolarization procedure was repeated before every acquired measurement. With the detector depolarized, the bias was raised to +300 V or 1 V/ $\mu\text{m}$  and the IBIC signal from the detector was acquired for about 1 minute. Even though the temperature was stabilized with a PID controller, temperature values were recorded every 10 seconds during the measurement and synchronized with the signal from the detector in the DAQ system. During the experiment at a +300 V bias applied to the top electrode, the leakage current was under 100 pA and therefore did not significantly add to the noise level of the system. The measurements were performed at six temperature setpoints: 46 K, 60 K, 70 K, 90 K, 110 K, 130 K and 150 K. Additionally, at each temperature, measurements were carried out at three bias voltages: +300 V, +350 V and + 400 V (1 V/ $\mu\text{m}$ , 1.17 V/ $\mu\text{m}$  and 1.33 V/ $\mu\text{m}$ ).

### 6.6.2 $\gamma$ -rays

The measurements with  $\gamma$ -rays were performed at the same laboratory by means of inelastic scattering  $^{23}\text{Na}(p,p'\gamma)$  at 2 MeV. This reaction produced two  $\gamma$ -rays with higher intensities, at 440 keV and 1634 keV using the setup illustrated in Figure 6.17. As was described in the previous section with simulations, the 440 keV  $\gamma$ -ray is of interest since it produces the well-defined Compton edge whose position can be evaluated as a function of temperature. The 1634 keV  $\gamma$ -ray does not produce a Compton edge but only adds an exponential background to the spectra and must be taken into account when analyzing the results.



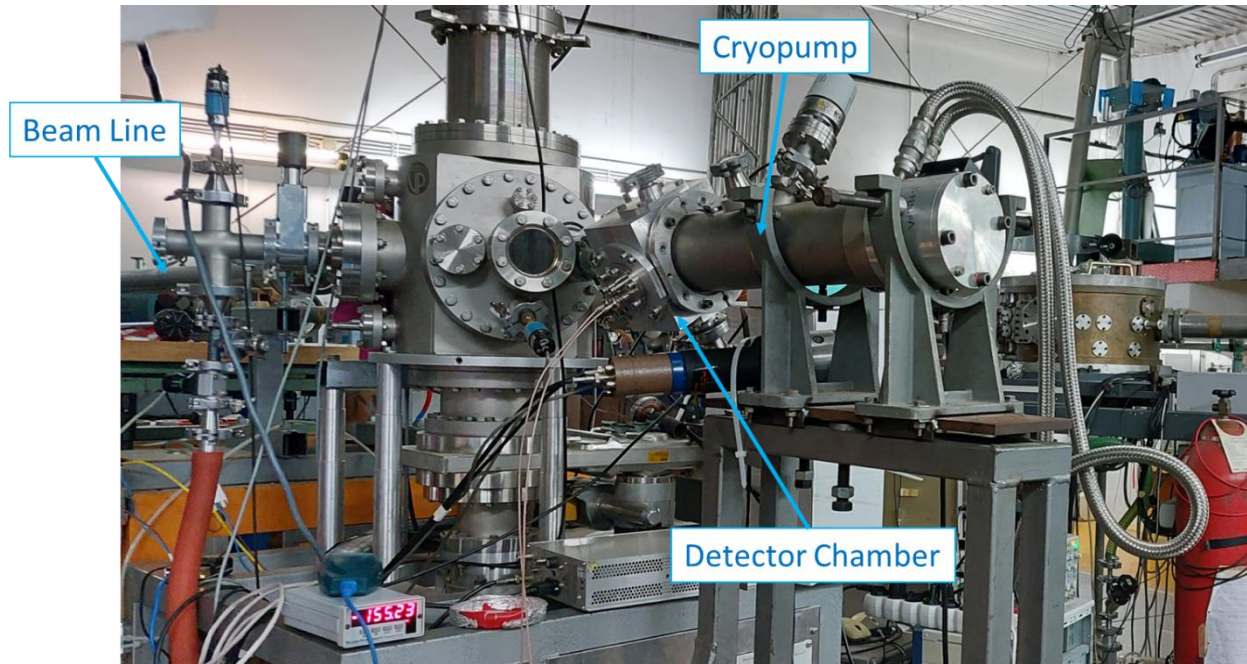


Figure 6.17 - Experimental setup installed at a beam line for high current 2 MeV H for  $^{23}\text{Na}(p,p'\gamma)\gamma$  production.

A sodium pellet was placed as close as possible to the detector, on top of the copper housing, to provide the most intense  $\gamma$ -ray field while blocking any stray accelerated protons from reaching the detector. The intensity of the  $\gamma$ -ray field was high enough to acquire appropriate statistics in a short period of time allowing for data acquisitions at 3 K intervals from 46 K to 120 K. Spectra above 120 K were not acquired since they were all identical, confirmed by the comparison of a spectrum acquired at room temperature. Although the intensity of the  $\gamma$ -ray field was high, due to the low probability and not localized interaction with the diamond crystal, polarization effects were not observed and therefore polarization mitigation strategies were not applied. The bias on the detector was again fixed to +300 V (1 V/ $\mu\text{m}$ ) which resulted in a 100 pA leakage current. Data was collected first using a charge sensitive preamplifier and the PHA method in the DAQ as described above, followed by TCT measurement using a current sensitive preamplifier and a fast oscilloscope. TCT signals from a  $^{60}\text{Co}$  closed radioactive source, 1.17 MeV and 1.33 MeV  $\gamma$ -rays, were obtained in addition to 440 keV  $\gamma$ -rays for the purpose of signal shape analysis using higher amplitude pulses with a better SNR.

### 6.6.3 Neutrons

For neutron irradiations, the experimental setup was placed downstream from a tritiated target used at the Ruđer Bošković Institute Neutron Generator which utilizes the  ${}^3\text{H}(d,n){}^4\text{He}$  reaction to produce a 14.1 MeV neutron field of  $10^7$  n/s in  $4\pi$  as illustrated in Figure 6.18. As observed from simulation, 14.1 MeV neutrons were chosen because they produce a sharp feature in the pulse height spectra, a  ${}^{12}\text{C}(n,\alpha){}^9\text{Be}$  peak at 8.3 MeV, which can be further analyzed to gauge the performance of the diamond detector.

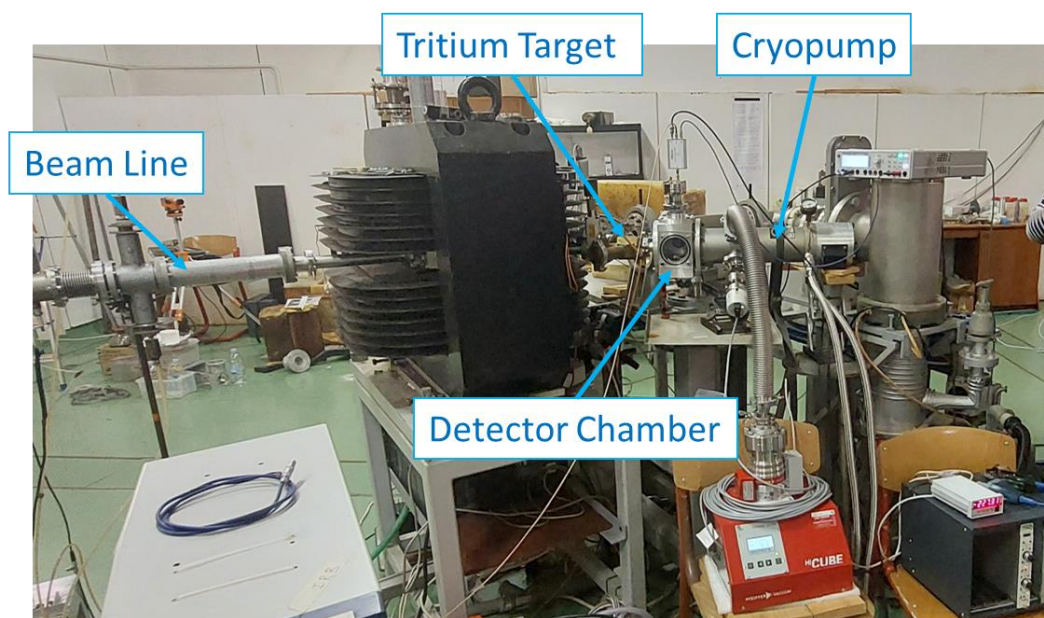


Figure 6.18 - Experimental setup installed the neutron generator downstream from a tritium target.

The neutron flux is the highest at the tritium target and therefore it is beneficial for the detector to be mounted as close as possible to it. However, due to the size of the vacuum chamber, the detector had to be placed at 165 mm from the tritium target which limited the neutron flux. Due to the small size of the diamond detector, more time was required to acquire enough statistics for the spectra which restricted the number of temperatures which could be measured during the experiment. In total 11 temperature setpoints were selected: 46 K, 55 K, 60 K, 70 K, 80 K, 90 K, 100 K, 110 K, 120 K, 200 K and 298 K. The bias on the detector was again fixed to +300 V (1 V/ $\mu\text{m}$ ) with a leakage current of 100 pA. Data was collected again using both types of preamplifiers at each temperature.

Experiments with neutrons we also performed at the Tandem Accelerator Facility at the Institute of Nuclear Physics, NCSR “Demokritos” in Athens, Greece [105]. The accelerator facility at Demokritos has the additional benefit of using the  $^2\text{H}(d,n)^3\text{He}$  reaction to produce neutrons of lower energies. For the purpose of the experiment, an end station used for irradiation of materials at cryogenic temperatures was modified to hold the diamond detector. Temperatures down to 10 K were achieved with this setup however, because the chamber was not optimized for detectors, increased noise in the output signal was an issue. This problem was compounded by the size of the chamber which limited the proximity of the gas cell used for the D-D reaction, resulting in a lower neutron flux while the activation of materials in the gas cell provided a large  $\gamma$ -ray background. Although these results could not be used to reliably estimate the behavior of the diamond at low temperatures, these experiments provided excellent insight into the operation of a diamond detector in a mix radiation field.

## 7 DETECTOR PERFORMANCE EVALUATION

The focus of this work is on evaluating the performance of a diamond detector from room temperature down to cryogenic temperature, as well as investigating discrimination methods for the separation of neutron events from  $\gamma$ -rays by employing signal processing techniques. As described in the section above, two signal acquisition chains were used to acquire data during the experiments, the first to evaluate the detector performance based on the CCE while the latter for building up a database of pulses for assessing different discrimination algorithms. Each of these objectives required unique data processing and analysis approaches which will be described in more detail in sections 7.1 and 7.3 of this chapter, respectively. These sections are followed by the discussion and interpretation of the obtained results from the data.

First the performance of the detector will be analyzed based on the evaluation of the CCE from room temperature down to 46 K. Parameters affecting the performance of the detector will be identified. The implications of these results will then be discussed in the context of operating such a detector as a  $\mu$ LoM at cryogenic temperatures. This will be followed by the analysis of the TCT datasets collected during the measurement. In section 7.4, the TCT signals will be compared with theoretically expected pulse shapes and deviations will be analyzed. From this analysis, the effects of noise on the signal shape will be identified as well as strategies to mitigate it. Based on the categorized signal shapes, the development of two PSD algorithms will be presented in section 7.5. The performance of these algorithms will be evaluated at different temperatures and compared to PSD algorithms found in literature and presented in section 5.3.

### 7.1 Charge Collection Efficiency

To evaluate the CCE dependence on temperature, the temperature data was combined with the evaluated pulse height of each event for each temperature setpoint to construct energy histograms as illustrated in Figure 7.1 for a carbon beam.

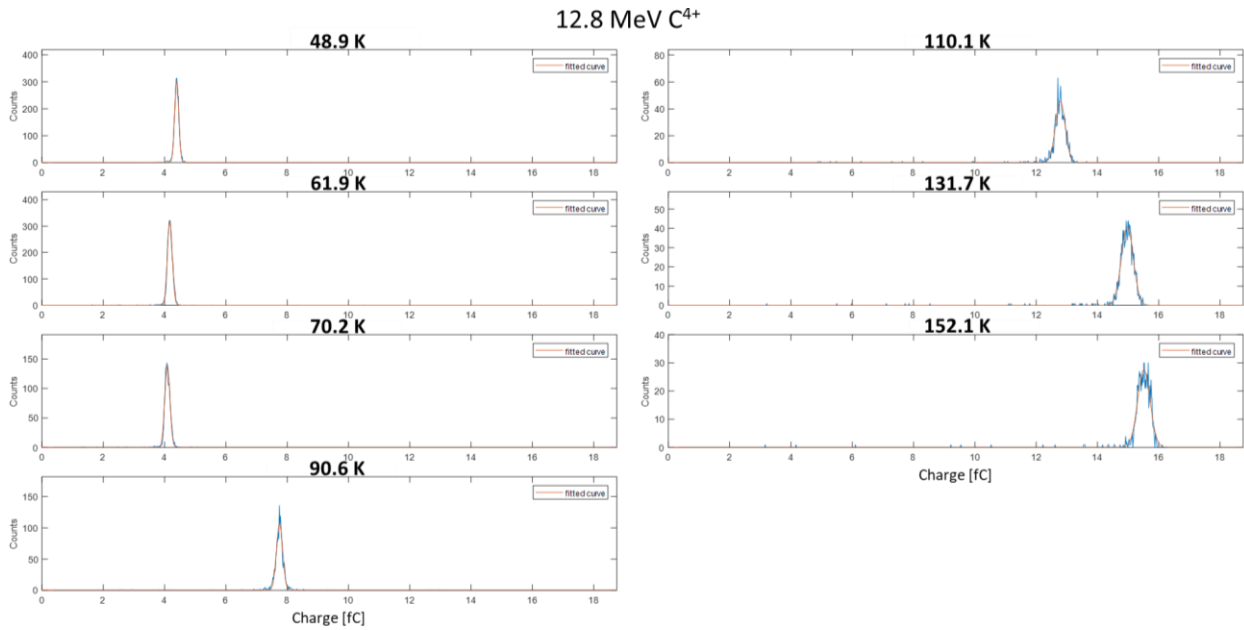


Figure 7.1 - Pulse height histograms obtained with a 12.8 MeV  $C^{4+}$  ion beam at 50 K, 60 K, 90 K, 110 K, 130 K, and 150 K [94].

From the figure above, it can be observed that at 152 K the diamond detector collected approximately 15.1 fC of charge for the 12.8 MeV carbon ion which is approximately equal to the theoretically expected value of 15.5 fC. However, at 49 K, the amount of charge collected by the detector falls to 4.4 fC or 29 % of the room temperature value. Although the number of e-h pairs generated is constant in all histograms, the number of e-h pairs detected has decreased at low temperature. For each temperature point, the centroid and the FWHM of the histogram peak were determined by a Gaussian fit. These extracted values are plotted in Figure 7.2.

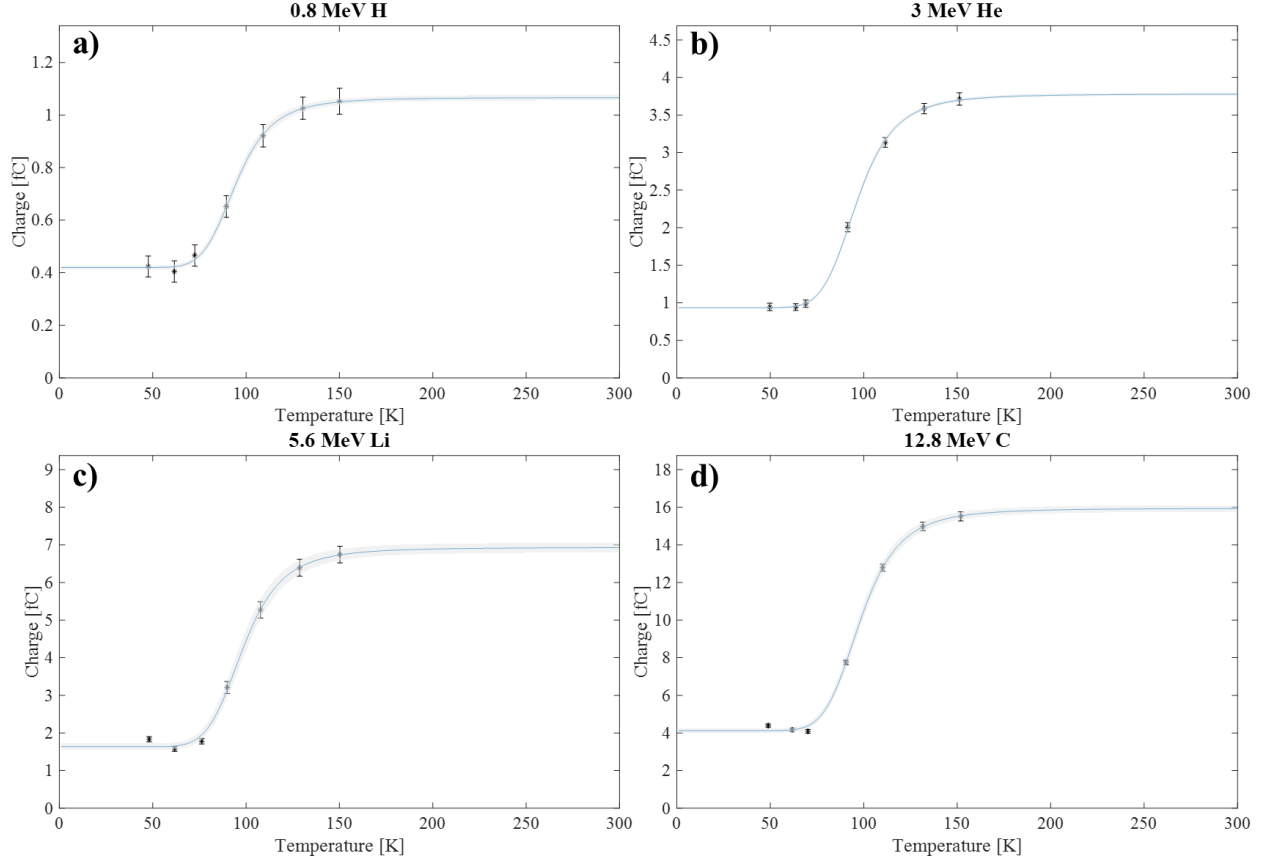


Figure 7.2 - Histogram peak centroid position plotted with temperature for a) 0.8 MeV  $H^+$ , b) 3 MeV  $He^{2+}$ , c) 5.6 MeV  $Li^{2+}$  and d) 12.8 MeV  $C^{4+}$  ion beams [94].

As described in section 3.4, this behavior has been observed by Jansen [31] for alpha particles. Jansen developed a model based on the recombination/evaporation of excitons which can be expressed by the following equation:

$$f_Q(T) = Q_{out} + \frac{Q_{tot} - Q_{out}}{1 + \epsilon \cdot e^{\frac{E_x}{k_B T}}} \quad (7.1)$$

where  $Q_{tot}$  is the total generated charge,  $Q_{out}$  the charge present in the outer volume of the generated charge cloud,  $E_x$  is the exciton binding energy of 80 meV in diamond,  $\epsilon$  represents the ratio of the exciton formation time to the exciton recombination time,  $k_B$  is the Boltzmann constant and  $T$  is the temperature.  $Q_{out}$  represents the charge collected when the CCE is at the lowest value which is at the lowest temperature, while  $Q_{tot}$  represents the charge collected when the CCE is at the highest

value and at the highest temperature. This model was used to fit the extracted histogram centroid position with respect to temperature, as presented in Figure 7.2 by a blue line. The grey region behind the blue line in the same figure represents the uncertainty in the fit. This fit was performed to aid in the comparison between various ion and bias measurements which will be presented in the following section. Here the data analysis process was outlined for the experiment performed with a carbon beam, but the same procedure was applied to all data acquired from experiments with monoenergetic ions.

Contrary to ion induced detection which results in a clearly defined single peak in the energy spectrum, neutron and  $\gamma$ -ray interactions with the diamond crystal result in more complicated pulse height spectra due to the possibility of multiple reactions with the carbon atoms/nuclei. This results in an energy spectrum which is a superposition of all the various interactions as shown by simulations in Figure 6.14 and Figure 6.15. These simulations show a fairly good agreement with the experimental spectra and enable the identification of all the spectra features. For CCE evaluation the clear peak at 8.3 MeV (Figure 7.4a) corresponding to the kinetic energy of the products of the  $^{12}\text{C}(n,\alpha)^9\text{Be}$  reaction was selected since it is well defined and separated from the  $^{12}\text{C}(n,n+2\alpha)$  continuum.

Concerning the  $\gamma$ -ray detection, as was expected, the 440 keV  $\gamma$ -ray does not result in a full energy peak but the spectrum consists of a 280 keV peak (Figure 7.4b) resulting from the 440 keV Compton edge superimposed on a continuum from the 1634 keV  $\gamma$ -ray. For this case, an exponential function was used to subtract this background from the spectrum and the Compton edge was fitted by means of the HDTV Nuclear Spectrum Analysis [106] software using a Gaussian fit with the left tail as a free parameter. As described in section 6.5, Geant4 simulation were performed during the design of the experiment. The simulation for 440 keV  $\gamma$ -rays, where the Compton edge is visible, was used to find the Gaussian function that fits the data properly (Figure 7.3a). The insert in this figure is a zoom to the region of interest where the Compton edge is located between 0.2 MeV to 0.35 MeV with the fit function illustrated by the red line. While the simulation of the 1634 keV  $\gamma$ -ray was used to find the correct exponential function for the background (Figure 7.3b). These two functions that were obtained from fitting the simulations were then combined to fit the experimental data in order to isolate the Compton edge with confidence (Figure 7.3c).



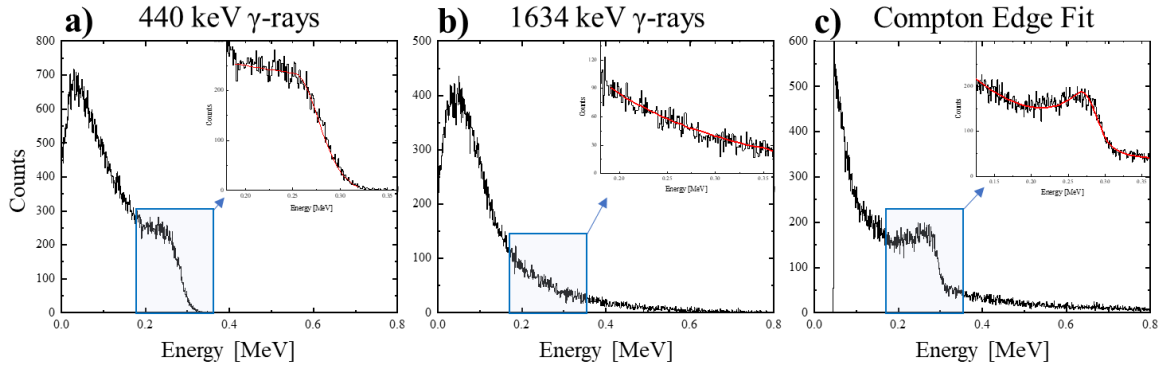


Figure 7.3 - Fitting the Compton edge in the experimental data obtained during the experiments with  $\gamma$ -rays. Plots a) and b) illustrate the simulated spectra for 440 keV and 1634 keV  $\gamma$ -rays overlaid with the fit functions used in the inlayed subplot, respectively. Plot c) illustrates the experimental spectrum with the cumulative fit function used in the inlayed subplot.

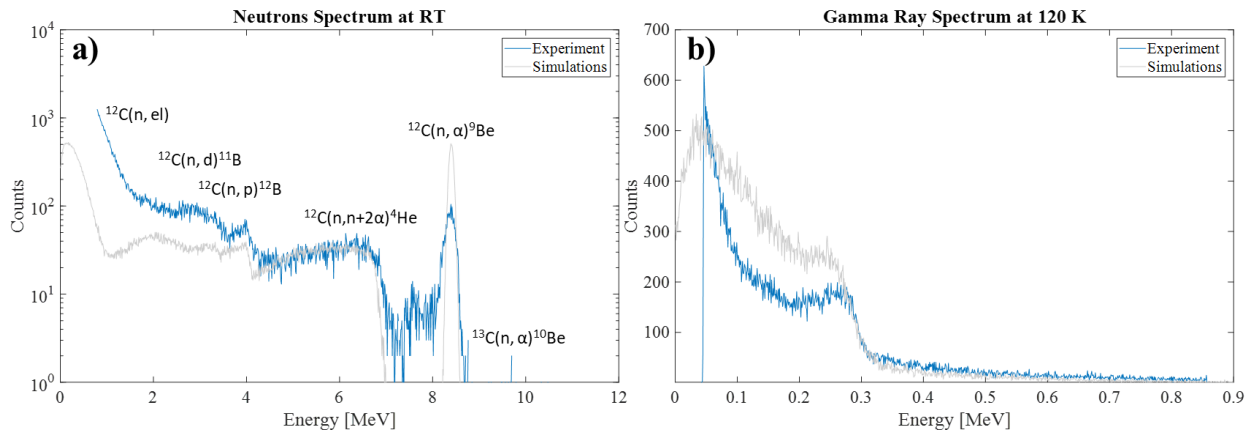


Figure 7.4 - Acquired spectra (blue) overlapped with simulated (grey) spectra. For a) 14.1 MeV neutrons and b)  $^{23}\text{Na}(p,p'\gamma)$   $\gamma$ -rays [95].

As the temperature decreases, the CCE, that is, the amount of charge collected by the diamond detector, decreases. Since less charge is being collected, the amplitude of the signal decreases, resulting in a shift of all the features of the corresponding pulse height spectrum towards lower amplitudes. Furthermore, since the noise amplitude remains the same while the signal amplitude decreases, the SNR decreases resulting in a decrease in the relative energy resolution. This can be observed in Figure 7.5 when comparing the spectra acquired at different temperatures. Figure 7.5a contains the spectra acquired for neutrons, while Figure 7.5b for  $\gamma$ -rays, respectively.



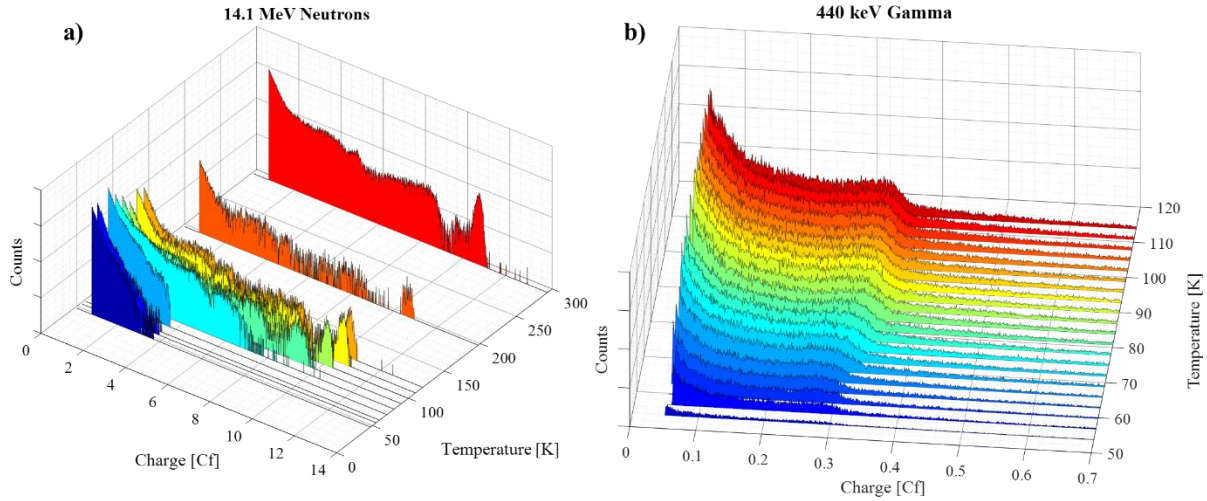


Figure 7.5 - Acquired pulse height spectra at each temperature setpoint for a) neutrons and b)  $^{23}\text{Na}(p,p'\gamma)$   $\gamma$ -rays [95].

From Figure 7.5a, it can be noted that the distinct  $^{12}\text{C}(n,\alpha)^9\text{Be}$  reaction peak is not observed below 70 K and therefore was not further analyzed below this temperature. The fitted centroid position of this reaction is plotted against temperature in Figure 7.6a. Furthermore, it can be observed from Figure 7.5b that the spectra for  $\gamma$ -rays change much less over the same temperature range in comparison to the neutron spectra. However, a shift towards lower CCE is still observed as is illustrated by plotting the 440 keV  $\gamma$ -ray Compton edge centroid position with temperature in Figure 7.6b.

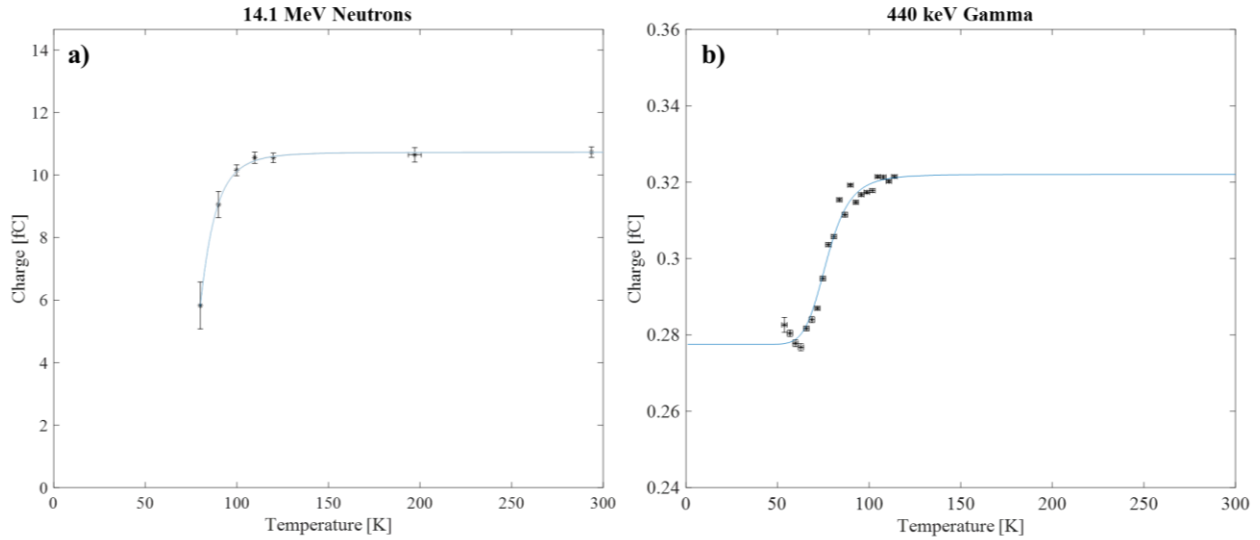


Figure 7.6 - Fitted centroid position for a)  $^{12}\text{C}(n,\alpha)^9\text{Be}$  reaction and b) 440 keV  $\gamma$ -ray Compton edge [95].

## 7.2 Detector Performance

A drop in the CCE for diamond detectors was observed previously for alpha particles [31], however this is the first published observation of low temperature operation for any other type of directly or indirectly ionizing and nonionizing radiation [94], [95]. To better understand the mechanism behind this CCE drop, experimental measurements of the CCE at low temperatures were performed for different ions spanning in masses from light protons to heavier carbon ions, as well as for photons and neutrons. From Figure 7.2 and Figure 7.6, a drop in CCE can be observed for all measured types of radiation, however the critical temperature where this drop begins as well as the magnitude of the CCE decrease varies. These results are combined and summarized in Figure 7.7 and Table 7.1.

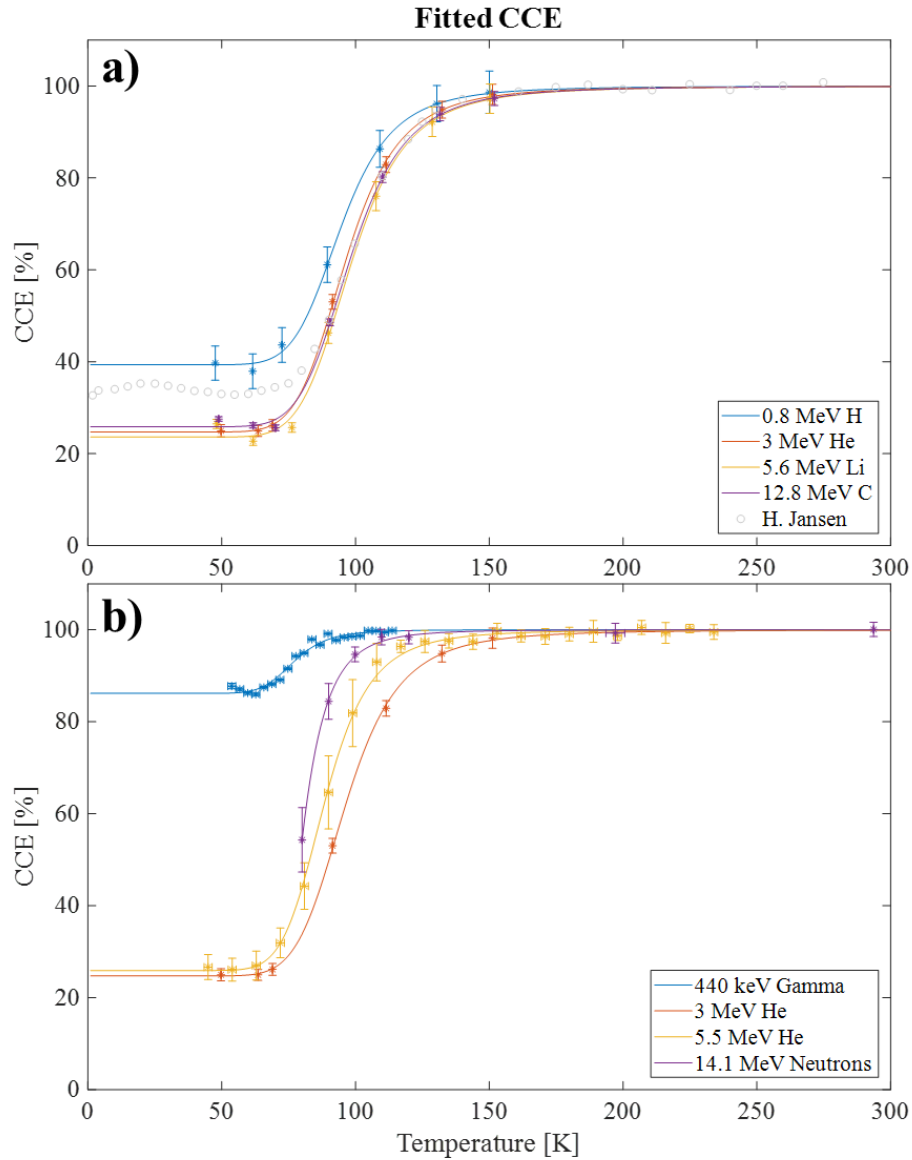


Figure 7.7 - CCE vs Temperature for a) ions b)  $\gamma$ -rays and neutrons. The data for 3 MeV He ion is added to both plots for comparison purposes.

Table 7.1 - Summary of CCE drop per impeding particle. For neutrons, the CCE value at 80 K is given since the evaluation of the CCE was not possible below this temperature.

Impeding Particle	Energy [MeV]	CCE Decrease [%]		
		Detector Bias		
		1 V/ $\mu\text{m}$ (300 V)	1.17 V/ $\mu\text{m}$ (350 V)	1.33 V/ $\mu\text{m}$ (400 V)
H	0.8	$60.7 \pm 0.8$	$59.2 \pm 0.8$	$57.6 \pm 0.8$
He	3	$75.3 \pm 0.4$	$73.5 \pm 0.5$	$71.5 \pm 0.7$

Li	5.6	$76.4 \pm 1.3$	$75.3 \pm 1.2$	$73.9 \pm 1.1$
C	12.8	$74.1 \pm 0.8$	$72.5 \pm 0.9$	$71.0 \pm 0.7$
$\gamma$ -rays	0.44	$13.8 \pm 0.5$	-	-
Neutrons	14.1	$(54 \pm 7 @ 80 K)$	-	-

Experimental data clearly shows that the decrease of the CCE with temperature follows a similar trend for each type of radiation. A plateau at 100 % CCE is observed from RT down to approximately 145 K. This is followed by a rapid decrease in the CCE between  $65 \text{ K} < T < 145 \text{ K}$ . Below 65 K, the CCE stabilizes again to the minimum measured temperature of 46 K. For He, Li and C ions, the relative CCE decreases by a similar magnitude to  $24.7 \pm 0.4 \%$ ,  $23.6 \pm 1.3 \%$ ,  $25.9 \pm 0.8 \%$  respectively. For protons, the relative CCE decreases to  $39.3 \pm 0.8 \%$ , which is significantly less than for the heavier ions. While for  $\gamma$ -rays the CCE decreases only to  $86.2 \pm 0.5 \%$  of the RT value.

Such differences are in agreement with the previous work performed by Jansen et al. [45], in which they are attributed to the screening of the externally applied electric field by the outer region of the generated charge cloud from the inner charge carriers. The lower electric field strengths seen by the inner volume of charge carriers leads to slower charge separation and therefore increases the probability of exciton formation. The charge carriers which enter an exciton state do not drift and consequently do not contribute to the induced current in the detector electrodes. Since the penetration depth of all ions used in the experiment was fixed to  $5.6 \mu\text{m}$ , only the density of the generated charge cloud varied. As the proton beam produced 16 times less charge carriers than the carbon beam in approximately the same volume, the electric field screening is weaker which leads to the formation of less excitons and therefore more charge carriers to drift and contribute to the overall induced current in the electrodes. This results in the CCE for a proton beam decreasing less than for a carbon beam at lower temperature, which is observed in Figure 7.7a. Furthermore, the density of the generated charge cloud created by the interaction of a  $\gamma$ -ray is still lower, resulting in even less excitons and therefore a smaller decrease in the CCE as observed in Figure 7.7b. On the other hand, the difference in the CCE drop for He, Li and C beams is insignificant even though the carbon beam creates 4.3 times (Table 6.1) more charge carries than the helium beam. This implies that there is a threshold density of the generated charge cloud after which almost all e-h pairs created in the inner volume enter into an exciton state.

However, by observing the ionization profile of each ion as they transverse the diamond lattice (presented in Figure 6.12), the generated charge cloud density is not evenly distributed throughout the ion range but is increasing to a maximum at the Bragg peak. A big difference is observed when comparing the portion of the ionization profile before the Bragg peak for a H beam to the He, Li and C beams. The density of the charge cloud before the Bragg peak is much lower for an H beam and therefore a greater portion of charge carriers from this region contribute to the overall induced current. This also explains the shift in the critical temperature where the CCE begins to decrease as observed for the same impinging ion at different energies and presented in Figure 7.7b. Specifically, experiments performed with a 3 MeV helium ion beam (red), a  $^{241}\text{Am}$  source producing 5.5 MeV  $\alpha$  particles (yellow) and neutron (purple). The  $^{12}\text{C}(n,\alpha)^9\text{Be}$  reaction with neutrons is the result of a superposition of  $\alpha$  particles with beryllium ions at an average energy of 8.3 MeV depending on the kinematics of the reaction. From the results of these three measurements, it is observed that the critical temperature where the CCE begins to drop shifts towards lower temperatures as the ion energy increases.

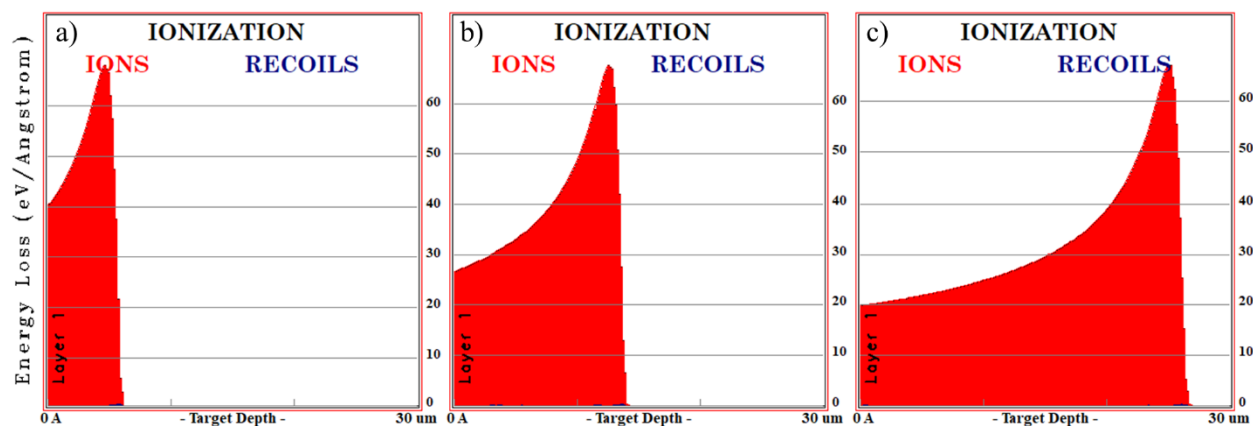


Figure 7.8 - Ionization profile of impinging  $\alpha$  particles at a) 3 MeV b) 5.5 MeV and c) 8.3 MeV.

The penetrating depth of an ion is proportional to its energy, the higher the energy of the impinging ion, the deeper the Bragg peak will be. As illustrated in Figure 7.8, the higher the energy of the ion, the greater the portion of charge carriers generated at lower density before the Bragg peak. As discussed earlier, since the density is directly proportional to the formation of excitons, the deeper the ion penetrates, the more charge carriers contribute to the induced current effectively shifting the CCE vs temperature curve to lower temperatures. However, the amount of charge

deposited before the Bragg peak is relatively small which in term has a limited effect of the CCE shift. The difference in energy between the three  $\alpha$  experiments are 2.5 MeV and 2.8 MeV respectively resulting in an approximate shift of 4.3 K/MeV. In the case of small energy differences, as those found in a triple alpha source consisting of  $^{239}\text{Pu}$ ,  $^{241}\text{Am}$  and  $^{244}\text{Cm}$ , with  $\alpha$  energies at 5.1 MeV, 5.5 MeV and 5.8 MeV respectively, the shift is not observed within uncertainty due to the resolution of the detector. The energy spectra collected by the detector from the triple alpha source with three distinctive peaks at RT is illustrated in Figure 7.9 from RT down to 46 K.

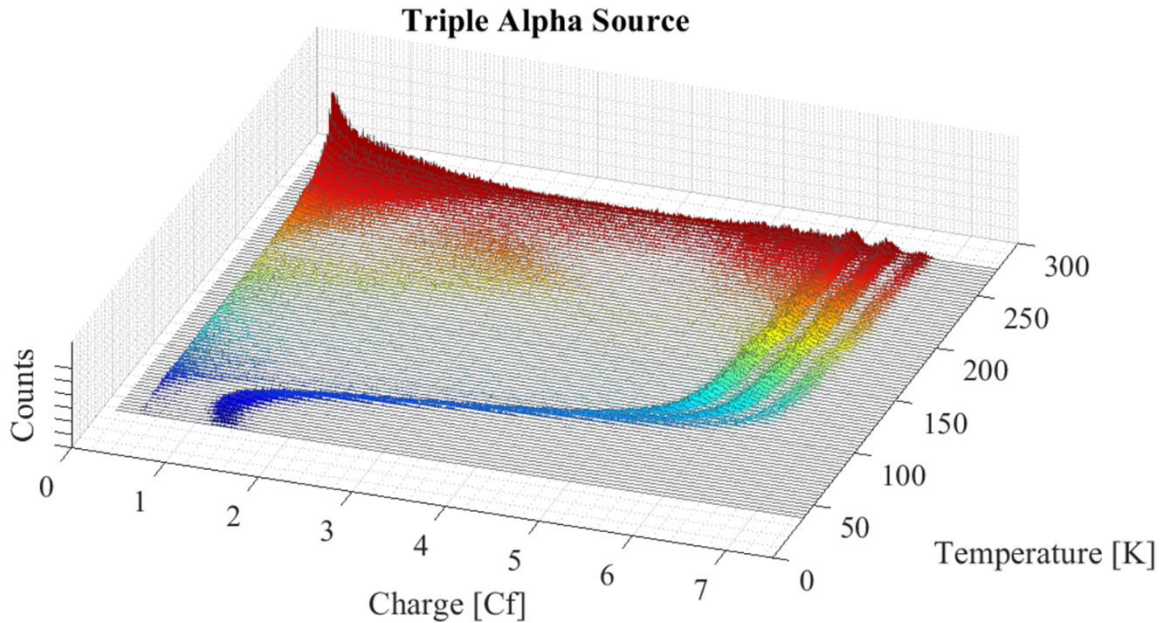


Figure 7.9 - Energy spectra collected from a triple alpha source from RT down to 46 K [95].

The 3D plot above, Figure 7.9, consisting of a collection of 2D energy spectra obtained at various temperatures nicely summaries the effects of the CCE decrease on a signal obtained from a diamond detector. At higher temperatures where the CCE is 100 %, the  $\alpha$  particles emitted by the isotopes at three different energies are easily distinguishable. However, at the critical temperature around 140 K, the three distinctive peaks start to merge into one and are completely indistinguishable below 100 K. This makes the diamond detector unsuitable for spectroscopic use at cryogenic temperature however it can still be used as a counter since all the impinging ions are still detected. It has to be notes that even though the detector can be used as a counter at cryogenic temperature, discrimination based on particle energy is not possible since all the signals merge into

the one. Therefore, other methods for discrimination have to be implemented and are explored in the next section of this work.

Furthermore, although there is a large uncertainty in the final CCE point at 80 K for neutrons, the slope of the CCE fit function is different from the other experiments with  $\alpha$  particles. This difference in the slope could be the result of the kinematics of the  $^{12}\text{C}(n,\alpha)^9\text{Be}$  reaction. The  $\alpha$  particle and beryllium ion can be ejected in any direction and therefore their trajectories are not always perpendicular to the electrodes in the co-planer design of the detector. Thus, the charge cloud orientation in reference to the electric field varies, impacting the separation of the charge carriers. This will affect the creation of excitons and therefore the CCE.

Since the formation of excitons is directly related to the electric field, varying the electric field strength should also influence the drop in the CCE at cryogenic temperatures and possibly provide a mechanism to recover the CCE. This effect was investigated with ions where the bias voltage was change from 1 V/ $\mu\text{m}$  to 1.33 V/ $\mu\text{m}$ . Although an increase of 0.33 V/ $\mu\text{m}$  is relatively small, a larger increase was not possible to due to the voltage limitations of the CIVIDEC amplifier and the thickness of the scCVD diamond.

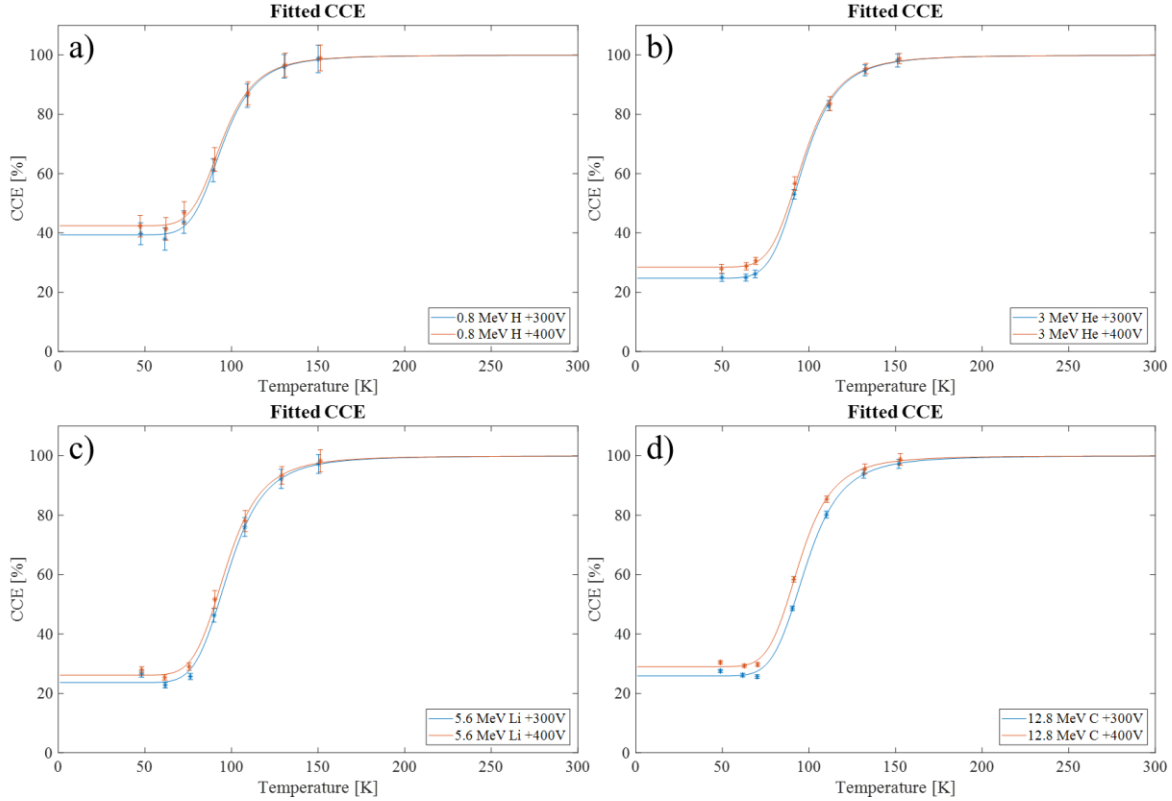


Figure 7.10 - Influence of the detector bias voltage change from 1 V/μm to 1.33 V/μm on the CCE for ions a) H, b) He, c) Li and d) C.

As depicted in Figure 7.10, the CCE at cryogenic temperatures increased by  $3.1 \pm 1.6 \%$ ,  $2.8 \pm 1.1 \%$ ,  $2.5 \pm 2.4 \%$  and  $3.1 \pm 1.5 \%$  for H, He, Li and C ions, respectively. Even with a small increase in the bias voltage of 0.33 V/μm, a significant increase in the CCE at cryogenic temperatures was clearly observed. Diamond has a large dielectric constant (Table 3.1) which allows for very high bias voltages. Further work is required to fully investigate the effects of bias voltage on the CCE at cryogenic temperatures, but the initial results are positive, and it has the potential to make a diamond-based detector a more effective μLoM.

### 7.3 Transient Current Technique

As described in section 5.3, the type of radiation detected by a diamond detector can be in principle determined on the basis of transient current profile induced at the electrodes by the drift of the generated charge carriers inside the diamond crystal. However, these current pulses are very small, superimposed with noise and require a large amplification before discrimination techniques



can be applied to them. Since only a wideband amplifier is used before the digitization of the transient current pulses, the amplified is acquired along with all the noise by the fast oscilloscope. Digital signal processing techniques must be applied to this signal before further analysis can be performed. Figure 7.11 illustrates an example of digitized signal in the time (Figure 7.11a) and frequency (Figure 7.11b) domain. As described in section 6.4, the noise from the ion source plasma oscillator is superimposed in the signal and its frequency of approximately 100 MHz is clearly visible in the frequency spectrum.

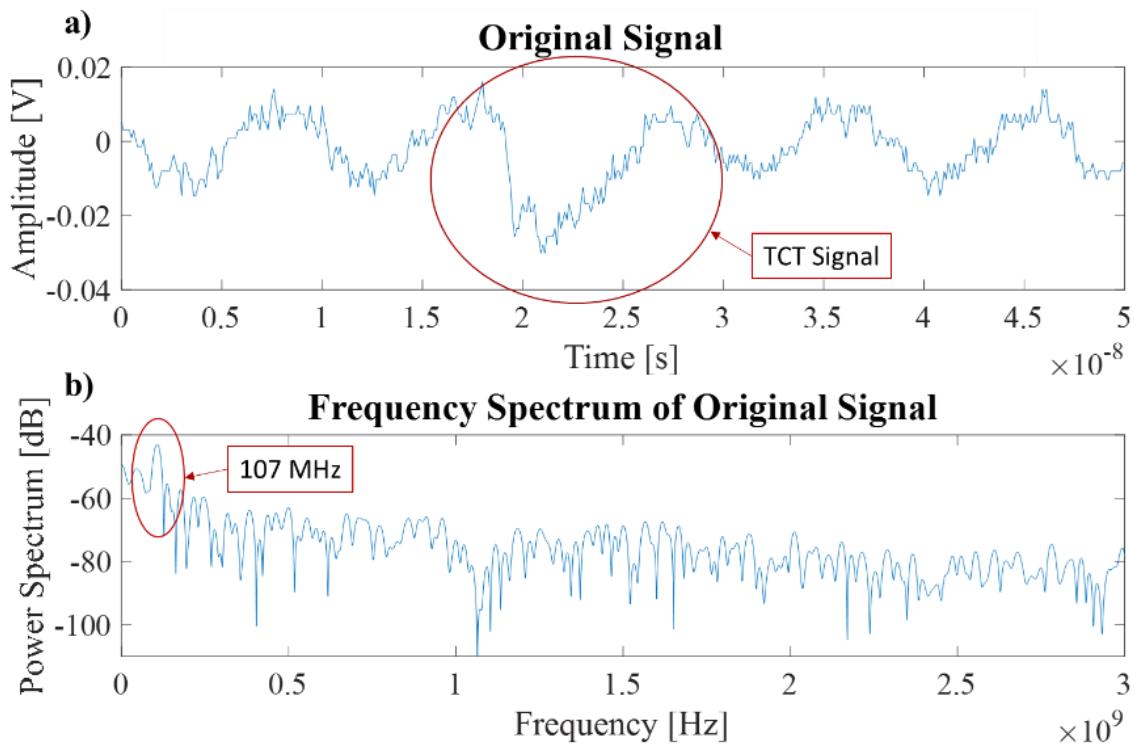


Figure 7.11 - Acquired TCT signal in a) time domain and b) frequency domain before signal processing. The TCT signal is highlighted along with the frequency of the superimposed noise at 107 MHz.

A 2<sup>nd</sup> order IIR Butterworth notch filter with a passband centered at 112 MHz and a width of 30 MHz was used to remove this sinusoidal noise (Figure 7.13a) while a 8<sup>th</sup> order IIR Chebyshev type I lowpass filter with a cutoff frequency of 2 GHz was used to further process the signal since the bandwidth of the preamplifier was 2 GHz (Figure 7.13b). The aforementioned filter parameters were experimentally determined to be the optimum through many iterations. A higher order lowpass filter was chosen due to the superior performance regarding stopband and passband ripples

and sharper cutoff edges at the cost of processing power and computing speed since the data was being analyzed offline.

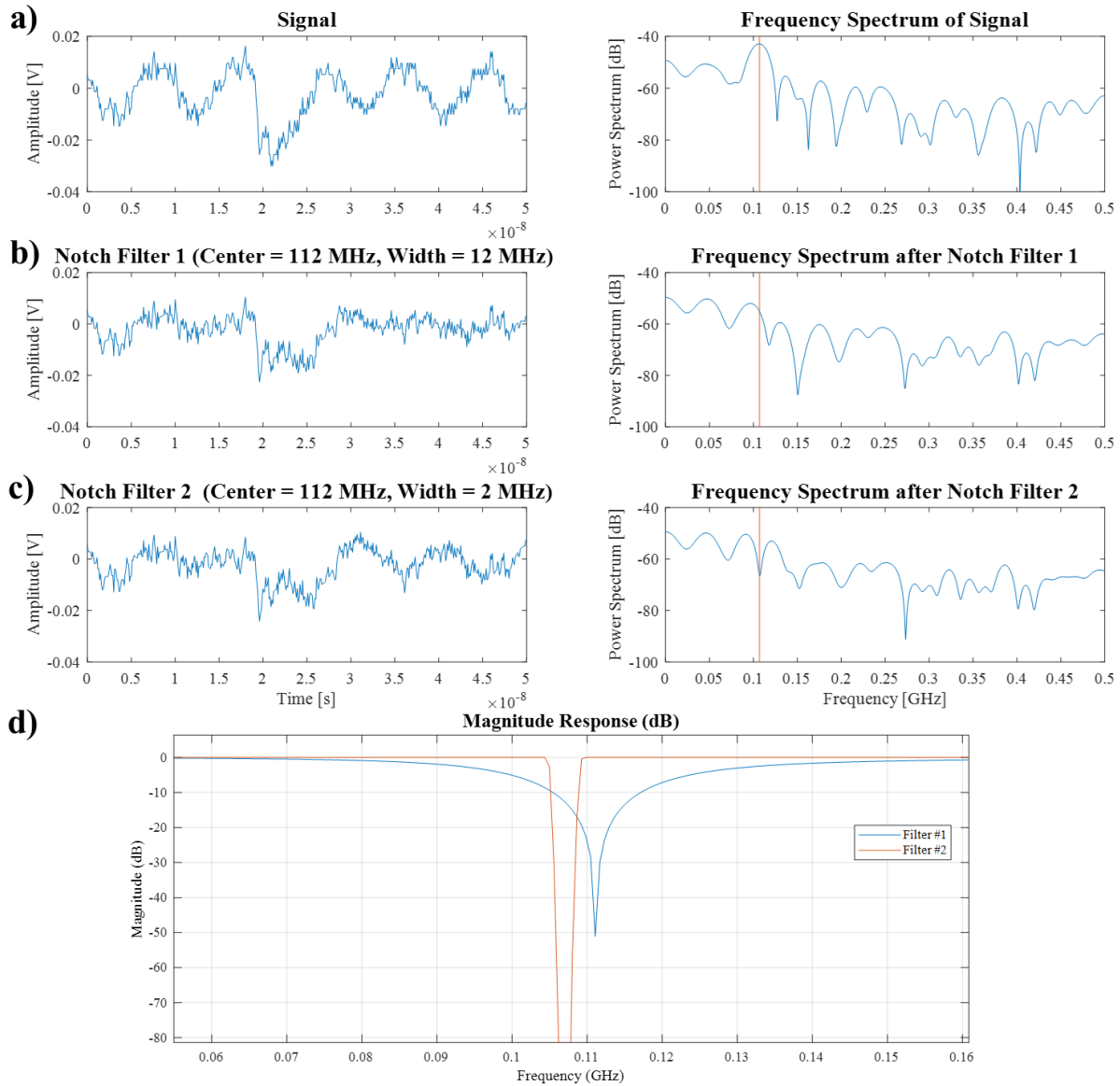


Figure 7.12 - Impact on the signal for various notch filter parameters. a) Original signal with the frequency spectrum marked with a vertical red line at the maximum value of 107 MHz. b) 2<sup>nd</sup> order notch filter centered at 112 MHz with a width of 12 MHz c) 20<sup>th</sup> order notch filter centered at 107 MHz with a width of 2 MHz. d) Magnitude response of each filter, lower order in blue (filter #1) and the higher order in red (filter #2).

The design of the notch filter was crucial as it had a significant effect of the signal shape, while the lowpass filter cutoff frequency was higher than the preamplifier bandwidth and therefore above the signal frequency and impacted the signal shape less. The design of the notch filter was based

on the frequency spectrum of the signal. A significant noise contribution can be seen at 107 MHz (indicated by a red line in the right plot of Figure 7.12a). The noise superimposed on the signal is sinusoidal, therefore the optimal filter center frequency and stopband width were obtained through an iterative process by evaluating the RMS value of the noise at the filter output. Table 7.2 summarizes a subset of the most promising parameter combination for the filter design.

Table 7.2 - Noise RMS values for different filter parameters. The parameters corresponding to the highlighted values were further evaluated on various signal shapes.

Center [MHz]	Width [MHz]	Filter Order									
		2	4	6	8	10	12	14	16	18	20
107	2	0.0057	0.0052	0.0048	0.0046	0.0045	0.0045	0.0045	0.0045	0.0045	0.0045
	12	0.0040	0.0038	0.0037	0.0037	0.0040	0.0041	0.0041	0.0040	0.0039	0.0039
112	2	0.0059	0.0055	0.0051	0.0049	0.0048	0.0048	0.0047	0.0047	0.0046	0.0046
	12	0.0040	0.0037	0.0037	0.0039	0.0041	0.0042	0.0041	0.0040	0.0039	0.0039

Smaller values in Table 7.2 indicate better attenuation of the sinusoidal noise, however the pulses being analyzed also contain components in the same frequency range. Completely eliminating the frequency of the noise alters the pulse shape leading to the loss of information regarding the type of impinging radiation. This is illustrated in Figure 7.12c with a 20<sup>th</sup> order notch filter centered at 107 MHz and with a stopband width of 2 MHz, which should be ideal for removing the superimposed noise. A balance between the attenuation of this noise and the preservation of the pulse shape was required. The cells highlighted in Table 7.2 present the best RMS values obtained with the given filter parameters. The filter output pulse achieved with these parameters were further analyzed based on the pulse shape in order to produce the optimal filter.

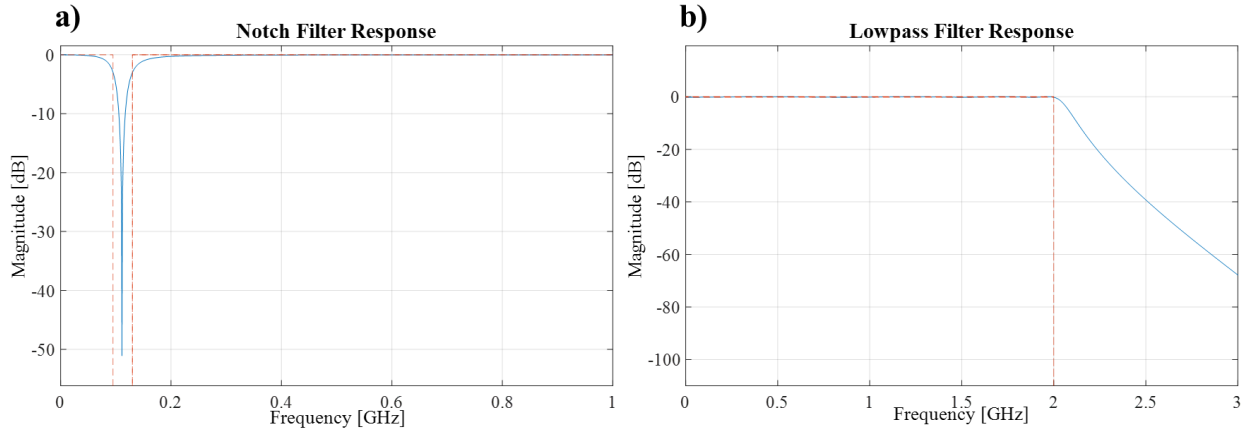


Figure 7.13 - Implemented digital filter magnitude response for a) Notch Filter and b) Lowpass Filter.

The Figure 7.14 below illustrates the signal after each filter stage and the final signal, which will be used for discrimination presented in Figure 7.14b. Comparing the time domain plots of Figure 7.11 and Figure 7.14b, the large influence of the noise on the signal shape can be observed. Further emphasizing that noise minimization as well as the choice of the correct filters are crucial for particle identification using the PSD technique.

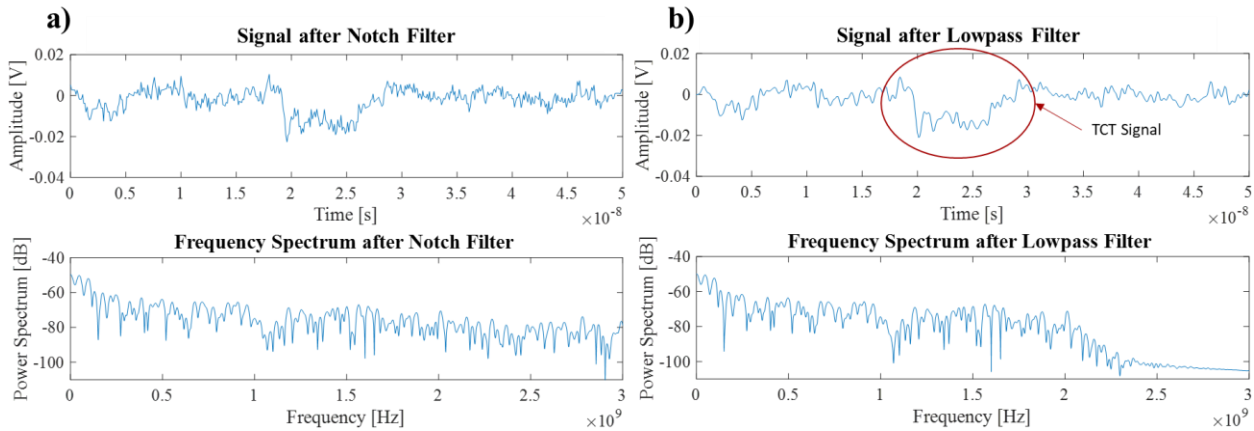


Figure 7.14 - Signal after a) Notch filter and b) Lowpass filter presented in both the time (top) and frequency (bottom) domain.

Each type of radiation interacts distinctively with the diamond detector, and this results in differences in the obtained TCT pulse shapes. Fast ions generate most charge carriers (electron-hole pairs) in a relatively small, localized part of the detector, following the steep energy loss at the Bragg peak. In a co-planar detector design, as presented earlier in Figure 6.5, this interaction

occurs close to one electrode, i.e., at a depth of  $11.8 \pm 0.1 \mu\text{m}$  for 5 MeV alpha particles. As the produced charge carriers start to drift towards their respective electrodes under the influence of the externally applied electric field at the same time, a sudden large current is induced in the electrode which remains constant until all the charges stop moving, that is, when they arrive at the electrode. This produces a square TCT pulse shape as was observed during measurement with ions and presented in Figure 7.15a. On the contrary,  $\gamma$ -ray interactions, dominated by Compton scattering, result in an even distribution of generated charge carriers throughout the whole thickness of the detector. As in the case with ions, these charge carriers begin to drift at the same time. However, due to their distribution throughout the detector, they will arrive at the electrode at different times. In an ideal case, the current induced in the electrode will linearly decrease with time until all the charge carriers are collected, resulting in a triangular TCT signal as was observed with 440 keV  $\gamma$ -rays and presented in Figure 7.15b.

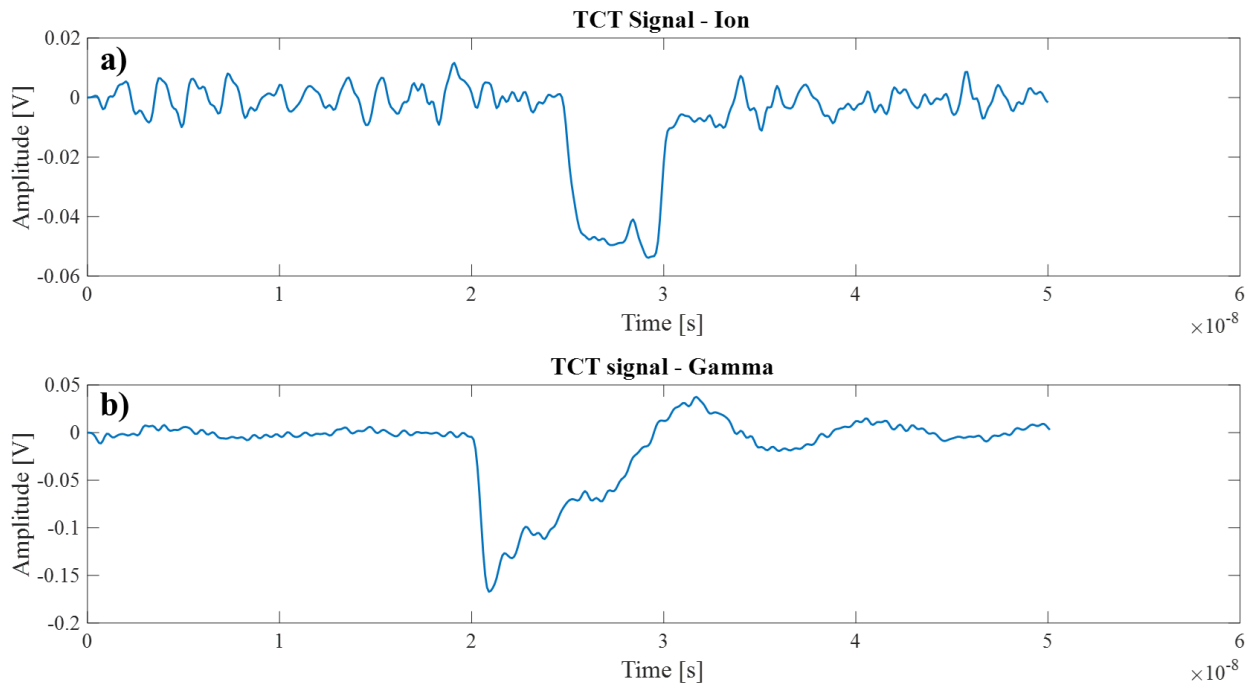


Figure 7.15 - TCT signals acquired from a) 12.8 MeV C beam and b) 440 keV  $\gamma$ -rays.

TCT signals generated by neutrons are more complex since nuclear reactions can occur at any location inside the volume of the detector. This results in a pulse shape that is a superposition of the current induced by the drift of electrons and holes to their respective electrodes. If the nuclear

reaction occurs close to the detector electrodes or in the ballistic center of the detector, an ion like square TCT signal shape is generated. While between these regions, a multi-step shape is generated consisting of a higher amplitude region where both charge carriers are in motion followed by a lower amplitude region where only one charge carrier is in motion. This signal shape acquired during the experiment is presented in Figure 7.16. The same figure additionally illustrates how the same signal shape looks during measurements at higher temperatures of 120 K (Figure 7.16a) and lower temperatures of 55 K (Figure 7.16b). The most notable difference between the two plots being the lower SNR of the TCT trace acquired at 55 K which is the result of the lower CCE.

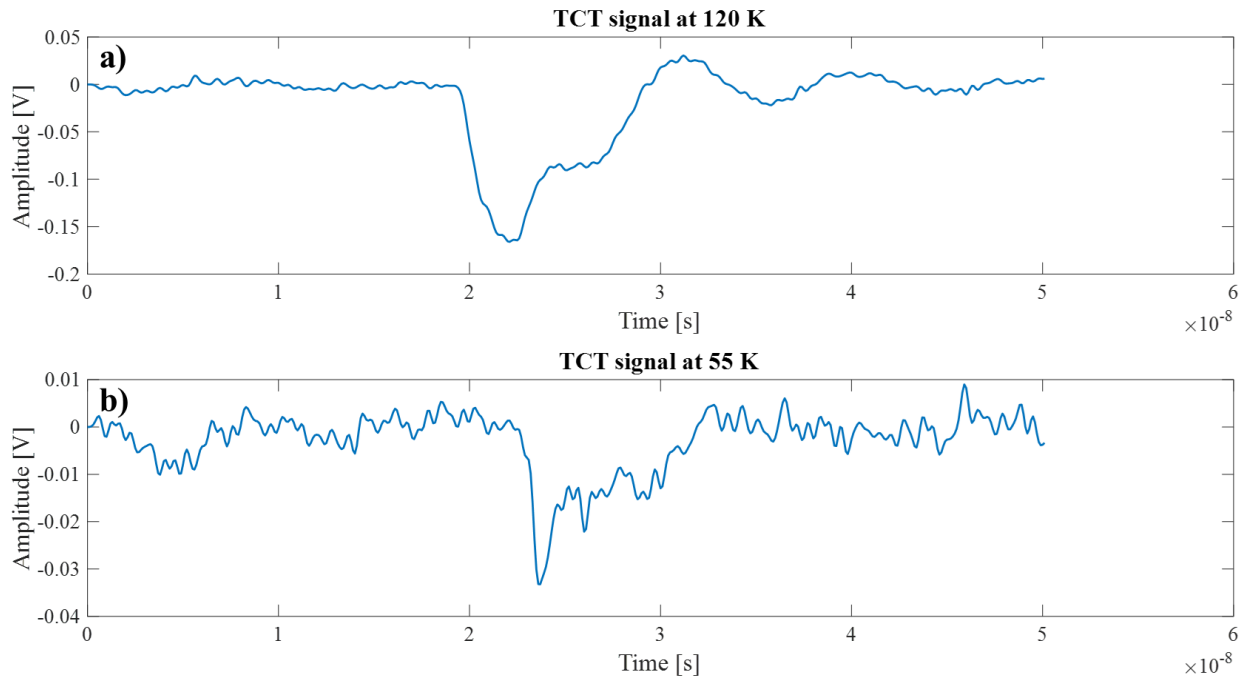


Figure 7.16 - TCT signals acquired by neutrons at a) 120 K and b) 55 K.

## 7.4 Signal Benchmarking

As was discussed in the previous sections, TCT datasets were obtained with each experiment for the purpose of applying pulse shape analysis techniques for neutron/ $\gamma$ -ray discrimination since discrimination based only on the total amount of charge collected (pulse height discrimination) is not possible at low temperatures. At each temperature setpoint approximately 3,000 TCT traces were collected. Each dataset was processed as described in section 7.3. However, to decrease the statistical uncertainty while keeping within the experiment time constraints, for temperature setpoints of 55 K and 120 K more than 10,000 TCT traces were collected, and these datasets were used for signal benchmarking and PSD algorithm development. Due to the large quantity of data, data mining techniques were employed to organize and filter the data using the Orange: Data Mining software package (v3.34) [107].

The TCT datasets obtained for ions and  $\gamma$ -rays are more straight forward to interpret due to the higher SNR and a single interaction occurring with the diamond lattice. TCT pulse shapes acquired during experiments with neutrons are far more complex and require a more detailed analysis. During the analysis of these acquired signals, theoretically expected pulse shapes were observed, however many other signal shapes were also detected. Since these unexpected pulse shapes make up a significant percentage of the overall signals detected, they cannot be ignored while developing a PSD algorithm. Benchmarking all the acquired signals provides a better understanding of where these unexpected pulse shapes are generated, and which are the result of the superposition of noise. Focusing on the neutron TCT dataset obtained at 120 K, due to the higher SNR, the dominate signal shape along with their correlation to the energy spectrum are presented in Figure 7.17. It was found that all other signal shapes present in the dataset are superpositions of these shapes with a varying level of noise.

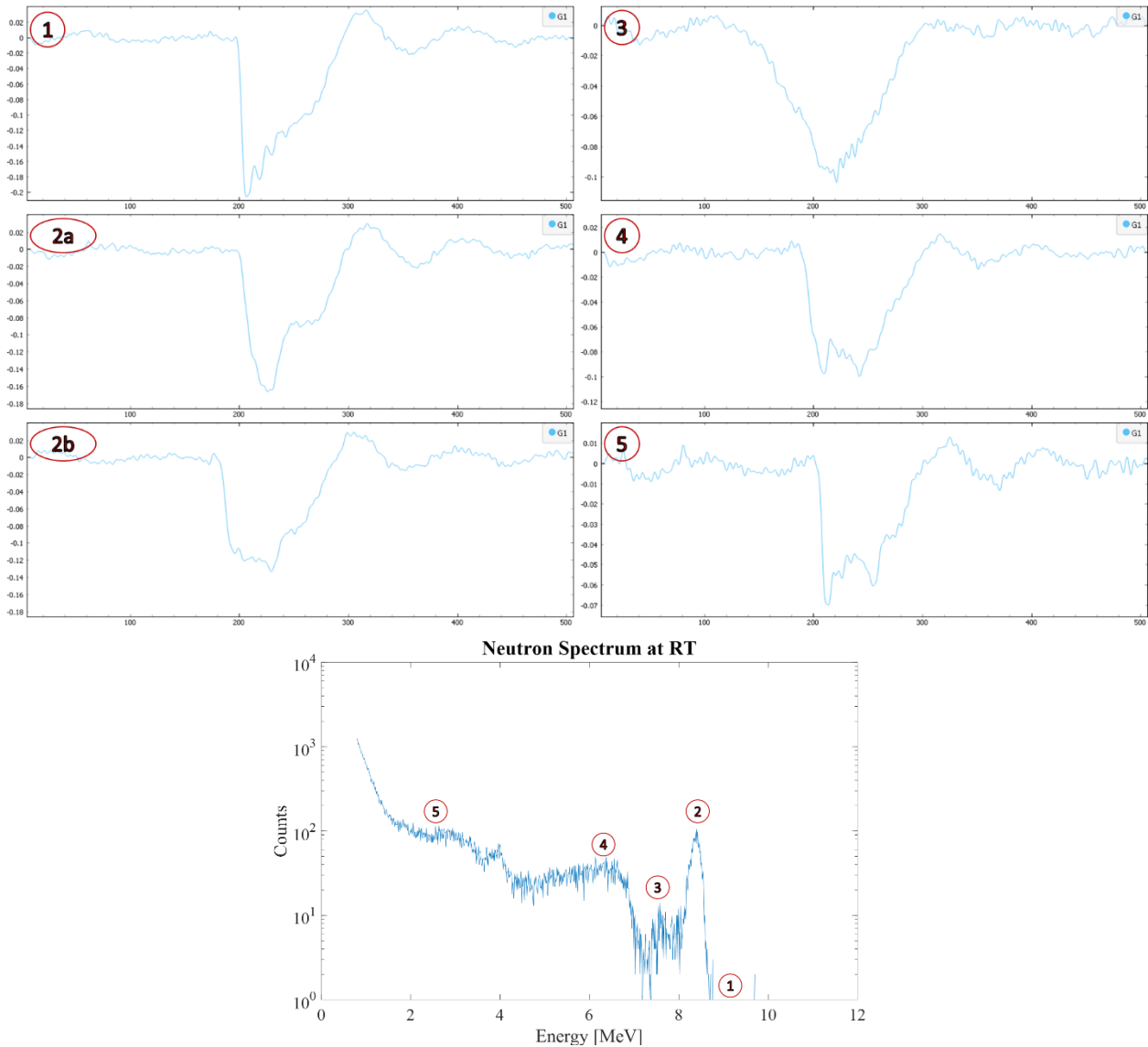


Figure 7.17 - TCT pulse shapes correlated with their position in the energy spectrum [95].

The dominant signal shapes vary depending on the position in the energy spectrum because several different reactions are possible between the neutron and the carbon atom. As depicted in Figure 7.4 the other possible reaction for the neutron energy range used in the experiment include:  $^{12}\text{C}(n,e)$ ,  $^{12}\text{C}(n,d)^{11}\text{B}$ ,  $^{12}\text{C}(n,p)^{12}\text{B}$ ,  $^{12}\text{C}(n,n+2\alpha)^4\text{He}$ ,  $^{12}\text{C}(n,\alpha)^9\text{Be}$  and  $^{13}\text{C}(n,\alpha)^{10}\text{Be}$  with Q-values: 0, -13.732, -12.587, -7.275, -5.701 and -3.835 MeV, respectively [70]. Examining the signal shapes presented in Figure 7.17 in numerical order from the higher energy part of the spectrum (left) to the lower energy part (right):



1. With 14.1 MeV neutron, the reaction with the highest Q-value is  $^{13}\text{C}(n,\alpha)^{10}\text{Be}$ . However, as  $^{13}\text{C}$  makes up about 1 % of natural carbon, so statistically this reaction is very improbable. Therefore the most probable reaction with the highest Q-value is  $^{12}\text{C}(n,\alpha)^9\text{Be}$  and above this peak at 8.3 MeV neutron TCT signals are not expected. This is confirmed in the dataset with only  $\gamma$ -ray triangular pulse shapes found above this energy.
2. The energy peak located at 8.3 MeV created by the  $^{12}\text{C}(n,\alpha)^9\text{Be}$  consists predominately of two pulse shapes, as theoretically expected. The more probable multi-step (2a) shape created by charge carriers drifting for a different amount of time to reach their respective electrodes, and the square shape (2b) resulting from charge carriers created close to the electrodes and in the ballistic center of the diamond crystal.
3. In the region between the  $^{12}\text{C}(n,n+2\alpha)^4\text{He}$  continuum and the  $^{12}\text{C}(n,\alpha)^9\text{Be}$  peak, no signals are expected. However, as observed in the histogram presented in Figure 7.17, signals were acquired in this region. The observed signal shapes suggest these are the results of the incomplete charge collection of the  $^{12}\text{C}(n,\alpha)^9\text{Be}$  reaction. Incomplete charge collection can occur at the detector edges where the external electric field is not uniform and only a portion of the generated charge carriers drift towards the electrodes and induce a current.
4. In this region of the histogram, the  $^{12}\text{C}(n,n+2\alpha)^4\text{He}$  reaction can result in multiple  $\alpha$  emissions where the TCT signals are a superposition of each individual reactions. This results in a wide range of possible signal shapes.
5. The  $^{12}\text{C}(n,d)^{11}\text{B}$  and  $^{12}\text{C}(n,p)^{12}\text{B}$  reaction produce ions which, as with the  $^{12}\text{C}(n,\alpha)^9\text{Be}$  reaction, produce multi-step along with square pulse shapes. However, the amplitude of these pulses is lower due to less charge carriers being generated.

At even lower energy TCT signals resulting from elastic collision between the impinging neutron and the carbon atom can be observed. This reaction transfers a maximum of 28 % of the initial neutron energy to the carbon atom which causes it to vibrate in the diamond lattice (see section 2.3). This vibration can induce current in the electrodes and therefore produce a TCT pulse. This signal has the shape of a very fast and sharp pulse.

The signal benchmarking presented above was achieved by calculating various parameters of each TCT pulse such as its width, maximum amplitude, spectral density and performing numerical integration to get the deposited charge. The dataset was organized into histograms based on these parameters which allowed for the identification of groups with similar pulses. This method was

further used to recognize features in the data which could be used for PSD and will be discussed in more detail in the following section.

## 7.5 PSD of Neutron/ $\gamma$ -ray Signals

As was emphasized in the previous section, neutrons produce many different pulse shapes making it difficult to isolate only them. TCT signals results from  $\gamma$ -ray interaction which are generated by Compton electrons with a range in the order of millimeters will always produce the same pulse shape, that is a triangular shape. Therefore, discrimination can be achieved by identifying the  $\gamma$ -ray signals and all the remaining signals could be considered as those created by neutrons. However, when this triangular signal is superimposed with noise, it can be difficult to identify it.

PSD for the separation of neutron signals from  $\gamma$ -rays are commonly used with scintillator-based detectors and some methods have also been applied to diamond detectors. Discrimination methods found in literature were applied to the acquired dataset at room temperature and at low temperatures with limited success. The evaluation of the effectiveness of different discrimination methods is not straight forward since the neutron dataset, due to the nature of the experiment, will contain a small portion of  $\gamma$ -rays as well. However, the  $\gamma$ -ray dataset does not contain any neutron signals and it can be used to measure the success of the PSD method. The most frequently used strategies have been tested and their success has been estimated:

- **FWHM based PSD** - Discrimination techniques based on the ratio of the FWHM to the base width of the signal were proposed to isolate triangular pulses from square pulses [21]. This method is promising for the separation of ions from  $\gamma$ -rays, however the multi-step shape of a neutron TCT trace cannot be effectively categorized using this technique. As can be observed from Figure 7.18a, some separation is observed between the two datasets however with a lot of overlap. Figure 7.18a contains an occurrence frequency histogram of  $PSD\ FWHW = \frac{FWHM}{Pulse\ Width}$  values for both the neutron and  $\gamma$ -ray datasets. Only the neutrons which interact in the ballistic center and close to the electrodes are properly isolated ( $PSD\ FWHM > 0.7$ ). Neutron reactions which occur further way from the electrodes and the ballistic center of the detector are found between  $0.35 < PSD\ FWHM < 0.7$  and cannot be properly distinguished from  $\gamma$ -rays.

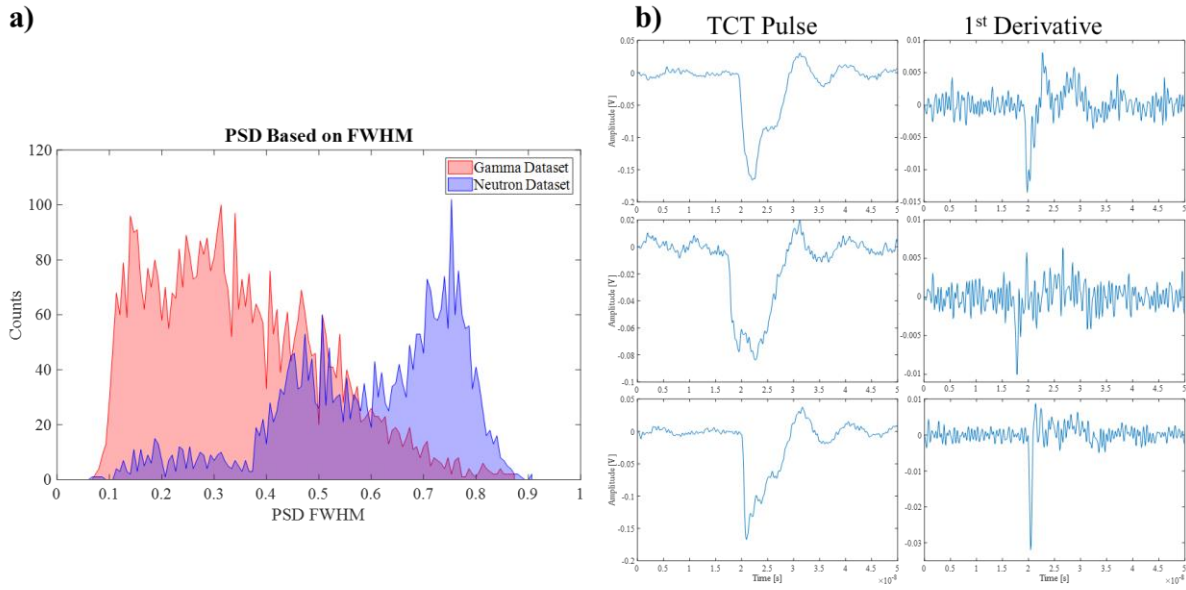


Figure 7.18 - a) FWHM based PSD and b) TCT traces (right) with their 1<sup>st</sup> derivative (left).

- 1<sup>st</sup> Derivative Peak Counting** – Neutron/ $\gamma$ -ray discrimination can be also achieved by counting the number of peaks present in the derivative of the TCT pulse. Neutron signals with a multi-step shape should contain multiple peaks while a triangular  $\gamma$ -ray signal should have only one peak [76]. Figure 7.18b contains two different neutron pulses and a  $\gamma$ -ray pulse with their respective 1<sup>st</sup> derivatives on the plot to the right. A double peak can be observed in the derivative of the multi-step pulse; however, the derivatives of the square and the triangle pulse are identical in the number of peaks. Furthermore, this method is extremely sensitive to the SNR which can be concluded by the size of the second peak in the derivative of the multi-step pulse. Noise introduces sudden shifts in the amplitude of the signal which result in sharp peaks when differentiated. No discrimination was observed when applying this method to the acquired datasets.
- Frequency Domain Analysis** – Neutron signals contain more flat sections in the pulse shape followed by multiple sharp edges while  $\gamma$ -rays contain one sharp edge followed by a slow changing section. Transforming this to the frequency domain results in the magnitude of lower and higher frequencies being higher for neutron signals while the midrange frequencies are higher for  $\gamma$ -ray signals. This is observed when comparing the FFT of neutron signals to  $\gamma$ -ray signal as presented in the top plot of Figure 7.19. The magnitude of the frequency components in the range of 300 MHz to 800 MHz is higher

for the black curve which represents the  $\gamma$ -ray signal. However, the difference in the magnitude in this region is less than the fluctuation due to the noise which makes it not usable for discrimination purposes. Therefore, no significant differences were observed between the two acquired datasets when applied this discrimination method.

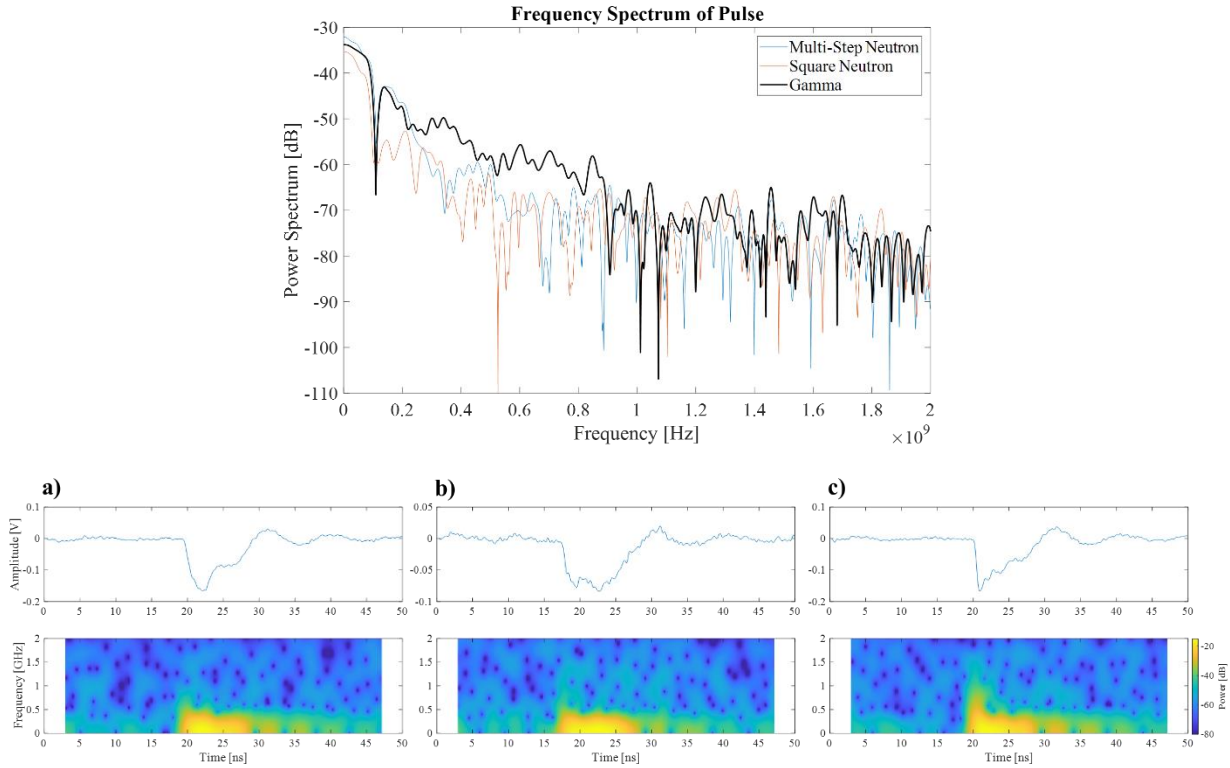


Figure 7.19 - Frequency domain analysis. The top plot contains the FFT of the two neutron shapes (blue, red) and the  $\gamma$ -ray shape (black). Bottom plot contains the associated spectrograms of the same three shapes: a) multi-step neutron, b) square neutron, c)  $\gamma$ -ray.

- **Wavelet Power Spectrum Analysis** – Frequency domain analysis can be expanded to show the frequency components per unit time of the signal (windowed Fourier transforms). The bottom plots of Figure 7.19 illustrates the two types of neutron signal shapes (a and b) and the  $\gamma$ -ray signal shape (c) along with their respective spectrogram. As was concluded with the frequency domain analysis, the  $\gamma$ -ray signal shape contains more frequency components in the range of 300 MHz to 800 MHz when compared to the neutron signals. However, this method is also very sensitive to noise and no reliable discrimination was achieved when applied to the acquired datasets.

- **Neural Networks/Machine Learning** – Demonstrations of deep learning algorithms used to discriminate neutron/ $\gamma$ -rays were found in literature, some of which were applied to diamond detectors at room temperature. Most notably [84], where Huang et al. utilized unsupervised machine learning classification algorithms, more specifically a self-organizing map algorithm to classify the data. However, the method described in the literature was not applied to the acquired datasets due to the  $\mu$ LoM requirement for the DONES accelerator to function in real time. Additionally, training the algorithm was not feasible with the acquired dataset because, at low temperatures, it was not possible to obtain two mutually exclusive datasets consisting solely of neutron or  $\gamma$ -ray signals.

The limited success of all the discrimination strategies listed above was predominantly due to their sensitivity to the noise level of the signal. The SNR proved to be too low, even though the noise was minimized by examining its various sources and the system design was optimized to achieve the greatest possible SNR during the experiments. Further filtering both in the analog and digital domain also proved to be ineffective since the signal of interest is located in the same frequency range as the noise. Any filtering greatly altered the shape of the TCT pulse making proper identification difficult. Limited success was achieved with algorithms based on comparing the pulse shapes in the datasets with ideal theoretical shapes using the least squares method [76] as well as the cosine similarity method [81]. However, fitting the acquired datasets to ideal shapes proved to be a good initial step for grouping signal shapes which allowed for the selection of reference signal, which then were used for comparison using the cosine similarities method. Using this methodology, the chosen reference TCT signals for neutrons at 120 K, 55 K and  $\gamma$ -rays are presented in Figure 7.16 and Figure 7.15b, respectively.

Based on the results from evaluating discrimination strategies found in literature, two methods for PSD were further developed which yielded the best outcomes when applied to the acquired datasets. The developed discrimination methods are based on the cosine similarity techniques utilized predominately for scintillator detectors. This method was chosen because it was found that they are more resistant to the low SNR at cryogenic temperatures. In order to apply these techniques, an algorithm for preprocessing the datasets first had to be developed and all the signals in the dataset had to be classified/benchmarked in order to select the best reference signals. The datasets were first organized by comparing the TCT traces with an ideal square shape. This was

followed by comparing the portion of the trace from the signal minimum to the end of the pulse with a straight line. Traces that are closer in shape to a square pulse have a higher probability of being created by neutrons while a more linear return to the baseline amplitude created by  $\gamma$ -rays, respectively. Two methods were devised to discriminate the datasets: method #1 utilized the most common neutron and  $\gamma$ -ray pulse shape as a reference signal, while method #2 utilized the two most common neutron shapes as reference signals to which a cosine similarity was computed. However, before the cosine similarity could be calculated for each method, pulse parameters such as the start position, end position and minimum value had to be extracted. The full procedure for the applied PSD method #1 and #2 is listed below. All the following steps are common to method #1 and method #2 with the exception of step 6 which is specific for each applied method.

1. **Baseline determination** – All TCT traces contain a certain inherent positive DC offset caused by the combination of noise and amplifier design. This offset had to be determined in order to more accurately gauge the start and end position of the pulse. Since all the TCT traces are negative, this was achieved by taking the minimum value as a starting point and following the signal in both directions until reaching the zero crossing. The portion of the signal between the two zero crossings was removed. The average noise amplitude and DC offset were then calculated from the remaining signal.
2. **Start/End pulse position** – The start and end positions of the pulse were found by again tracing the original signal from the minimum value in both directions to the calculated baseline amplitude considering the average noise level calculated in step 1. The found positions are abbreviated: startPos, endPos and minPos.
3. **Start position alignment** – In order to calculate the PSD using the cosine method in later steps between two signals in the dataset, the signals were shifted using a circular buffer to align all pulse start position.
4. **Finding reference pulse shapes** – PSD values were first calculated against an ideal line and ideal square pulse shape using the cosine similarity method to identify the most common types of signal shapes in the datasets. An ideal line was constructed between the pulse minimum position (minPos) and the pulse end position (endPos) using the following equation:

$$r_i = \frac{y_{endPos} - y_{minPos}}{x_{endPos} - x_{minPos}}(x_i - x_{minPos}) + y_{minPos} \quad (7.2)$$

This ideal line was compared to the TCT trace between the same two points leading to a cosine similarities value between 0 (no similarity) and 1 (the same) using the equation below where  $s_i$  represents the TCT trace values,  $r_i$  the reference signal (the ideal line in this case) and  $x_{startPos}$ ,  $x_{endPos}$ ,  $y_{startPos}$ ,  $y_{endPos}$  represent the x and y coordinated of the start and end positions of the signal respectively.

$$PSD_{Line} = \frac{\sum_{i=x_{minPos}}^{x_{endPos}} s_i r_i}{\sqrt{\sum_{i=x_{minPos}}^{x_{endPos}} s_i^2} \sqrt{\sum_{i=x_{minPos}}^{x_{endPos}} r_i^2}} \quad (7.3)$$

An ideal square pulse shape was created by setting the values of the signal to zero everywhere except in-between the calculated start and end positions of the TCT pulse, where it was set to 1:

$$r_i = \begin{cases} 1, & startPos \leq i \leq endPos \\ 0, & elsewhere \end{cases} \quad (7.4)$$

This ideal square pulse was then compared to the TCT traces which simplifies the cosine similarity formula to [81]:

$$PSD_{Square} = \frac{\sum_{i=x_{startPos}}^{x_{endPos}} s_i}{\sqrt{(x_{endPos} - x_{startPos})} \sqrt{\sum_{i=x_{startPos}}^{x_{endPos}} s_i^2}} \quad (7.5)$$

5. **2D Histogram PSD Square vs PSD Line** – Plotting the results as a 2D histogram, presented in Figure 7.20, shows some separation and conglomeration of TCT signal shapes. However, only a small portion of the  $\gamma$ -ray signals are separated from the neutron signals as can be observed by only one group containing a higher count of signals (marked in yellow) and therefore not an effective method for discriminating between neutron and  $\gamma$ -ray signals. This step is however useful for identifying the most dominant neutron and  $\gamma$ -ray shapes.

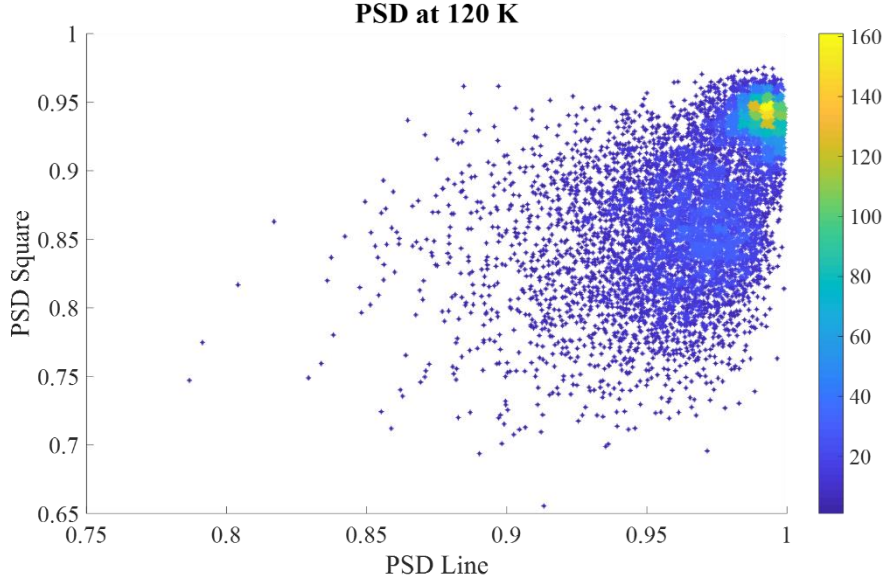


Figure 7.20 - 2D histogram of cosine similarities of the datasets to an ideal line (x-axis) and ideal square (y-axis).

- 6a. **PSD Method #1** – The most frequent neutron and  $\gamma$ -ray shapes were identified from the initial grouping performed in the previous step. The most common neutron signal was the multi-step shape (top plot of Figure 7.18b) and for  $\gamma$ -rays, the triangular shape (bottom plot of Figure 7.18b). These shapes were used as referent signals for further discrimination.
- 6b. **PSD Method #2** – The most frequent neutron shapes were identified from the initial grouping performed in step 4. As predicted, these were a multi-step (top plot of Figure 7.18b) and a square (middle plot of Figure 7.18b) shape signal.
7. **PSD Calculation** – With all the TCT signals aligned by the start position of the pulse and their lengths being the same, a direct comparison to calculate the cosine similarity of the two signals was possible using the following equation:

$$PSD_{Ref_{n(g)}} = \frac{\sum_{i=startPos}^{endPos} S_i r_i}{\sqrt{\sum_{i=startPos}^{endPos} S_i^2} \sqrt{\sum_{i=startPos}^{endPos} r_i^2}} \quad (7.6)$$

8. **Discrimination Method Evaluation** – Method #1 resulted in an array of cosine similarity values PSD\_Neutron and PSD\_Gamma while method #2 resulted in PSD\_Square and PSD\_MultiStep. For each method a 2D histogram was created at each temperature showing the distribution of all signals in the datasets in comparison to the reference signals



chosen by each method. Two conglomerations of signals were observed, one for neutrons and one for  $\gamma$ -ray pulses. The discrimination quality was then evaluated by a linear projection of the 2D histogram along the line of best separation between the two groups. A Figure of Merit (FOM) was calculated by first fitting the neutron and  $\gamma$ -ray peaks in the linear projection and then applying the following formula:

$$FOM = \frac{|n_{centroid} - \gamma_{centroid}|}{n_{FWHM} + \gamma_{FWHM}} \quad (7.7)$$

Using the above procedure, the two datasets were combined and evaluated at each temperature setpoint. The 2D histogram displaying the results of step 6 for method #2 for data acquired at 120 K is illustrated in Figure 7.21. For this method, the two neutron shapes were used as reference signals producing 2D histogram with neutron signals located closer to the top right corner of the plot while  $\gamma$ -ray signals closer to the center of the plot. The almost complete separation of the neutron signals from the  $\gamma$ -ray signals in the plot indicates that a good discrimination was achieved using this method. Furthermore, it can also be observed from the plot that most of the neutron signals are of the multi-step shape as was statistically expected.

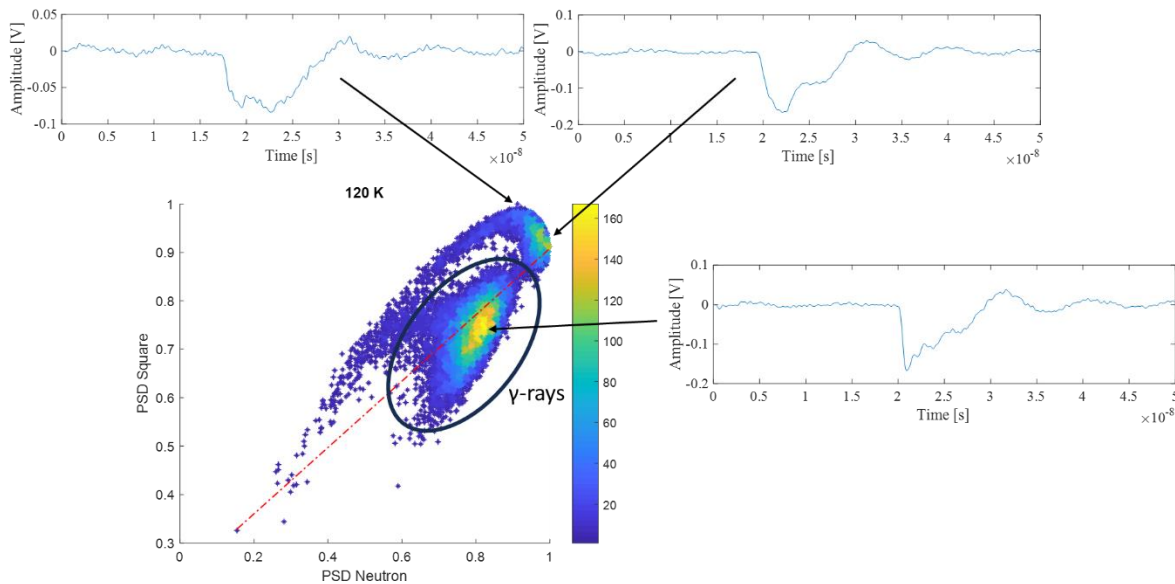


Figure 7.21 - 2D Histogram of results obtained with Method #2 at 120 K.

The 2D histograms along with their associate linear projection used to calculate the FOM using discrimination method #1 and method #2 at each acquired temperature is presented in Figure 7.22 and Figure 7.23, respectively. The plots are organized by temperature, the highest temperature, 120 K, results are presented in the top left corner of the figure (a), while the lowest, 46 K, in the bottom right corner (i). As mentioned above, the 2D histogram presents the similarity on a scale of 0 to 1 while the linear projection contains arbitrary units, that is, the histogram bin numbers.

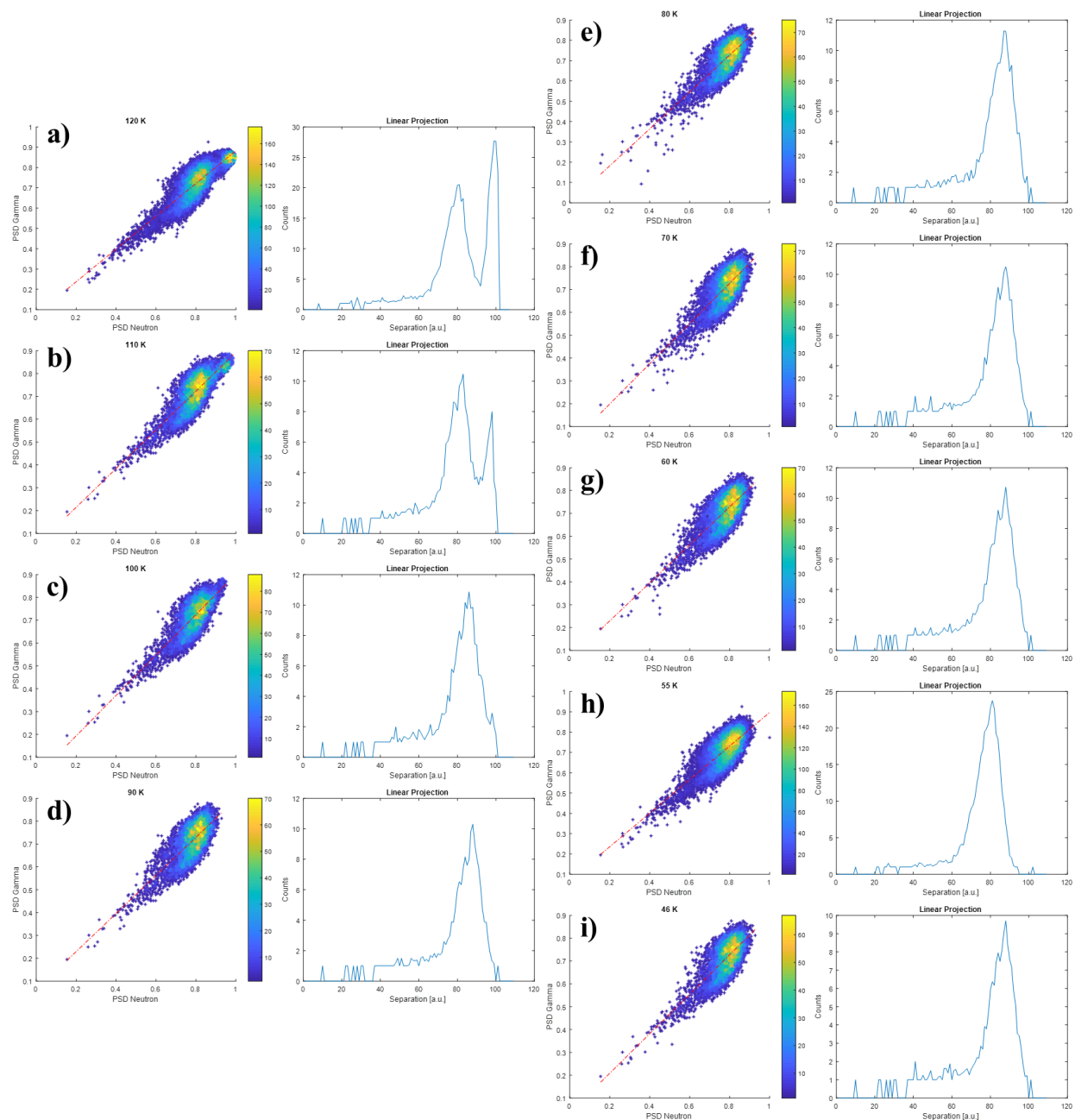


Figure 7.22 - PSD Method #1 results presented as 2D histogram (left) and linear projection (right) at temperatures a) 120 K b) 110 K c) 100 K d) 90 K e) 80 K f) 70 K g) 60 K h) 55 K and i) 46 K.

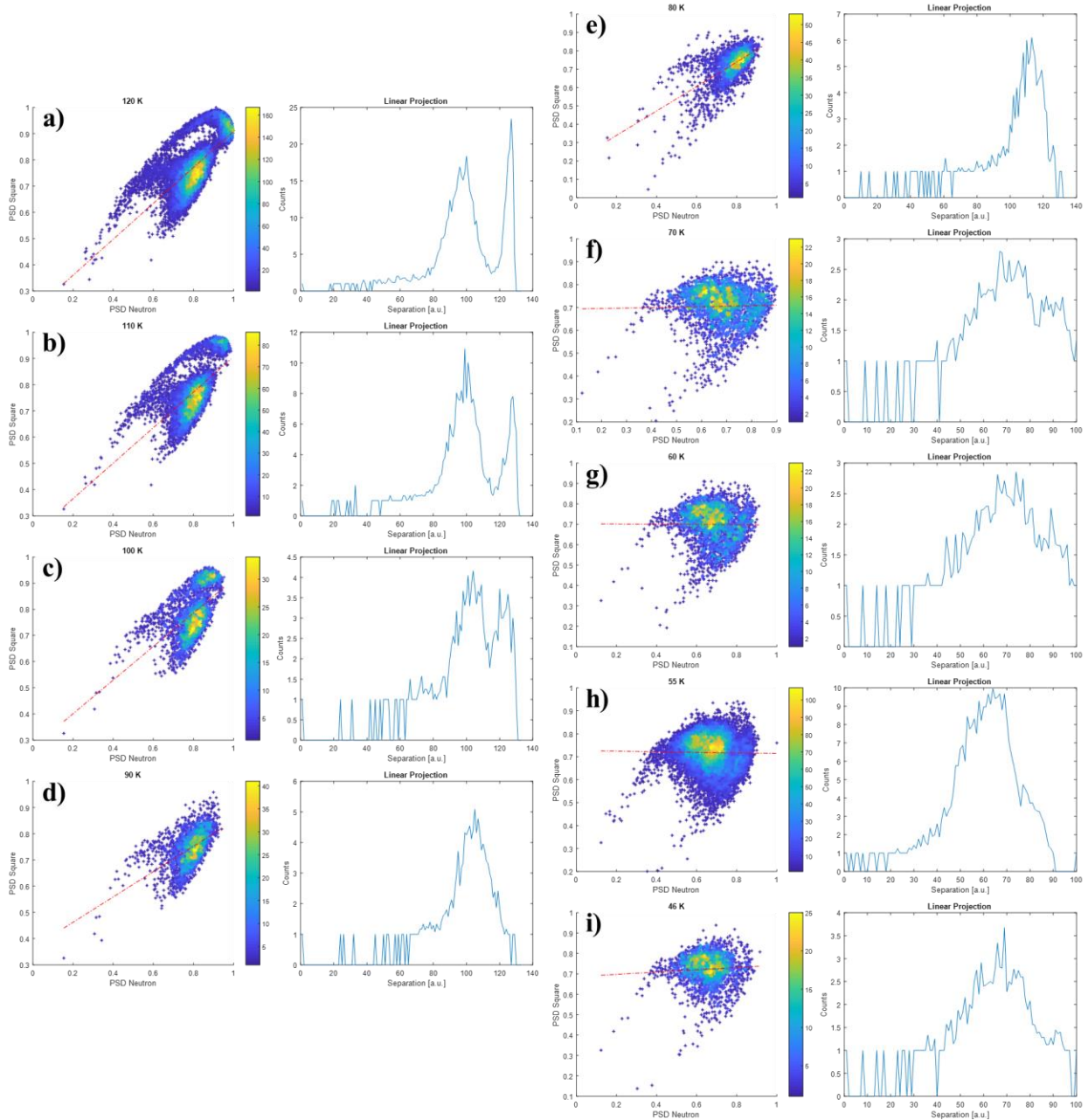


Figure 7.23 - PSD Method #2 results presented as 2D histogram (left) and linear projection (right) at temperatures a) 120 K b) 110 K c) 100 K d) 90 K e) 80 K f) 70 K g) 60 K h) 55 K and i) 46 K.

From the above figures it is observed that at higher temperatures two peaks are visible in the linear projections, the left peak comprised of  $\gamma$ -ray signals while the right neutron signals. However, as the temperature decreases, the neutron peak begins to shift towards the  $\gamma$ -ray peak and quickly becomes indistinguishable. This indicates that the discrimination method was ineffective

in separating neutrons from  $\gamma$ -ray signals at lower temperatures. As the temperature decreases, so does the CCE of the diamond detector resulting in a lower SNR of the TCT pulses. Lower SNR means that the noise has a greater impact on the shape of the pulse effectively altering it and making it less distinguishable from a  $\gamma$ -ray pulse shape.

*Table 7.3 - FOM results for the evaluation of the presented two PSD methods at different temperatures.*

<b>Temperature</b>	<b>FOM PSD Method #1</b>	<b>FOM PSD Method #2</b>
120	0.8971	1.0489
110	0.7483	0.9493
100	-	0.4272
90	-	-

The effectiveness of each PSD method can be better evaluated by examining the FOM values which are presented in Table 7.3. As was observed by the 2D histograms plots, FOM values could only be calculated for higher temperature datasets where a separation between neutron and  $\gamma$ -ray signals was observed. Additionally, from the FOM results, it can be concluded that the second PSD method employed was more efficient than the first one. However, both discrimination methods do not work below 100 K due to the low SNR. The SNR was the limiting factor for successful neutron/ $\gamma$ -ray discrimination and as such a lot of attention was dedicated to studying all sources of noise and minimizing them. However, the decreases in the CCE of a diamond detector operating at cryogenic temperatures was greater than how much SNR could be recovered by the employed noise minimization techniques.

To validate the performance of the developed neutron/ $\gamma$ -ray discrimination methods described above, the results were compared to discrimination methods found in literature. However, a direct comparison is difficult because of the higher levels of noise present in the dataset acquired in this work due to the operation of the cryopump, the accelerator and other support systems. Measuring with a diamond detector in a cryostat with a radioactive source greatly reduces the amount of noise in the system which increases the SNR. This represents a highly un-realistic environment for the operation of diamond-based neutron detectors ( $\mu$ LoM). In real-case scenarios neutron detectors ( $\mu$ LoM) would be exposed to various noise resulting from the accelerator's operation, as well as

from the operation of vacuum systems and various support facilities. As was mentioned in the previous paragraph, discrimination algorithms are very sensitive to the SNR and their efficiencies drop very quickly with lower SNR values. Furthermore, only the data acquired at the highest acquired temperature of 120 K can be compared to room temperature values found in literature, as lower temperature data does not exist. The highest FOM value achieved with the developed algorithms was around 1, while FOM values ranging from 0.8 to 4 were found in literature [69], [77], [83], [88], [108]. However, these values were obtained with scintillator detectors and not diamond detectors. All articles found in literature which applied PSD algorithms to a diamond detector present their performance as a percentage of the total number of neutrons in the dataset [75], [76], [84]. A direct comparison to these results is not possible since the total number of only neutron events acquired during the experiment is unknown due to the conditions at the RBI neutron generator at the time. Future experiments will be performed where the associate alpha particle from the neutron reaction is also measured and correlated with events registered by the diamond detector to give the exact number of neutrons. Although, this number can be estimated by knowing the approximate flux on neutrons generated, the solid angle of the detector and the efficiency of the detector, calculating the efficiency of the detector is not trivial as it is neutron energy dependent and the error in the calculation would be very large.



## 8 CONCLUSION

Recent advances in accelerator and fusion technology require a new generation of detectors that will be able to meet the requirements of operating in harsh environments reliably. Detectors based on single crystal CVD diamond are seen as one possible solution that could meet these requirements. As a wide bandgap semiconductor (5.47 eV), with high mobility of charge carriers, the ability of applying large bias potential with a very low leakage current, makes diamond suitable for a high dynamic range operation from very low to very high rate measurements. Furthermore, due to its large atomic displacement energy (43 eV), it is intrinsically radiation hard and therefore it can be placed close to the high intensity radiation sources found in accelerators. But most importantly, diamond detectors can be intrinsically used as neutron detectors by the possible nuclear reactions with the carbon atom for neutrons of 6.2 MeV or higher. Due to these characteristics and their compact size, scCVD diamond detectors are prime candidates for BLM in large accelerator facilities such as the LHC, IFMIF-DONES and ITER. However, due to the use of superconducting magnets in these facilities, detectors that are placed close to the beam or plasma source must also operate at cryogenic temperatures.

This work provides an insight into the various aspects of detector development and the current state of the art technology level of diamond detectors. Focus was given to the operation of a diamond detector at cryogenic temperatures and the problems that arise from utilizing a detector in such an environment. An optimized experimental setup was constructed, and methods were developed to systematically evaluate the performance of a diamond detector over a wide temperature range from 46 K to 295 K. More specifically, two ion beam analysis techniques, IBIC and TCT, were used to measure the CCE. Each of the applied analysis techniques required a unique signal processing chain and filtering both in the analogue and digital domain. Each component in this chain was carefully selected optimized to achieve the highest SNR. The SNR of the experimentally acquired data proved to be the key parameter for the evaluation of the detector since the performance of the detector dropped drastically towards cryogenic temperatures. CCE profiles were collected from 46 K to 295 K for impinging ions of H, He, Li, and C along with neutrons and  $\gamma$ -rays. It was found that the performance of the detector degraded at cryogenic temperatures to all types of radiation however, with different magnitudes. The CCE decreased to  $39.3 \pm 0.8 \%$ ,  $24.7 \pm 0.4 \%$ ,  $23.6 \pm 1.3 \%$ ,  $25.9 \pm 0.8 \%$  and  $86.2 \pm 0.5 \%$  for H, He, Li, C and  $\gamma$ -rays, respectively. The magnitude of the decrease in CCE for neutrons was impossible to evaluate due to neutron signals



being indistinguishable from the background noise and  $\gamma$ -rays below 70 K, at which point the CCE already dropped by more than 50 %. This highlights one of the main problems which must be solved before utilizing diamond detectors as  $\mu$ LoM at cryogenic temperatures, specifically the ability to discriminate neutrons from  $\gamma$ -rays. PSD techniques found in literature were applied to the datasets of current profiles generated at the detector electrodes and obtained during experiments with limited results, as presented. To aid the development of new PSD methods, these current profiles were benchmarked against theoretically expected pulse shapes. This provided insight into the operation of the detector in real life conditions where the signals shapes are affected not only by the type of radiation and front-end electronics, but by the finite electrode size and external interference sources as well. It was found that a significant portion of the signals could not be successfully discriminated specifically due to these effects as it caused expected neutron current profiles to resemble a  $\gamma$ -ray shape. Based on the benchmarked data, two methods for PSD neutron/ $\gamma$ -ray discrimination were developed. Both methods were evaluated offline with the acquired datasets at various temperatures from 120 K down to 46 K. The performance of each method was assessed using the FOM method. Good discrimination was achieved at higher temperature where the CCE was higher, however both methods failed when applied to data acquired at cryogenic temperatures.

The main reason that each PSD method failed at cryogenic temperatures was related to the very low CCE which results in a very low SNR of the pulse being analyzed, increasing the influence of noise on the overall shape of the signal. During this work, it was found that CCE of a diamond detector operating at cryogenic temperatures could be increased by the application of higher bias voltages. This would increase the generated charge carrier separation speed and decrease their probability of entering an exciton state. Due to the limitation of the constructed apparatus, only a relatively small increase in the bias voltage, from 1 V/ $\mu$ m to 1.3 V/ $\mu$ m, was possible. However, even with this small increase, a higher CCE at cryogenic temperatures was observed which translates to a better SNR of the current pulse and therefore higher performance of the PSD developed PSD algorithms. A systematic study of higher bias voltages which take advantage of the diamonds' large dielectric strength was identified as one of the main areas requiring further research in order to develop  $\mu$ LoM based on diamond detectors, along with the study of the effects of radiation damage on the detector performance as well as the influence of very large external magnetic fields on the operation the detector. Only after acquiring this knowledge, can a diamond

detector be used successfully as a  $\mu$ LoM and its response interpreted correctly in an environment such as the one expected in DONES. As this work demonstrates, diamond detectors have exceptional qualities, and they can be very beneficial for future fusion and accelerator facilities. More development and research are required; however, the pace of progress is very encouraging, and a working diamond-based  $\mu$ LoM is not far off.



## BIBLIOGRAPHY

- [1] A. J. H. Donné, “The European roadmap towards fusion electricity,” *Philos. Trans. R. Soc. A Math. Phys. Eng. Sci.*, vol. 377, no. 2141, 2019, doi: 10.1098/rsta.2017.0432.
- [2] J. M. Arroyo *et al.*, “Dones conceptual design report,” no. April, 2014.
- [3] J. Egberts, “IFMIF-LIPAc Beam Diagnostics: Profiling and Loss Monitoring Systems,” Universite Paris Sud, 2012.
- [4] J. Marroncle *et al.*, “IFMIF-LIPAC diagnostics and its challenges,” *IBIC 2012 - Proc. 1st Int. Beam Instrum. Conf.*, pp. 557–565, 2013.
- [5] J. Marroncle, P. Abbon, J. Egberts, and M. Pomorsk, “u-loss detector for Ifmif-Eveda,” *Proc. DIPAC2011*, pp. 146–148, 2008.
- [6] W. De Boer *et al.*, “Radiation hardness of diamond and silicon sensors compared,” *Phys. Status Solidi Appl. Mater. Sci.*, vol. 204, no. 9, pp. 3004–3010, 2007, doi: 10.1002/pssa.200776327.
- [7] L. Băni *et al.*, “A study of the radiation tolerance of cvd diamond to 70 mev protons, fast neutrons and 200 mev pions,” *Sensors (Switzerland)*, vol. 20, no. 22, pp. 1–19, 2020, doi: 10.3390/s20226648.
- [8] F. Bachmair, “Diamond sensors for future high energy experiments,” *Nucl. Instruments Methods Phys. Res. Sect. A Accel. Spectrometers, Detect. Assoc. Equip.*, vol. 831, pp. 370–377, Sep. 2016, doi: 10.1016/j.nima.2016.03.039.
- [9] W. Adam *et al.*, “Radiation hard diamond sensors for future tracking applications,” *Nucl. Instruments Methods Phys. Res. Sect. A Accel. Spectrometers, Detect. Assoc. Equip.*, vol. 565, no. 1, pp. 278–283, Sep. 2006, doi: 10.1016/j.nima.2006.05.127.
- [10] I. Zamboni, Ž. Pastuović, and M. Jakšić, “Radiation hardness of single crystal CVD diamond detector tested with MeV energy ions,” *Diam. Relat. Mater.*, 2013, doi: 10.1016/j.diamond.2012.11.002.
- [11] H. Kagan *et al.*, “Diamond detector technology, status and perspectives,” *Nucl. Instruments Methods Phys. Res. Sect. A Accel. Spectrometers, Detect. Assoc. Equip.*, vol. 924, pp. 297–300, 2018, doi: 10.1016/j.nima.2018.06.009.
- [12] R. S. Sussmann, *CVD Diamond for Electronic Devices and Sensors*. Chichester, UK: John Wiley & Sons, Ltd, 2009.
- [13] J. K. Shultis and R. E. Faw, *Radiation shielding*. La Grange Park, IL: American Nuclear Society, 2000.
- [14] J. Beringer *et al.*, “Review of particle physics,” *Phys. Rev. D - Part. Fields, Gravit. Cosmol.*, vol. 86, no. 1, 2012, doi: 10.1103/PhysRevD.86.010001.
- [15] G. F. Knoll, *Radiation Detection and Measurement*, 4th ed. New York: John Wiley and Sons, Inc., 2010.

- [16] J. F. Ziegler, M. D. Ziegler, and J. P. Biersack, “SRIM - The stopping and range of ions in matter (2010),” *Nucl. Instruments Methods Phys. Res. Sect. B Beam Interact. with Mater. Atoms*, vol. 268, no. 11–12, pp. 1818–1823, 2010, doi: 10.1016/j.nimb.2010.02.091.
- [17] J. Lilley, *Nuclear Physics - Principles and Applications*. Wiley, 2001.
- [18] M. Angelone and C. Verona, “Properties of Diamond-Based Neutron Detectors Operated in Harsh Environments,” *J. Nucl. Eng.*, vol. 2, no. 4, pp. 422–470, 2021, doi: 10.3390/jne2040032.
- [19] “Experimental Nuclear Reaction Data (EXFOR),” *International Atomic Energy Agency*. <https://www-nds.iaea.org/exfor/> (accessed Mar. 11, 2022).
- [20] “NuDat 3.0,” *National Nuclear Data Center*. <https://www.nndc.bnl.gov/nudat3/> (accessed Mar. 11, 2022).
- [21] C. Weiss, H. Fraiss-Kölbl, E. Griesmayer, and P. Kavargin, “Ionization signals from diamond detectors in fast-neutron fields,” *Eur. Phys. J. A*, vol. 52, no. 9, p. 269, Sep. 2016, doi: 10.1140/epja/i2016-16269-8.
- [22] W. Catford, “CATKIN.” <http://personal.ph.surrey.ac.uk/~phs1wc/kinematics/> (accessed Mar. 17, 2022).
- [23] M. Angelone *et al.*, “Neutron detectors based upon artificial single crystal diamond,” *IEEE Trans. Nucl. Sci.*, vol. 56, no. 4, pp. 2275–2279, 2009, doi: 10.1109/TNS.2009.2025177.
- [24] M. Osipenko *et al.*, “Neutron spectrometer for fast nuclear reactors,” *Nucl. Instruments Methods Phys. Res. Sect. A Accel. Spectrometers, Detect. Assoc. Equip.*, vol. 799, pp. 207–213, Nov. 2015, doi: 10.1016/j.nima.2015.07.050.
- [25] J. Holmes *et al.*, “Performance of 5- $\mu$ m PIN diamond diodes as thermal neutron detectors,” *Nucl. Instruments Methods Phys. Res. Sect. A Accel. Spectrometers, Detect. Assoc. Equip.*, vol. 961, no. December 2019, p. 163601, 2020, doi: 10.1016/j.nima.2020.163601.
- [26] X. Xie *et al.*, “Application of a single crystal chemical vapor deposition diamond detector for deuteron plasma neutron measurement,” *Nucl. Instruments Methods Phys. Res. Sect. A Accel. Spectrometers, Detect. Assoc. Equip.*, vol. 761, pp. 28–33, Oct. 2014, doi: 10.1016/j.nima.2014.05.067.
- [27] H. Barschall *et al.*, *Neutron sources for basic physics, and their applications*, 1st ed. Oxford; New York: Pergamon Press, 1983.
- [28] S. Friedland S., J. Mayer, W., and J. Wiggins, S., “The solid ionization chamber,” *IRE Trans. Nucl. Sci.*, vol. 7, no. 2/3, pp. 181–185, 1960, doi: 10.1109/TNS2.1960.4315761.
- [29] C. Weiss, “A CVD Diamond Detector for (n, $\alpha$ ) Cross-Section Measurements,” Vienna University of Technology, Vienna, 2014.
- [30] M. Pomorski, “Electronic properties of single crystal CVD diamond and its suitability for particle detection in hadron physics experiments,” no. January 2008, 2008.
- [31] H. Jansen, “Chemical Vapour Deposition Diamond - Charge Carrier Movement at Low Temperatures and Use in Time-Critical Applications,” Bonn University, 2013.

- [32] J. Marroncle, P. Abbon, A. Marchix, and M. Pomorski, “R & D on micro-loss monitors for high intensity LINACS like LIPAc,” *Beam Instruments Interact.*, pp. 538–542, 2016.
- [33] D. Jain, J. Nuwad, N. Manoj, and V. Sudarsan, “Diamond-Based Radiation Detectors for Applications in Highly Corrosive Solutions and High-Radiation Fields,” in *Materials Under Extreme Conditions: Recent Trends and Future Prospects*, Elsevier Inc., 2017, pp. 683–715.
- [34] R. Alig, C. S. Bloom, and C. Struck, W., “Scattering by ionization and phonon emission in semiconductors,” *Phys. Rev. B*, vol. 22, no. 12, pp. 5565–5582, 1980, doi: 10.1103/physrevb.22.5565.
- [35] H. Pernegger *et al.*, “Charge-carrier properties in synthetic single-crystal diamond measured with the transient-current technique,” *J. Appl. Phys.*, vol. 97, no. 7, 2005, doi: 10.1063/1.1863417.
- [36] S. Ramo, “Currents Induced by Electron Motion,” *Proc. of IRE*, vol. 27, no. 9, 1939.
- [37] N. Skukan, V. Grilj, and M. Jakšić, “CVD diamond as a position sensitive detector using charge carrier transition time,” *Nucl. Instruments Methods Phys. Res. Sect. B Beam Interact. with Mater. Atoms*, 2013, doi: 10.1016/j.nimb.2012.12.055.
- [38] H. Pernegger, “High mobility diamonds and particle detectors,” *Phys. Status Solidi Appl. Mater. Sci.*, vol. 203, no. 13, pp. 3299–3314, 2006, doi: 10.1002/pssa.200671404.
- [39] C. Kurfuerst, “Cryogenic Beam Loss Monitoring for the LHC,” Technical University of Vienna, 2013.
- [40] M. Cerv, “CVD diamond applications for particle detection and identification in high-radiation environments,” Technical University Vienna, Vienna, 2016.
- [41] S. M. Sze and K. K. Ng, *Physics of Semiconductor Devices*, 3rd ed. Hoboken, NJ, USA: John Wiley & Sons, Inc., 2006.
- [42] M. A. Tamor and J. P. Wolfe, “Drift and diffusion of free excitons in Si,” *Phys. Rev. Lett.*, vol. 44, no. 25, pp. 1703–1706, 1980, doi: 10.1103/PhysRevLett.44.1703.
- [43] P. J. Dean, E. C. Lightowers, and D. R. Wight, “Intrinsic and extrinsic recombination radiation from natural and synthetic aluminum-doped diamond,” *Phys. Rev.*, vol. 140, no. 1A, 1965, doi: 10.1103/PhysRev.140.A352.
- [44] K. Takiyama, M. I. Abd-Elrahman, T. Fujita, and T. Oda, “Photoluminescence and decay kinetics of indirect free excitons in diamonds under the near-resonant laser excitation,” *Solid State Commun.*, vol. 99, no. 11, pp. 793–797, 1996, doi: 10.1016/0038-1098(96)00309-2.
- [45] H. Jansen, D. Dobos, T. Eisel, H. Pernegger, V. Eremin, and N. Wermes, “Temperature dependence of charge carrier mobility in single-crystal chemical vapour deposition diamond,” *J. Appl. Phys.*, vol. 113, no. 17, p. 173706, 2013, doi: 10.1063/1.4802679.
- [46] H. Jansen, D. Dobos, H. Pernegger, N. Wermes, V. Eremin, and R. Sauer, “C-TCT measurements on scCVD diamond and its use at CNGS.” DESY, Hamburg, pp. 1–47, 2014.

- [47] M. Guthoff, “Radiation Damage to the diamond-based Beam Condition Monitor of the CMS Detector at the LHC,” Karlsruhe Institute of Technology, 2014.
- [48] T. Naaranoja, M. Golovleva, L. Martikainen, M. Berretti, and K. Österberg, “Space charge polarization in irradiated single crystal CVD diamond,” *Diam. Relat. Mater.*, vol. 96, pp. 167–175, Jun. 2019, doi: 10.1016/j.diamond.2019.03.007.
- [49] M. R. Ramos, A. Crnjac, D. Cosic, and M. Jakši, “Ion Microprobe Study of the Polarization Quenching Techniques in Single Crystal Diamond Radiation Detectors,” *Materials (Basel)*, vol. 15, no. 1, p. 388, 2022, doi: <https://doi.org/10.3390/ma15010388>.
- [50] C. Kurfürst *et al.*, “In situ radiation test of silicon and diamond detectors operating in superfluid helium and developed for beam loss monitoring,” *Nucl. Instruments Methods Phys. Res. Sect. A Accel. Spectrometers, Detect. Assoc. Equip.*, vol. 782, pp. 149–158, 2015, doi: 10.1016/j.nima.2015.02.002.
- [51] K. Konishi *et al.*, “Low-temperature mobility-lifetime product in synthetic diamond,” *Appl. Phys. Lett.*, vol. 117, no. 21, p. 212102, 2020, doi: 10.1063/5.0031600.
- [52] F. Nava *et al.*, “Transport properties of natural diamond used as nuclear particle detector for a wide temperature range,” *IEEE Trans. Nucl. Sci.*, vol. NS-26, no. 1, 1979.
- [53] J. Isberg, M. Gabrysch, S. Majdi, and D. J. Twitchen, “Negative electron mobility in diamond,” *Appl. Phys. Lett.*, vol. 100, no. 17, 2012, doi: 10.1063/1.4705434.
- [54] R. Sauer, “Modeling novel effects in transient current measurements of single-crystal CVD diamond with carrier excitation by MeV  $\alpha$ -particles,” *Diam. Relat. Mater.*, vol. 111, no. April 2020, p. 108166, Jan. 2021, doi: 10.1016/j.diamond.2020.108166.
- [55] K. Konishi, I. Akimoto, J. Isberg, and N. Naka, “Diffusion-related lifetime and quantum efficiency of excitons in diamond,” *Phys. Rev. B*, vol. 102, no. 19, p. 195204, 2020, doi: 10.1103/PhysRevB.102.195204.
- [56] T. Ichii, Y. Hazama, N. Naka, and K. Tanaka, “Study of detailed balance between excitons and free carriers in diamond using broadband terahertz time-domain spectroscopy,” *Appl. Phys. Lett.*, vol. 116, no. 23, p. 231102, 2020, doi: 10.1063/5.0006993.
- [57] M. Wiehe *et al.*, “Development of a Tabletop Setup for the Transient Current Technique Using Two-Photon Absorption in Silicon Particle Detectors,” *IEEE Trans. Nucl. Sci.*, vol. 68, no. 2, pp. 220–228, 2021, doi: 10.1109/TNS.2020.3044489.
- [58] CAEN, “WP2081 - Digital Pulse Processing in Nuclear Physics - Overview of CAEN DPP algorithms.” CAEN S.pA, Viareggio, Italy, 2017.
- [59] M. Nakhostin, “Signal Processing for Radiation Detectors,” p. 528, Oct. 2017, doi: 10.1002/9781119410225.
- [60] H. Spieler, *Semiconductor Detector Systems*. Oxford University Press, 2005.
- [61] P. W. Nicholson, *Nuclear Electronics*. Hoboken, NJ, USA: John Wiley & Sons, Inc., 1974.
- [62] Z. Guzik and T. Krakowski, “Algorithms for digital gamma-ray spectroscopy,”

- Nukleonika*, vol. 58, no. November 2012, pp. 333–338, 2013.
- [63] V. T. Jordanov, G. F. Knoll, A. C. Huber, and J. A. Pantazis, “Digital techniques for real-time pulse shaping in radiation measurements,” *Nucl. Inst. Methods Phys. Res. A*, vol. 353, no. 1–3, pp. 261–264, 1994, doi: 10.1016/0168-9002(94)91652-7.
- [64] M. Bogovac, M. Jakšić, D. Wegrzynek, and A. Markowicz, “Digital pulse processor for ion beam microprobe imaging,” *Nucl. Instruments Methods Phys. Res. Sect. B Beam Interact. with Mater. Atoms*, vol. 267, no. 12–13, pp. 2073–2076, 2009, doi: 10.1016/j.nimb.2009.03.033.
- [65] D. Cosic, M. Bogovac, and M. Jakšić, “Data acquisition and control system for an evolving nuclear microprobe,” *Nucl. Instruments Methods Phys. Res. Sect. B Beam Interact. with Mater. Atoms*, vol. 451, pp. 122–126, Jul. 2019, doi: 10.1016/j.nimb.2019.05.047.
- [66] E. Vittone, “Theory of ion beam induced charge measurement in semiconductor devices based on the Gunn’s theorem,” in *Nuclear Instruments and Methods in Physics Research, Section B: Beam Interactions with Materials and Atoms*, Jun. 2004, vol. 219–220, no. 1–4, pp. 1043–1050, doi: 10.1016/j.nimb.2004.01.210.
- [67] V. Eremin, N. Stokan, E. Verbitskaya, and Z. Li, “Development of transient current and charge techniques for the measurement of effective net concentration of ionized charges (Neff) in the space charge region of p-n junction detectors,” *Nucl. Instruments Methods Phys. Res. Sect. A Accel. Spectrometers, Detect. Assoc. Equip.*, vol. 372, no. 3, pp. 388–398, Apr. 1996, doi: 10.1016/0168-9002(95)01295-8.
- [68] A. Pietropaolo *et al.*, “Neutron detection techniques from  $\mu\text{eV}$  to GeV,” *Phys. Rep.*, vol. 875, pp. 1–65, Sep. 2020, doi: 10.1016/j.physrep.2020.06.003.
- [69] H. Arahmane, E.-M. Hamzaoui, Y. Ben Maissa, and R. Cherkaoui El Moursli, “Neutron-gamma discrimination method based on blind source separation and machine learning,” *Nucl. Sci. Tech.*, vol. 32, no. 2, p. 18, Feb. 2021, doi: 10.1007/s41365-021-00850-w.
- [70] M. Pillon, M. Angelone, A. Krása, A. J. M. Plompen, P. Schillebeeckx, and M. L. Sergi, “Experimental response functions of a single-crystal diamond detector for 5–20.5 MeV neutrons,” *Nucl. Instruments Methods Phys. Res. Sect. A Accel. Spectrometers, Detect. Assoc. Equip.*, vol. 640, no. 1, pp. 185–191, Jun. 2011, doi: 10.1016/j.nima.2011.03.005.
- [71] S. Almaguilla *et al.*, “Improved performance in synthetic diamond neutron detectors: Application to boron neutron capture therapy,” *Nucl. Instruments Methods Phys. Res. Sect. A Accel. Spectrometers, Detect. Assoc. Equip.*, vol. 612, no. 3, pp. 580–582, 2010, doi: 10.1016/j.nima.2009.08.016.
- [72] M. Marinelli *et al.*, “High performance  $^6\text{LiF}$ -diamond thermal neutron detectors,” *Appl. Phys. Lett.*, vol. 89, no. 14, 2006, doi: 10.1063/1.2356993.
- [73] M. Osipenko *et al.*, “Calibration of a  $^6\text{Li}$  diamond-sandwich spectrometer with quasi-monoenergetic neutrons,” *Nucl. Instruments Methods Phys. Res. Sect. A Accel. Spectrometers, Detect. Assoc. Equip.*, vol. 931, pp. 135–141, Jul. 2019, doi: 10.1016/j.nima.2019.04.015.



- [74] M. Osipenko *et al.*, “Response of a diamond detector sandwich to 14 MeV neutrons,” *Nucl. Instruments Methods Phys. Res. Sect. A Accel. Spectrometers, Detect. Assoc. Equip.*, vol. 817, pp. 19–25, May 2016, doi: 10.1016/j.nima.2016.02.008.
- [75] P. Kavrigin, P. Finocchiaro, E. Griesmayer, E. Jericha, A. Pappalardo, and C. Weiss, “Pulse-shape analysis for gamma background rejection in thermal neutron radiation using CVD diamond detectors,” *Nucl. Instruments Methods Phys. Res. Sect. A Accel. Spectrometers, Detect. Assoc. Equip.*, vol. 795, pp. 88–91, Sep. 2015, doi: 10.1016/j.nima.2015.05.040.
- [76] M. Passeri *et al.*, “Neutron/Gamma separation in 500 $\mu$ m thick single crystal diamonds,” *Nucl. Instruments Methods Phys. Res. Sect. A Accel. Spectrometers, Detect. Assoc. Equip.*, vol. 974, no. May, 2020, doi: 10.1016/j.nima.2020.164195.
- [77] M. Astrain *et al.*, “Real-Time Implementation of the Neutron/Gamma Discrimination in an FPGA-Based DAQ MTCA Platform Using a Convolutional Neural Network,” *IEEE Trans. Nucl. Sci.*, vol. 68, no. 8, pp. 2173–2178, Aug. 2021, doi: 10.1109/TNS.2021.3090670.
- [78] M. Pavelek *et al.*, “Fast digital spectrometer for mixed radiation fields,” in *2017 IEEE SENSORS*, Oct. 2017, pp. 1–3, doi: 10.1109/ICSENS.2017.8234012.
- [79] T. Szczesmak *et al.*, “Digital neutron-gamma discrimination methods: Charge comparison versus zero-crossing,” in *2014 IEEE Nuclear Science Symposium and Medical Imaging Conference (NSS/MIC)*, Nov. 2014, pp. 1–4, doi: 10.1109/NSSMIC.2014.7431222.
- [80] M. Nakhostin, “Recursive algorithms for digital implementation of neutron/gamma discrimination in liquid scintillation detectors,” *Nucl. Instruments Methods Phys. Res. Sect. A Accel. Spectrometers, Detect. Assoc. Equip.*, vol. 672, pp. 1–5, Apr. 2012, doi: 10.1016/j.nima.2011.12.113.
- [81] M. Nakhostin, “A general-purpose digital pulse shape discrimination algorithm,” *IEEE Trans. Nucl. Sci.*, vol. 66, no. 5, pp. 838–845, May 2019, doi: 10.1109/TNS.2019.2910153.
- [82] T. S. Sanderson, C. D. Scott, M. Flaska, J. K. Polack, and S. A. Pozzi, “Machine learning for digital pulse shape discrimination,” in *2012 IEEE Nuclear Science Symposium and Medical Imaging Conference Record (NSS/MIC)*, Oct. 2012, pp. 199–202, doi: 10.1109/NSSMIC.2012.6551092.
- [83] C. Fu, A. Di Fulvio, S. D. Clarke, D. Wentzloff, S. A. Pozzi, and H. S. Kim, “Artificial neural network algorithms for pulse shape discrimination and recovery of piled-up pulses in organic scintillators,” *Ann. Nucl. Energy*, vol. 120, pp. 410–421, Oct. 2018, doi: 10.1016/j.anucene.2018.05.054.
- [84] G.-W. Huang *et al.*, “High-Performance Single-Crystal Diamond Detector for Accurate Pulse Shape Discrimination Based on Self-Organizing Map Neural Networks,” *Adv. Photonics Res.*, vol. 2, no. 12, p. 2100138, 2021, doi: 10.1002/adpr.202100138.
- [85] C. L. Wang, L. L. Funk, R. A. Riedel, and K. D. Berry, “Improved neutron-gamma discrimination for a  $^3\text{He}$  neutron detector using subspace learning methods,” *Nucl.*

- Instruments Methods Phys. Res. Sect. A Accel. Spectrometers, Detect. Assoc. Equip.*, vol. 853, pp. 27–35, May 2017, doi: 10.1016/j.nima.2017.02.022.
- [86] A. Pappalardo *et al.*, “Characterization of the silicon+6LiF thermal neutron detection technique,” *Nucl. Instruments Methods Phys. Res. Sect. A Accel. Spectrometers, Detect. Assoc. Equip.*, vol. 810, pp. 6–13, 2016, doi: 10.1016/j.nima.2015.11.114.
- [87] T. K. Alexander and F. S. Goulding, “An amplitude-insensitive system that distinguishes pulses of different shapes,” *Nucl. Instruments Methods*, vol. 13, no. C, pp. 244–246, 1961, doi: 10.1016/0029-554X(61)90198-7.
- [88] M. J. Safari, F. A. Davani, H. Afarideh, S. Jamili, and E. Bayat, “Discrete Fourier Transform Method for Discrimination of Digital Scintillation Pulses in Mixed Neutron-Gamma Fields,” *IEEE Trans. Nucl. Sci.*, vol. 63, no. 1, pp. 325–332, 2016, doi: 10.1109/TNS.2016.2514400.
- [89] B. D’Mellow, M. D. Aspinall, R. O. Mackin, M. J. Joyce, and A. J. Peyton, “Digital discrimination of neutrons and  $\gamma$ -rays in liquid scintillators using pulse gradient analysis,” *Nucl. Instruments Methods Phys. Res. Sect. A Accel. Spectrometers, Detect. Assoc. Equip.*, vol. 578, no. 1, pp. 191–197, 2007, doi: 10.1016/j.nima.2007.04.174.
- [90] J. E. McFee, C. M. Mosquera, and A. A. Faust, “Comparison of model fitting and gated integration for pulse shape discrimination and spectral estimation of digitized lanthanum halide scintillator pulses,” *Nucl. Instruments Methods Phys. Res. Sect. A Accel. Spectrometers, Detect. Assoc. Equip.*, vol. 828, pp. 105–115, 2016, doi: 10.1016/j.nima.2016.04.116.
- [91] G. A. Schlapper, *Measurement and Detection of Radiation*, 2nd ed. 1995.
- [92] J. Scherzinger *et al.*, “Tagging fast neutrons from a  $^{252}\text{Cf}$  fission-fragment source,” *Appl. Radiat. Isot.*, vol. 128, no. December 2016, pp. 270–274, 2017, doi: 10.1016/j.apradiso.2017.05.022.
- [93] P. Van Chuan, N. D. Hoa, N. X. Hai, N. N. Anh, N. N. Dien, and P. D. Khang, “A scintillation detector configuration for pulse shape analysis,” *Nucl. Eng. Technol.*, vol. 50, no. 8, pp. 1426–1432, 2018, doi: 10.1016/j.net.2018.07.009.
- [94] D. Cosic, G. Provasas, M. Jakšić, and D. Begušić, “Charge collection efficiency of scCVD diamond detectors at low temperatures,” *Diam. Relat. Mater.*, vol. 127, no. March, p. 109184, Aug. 2022, doi: 10.1016/j.diamond.2022.109184.
- [95] D. Cosic, G. Provasas, M. Jakšić, and D. Begušić, “scCVD Diamond Detector Response to Fast Neutrons and  $\gamma$ -Rays at Cryogenic Temperatures,” *IEEE Trans. Instrum. Meas.*, vol. 73, pp. 1–10, 2024, doi: 10.1109/TIM.2023.3341106.
- [96] E. Bossini and N. Minafra, “Diamond Detectors for Timing Measurements in High Energy Physics,” *Front. Phys.*, vol. 8, no. July, Jul. 2020, doi: 10.3389/fphy.2020.00248.
- [97] L. R. Dalesio *et al.*, “The experimental physics and industrial control system architecture: past, present, and future,” *Nucl. Instruments Methods Phys. Res. Sect. A Accel. Spectrometers, Detect. Assoc. Equip.*, vol. 352, no. 1–2, pp. 179–184, Dec. 1994, doi: 10.1016/0168-9002(94)91493-1.

- [98] CIVIDEC, “C6 Fast Charge Amplifier,” 2021.  
<https://cividec.at/index.php?module=public.product&idProduct=36&scr=0> (accessed Nov. 09, 2021).
- [99] M. Ciobanu, N. Herrmann, K. D. Hildenbrand, T. I. Kang, M. Kiš, and A. SchUttauf, “A charge sensitive amplifier for time and energy measurements,” *IEEE Nucl. Sci. Symp. Conf. Rec.*, no. November, pp. 2025–2028, 2008, doi: 10.1109/NSSMIC.2008.4774809.
- [100] C. Weiss *et al.*, “A CVD diamond detector for (n, a) cross-section measurements,” *Proc. Sci.*, vol. 18, pp. 1–8, 2011.
- [101] S. Agostinelli *et al.*, “Geant4 -- a simulation toolkit,” *Nucl. Instruments Methods Phys. Res. Sect. A Accel. Spectrometers, Detect. Assoc. Equip.*, vol. 506, no. 3, pp. 250–303, 2003, doi: 10.1016/S0168-9002(03)01368-8.
- [102] G. Santin, V. Ivanchenko, H. Evans, P. Nieminen, and E. Daly, “GRAS: A general-purpose 3-D modular simulation tool for space environment effects analysis,” *IEEE Trans. Nucl. Sci.*, vol. 52, no. 6, pp. 2294–2299, 2005, doi: 10.1109/TNS.2005.860749.
- [103] R. Brun, “ROOT.” 2019, doi: <https://doi.org/10.5281/zenodo.3457396>.
- [104] M. Jakšić *et al.*, “New capabilities of the Zagreb ion microbeam system,” *Nucl. Instruments Methods Phys. Res. Sect. B Beam Interact. with Mater. Atoms*, vol. 260, no. 1, pp. 114–118, 2007, doi: 10.1016/j.nimb.2007.01.252.
- [105] S. Harissopulos *et al.*, “The Tandem Accelerator Laboratory of NCSR ‘Demokritos’: current status and perspectives,” *Eur. Phys. J. Plus*, vol. 136, no. 6, p. 617, Jun. 2021, doi: 10.1140/epjp/s13360-021-01596-5.
- [106] J. Mayer *et al.*, “HDTV - Nuclear Spectrum Analysis Tool.” <https://gitlab.ikp.uni-koeln.de/jmayer/hdtv> (accessed Feb. 05, 2023).
- [107] J. Demšar *et al.*, “Orange: Data Mining Toolbox in Python,” *J. Mach. Learn. Res.*, vol. 1, no. 14, pp. 2349–2353, 2013, [Online]. Available: <http://jmlr.org/papers/v14/demsar13a.html>.
- [108] T. Ma, H. Song, B. Lyu, and J. Ma, “Comparison of Artificial Intelligence Algorithms and Traditional Algorithms in Detector Neutron/Gamma Discrimination,” *Proc. - 2020 Int. Conf. Artif. Intell. Comput. Eng. ICAICE 2020*, pp. 173–178, 2020, doi: 10.1109/ICAICE51518.2020.00040.

## Curriculum Vitae

Donny Domagoj Cosic was born in Zagreb, Croatia on the 06/04/1985 and moved to Canada in 1990 where he finished elementary and high school in Mississauga, Canada. In 2004, he enrolled in the Engineering Physics program at McMaster University in Hamilton, Canada where he specialized in micro/nanoelectromechanical systems with a subspecialty in nuclear engineering. Graduating summa cum laude in 2008, he continued his education at the International Space University in Strasbourg, France where he obtained his Master of Science degree in space studies in 2009 with the thesis titled “Radiation Effects on Electronics”. During his studies he completed an internship at the German Aerospace Center (DLR) in Oberpfaffenhofen, Germany where he continued working until 2011 as an embedded programmer designing test benches for studying radiation effects on commercial off-the-shelf electronic components. Since 2011 he has been working at the Laboratory for Ion Beam Interactions of the Ruđer Bošković Institute as a professional associate where he worked on the development of acquisition systems, automation of experimental set-up and accelerator control. In 2018 he enrolled in doctorate studies at the Faculty of Electrical Engineering, Mechanical Engineering and Naval Architecture in Split under the supervision of Prof. Dinko Begušić and dr. Tonči Tadić. In the scope of his PhD, he researched diamond detectors and their possible applications as micro-loss monitors in fusion research, more specifically, the DONES project. He participated in numerous international conferences, seminars and workshops, both with oral and poster presentations, and is the author and co-author of 21 peer-reviewed scientific articles.

## Curriculum Vitae

Donny Domagoj Cosic rođen je 06.04.1985. godine u Zagrebu, Hrvatska, a preselio se u Kanadu 1990. godine, gdje je završio osnovnu i srednju školu u Mississaugi, Kanada. 2004. godine upisao je studij inženjera fizike na Sveučilištu McMaster u Hamiltonu, Kanada, gdje se specijalizirao za mikro/nanoelektromehaničke sustave s podspecijalizacijom u nuklearnom inženjerstvu. Diplomirao je *summa cum laude* 2008. godine, nakon čega je nastavio školovanje na Međunarodnom Svemirskom Sveučilištu u Strasbourgu, Francuska, gdje je 2009. godine stekao titulu magistra znanosti u svemirskim studijima s radom naslova “Učinci zračenja na elektroniku”. Tijekom studija je odradio stručnu praksu u Njemačkom centru za svemirska istraživanja (DLR) u Oberpfaffenhofenu, Njemačka, gdje je nastavio raditi do 2011. godine kao programer dizajnirajući ispitne postave za proučavanje učinaka zračenja na komercijalne elektroničke komponente. Od 2011. godine radi u Laboratoriju za interakcije ionskih snopova Instituta Ruđer Bošković kao stručni suradnik, gdje je radio na razvoju akvizicijskih sustava, automatizaciji eksperimentalnih postava i upravljanju akceleratorima. Godine 2018. upisao je doktorski studij na Fakultetu elektrotehnike, strojarstva i brodogradnje u Splitu pod mentorstvom prof. Dinka Begušića i dr. Tončija Tadića. U sklopu svog doktorata istraživao je dijamantne detektore i njihove moguće primjene kao monitora mikro-gubitaka u istraživanju fuzije, točnije, u projektu DONES. Sudjelovao je na brojnim međunarodnim konferencijama, seminarima i radionicama, kako s usmenim tako i s posterskim prezentacijama, te je autor i koautor 21 znanstvenog rada objavljenog u međunarodnim znanstvenim časopisima.